GENERATING ENZYME-SYNTHESIZED HYALURONAN BRUSHES: CHARACTERIZATION, LENGTH REGULATION AND APPLICATIONS

A Dissertation
Presented to
The Academic Faculty

By

Wenbin Wei

In Partial Fulfillment
of the Requirements for the Degree
Doctor of Philosophy in the
School of Physics

Georgia Institute of Technology

August 2018

GENERATING ENZYME-SYNTHESIZED HYALURONAN BRUSHES: CHARACTERIZATION, LENGTH REGULATION AND APPLICATIONS

Approved by:

Dr. Jennifer E. Curtis, Advisor
School of Physics
Georgia Institute of Technology

Dr. James C. Gumbart
School of Physics
Georgia Institute of Technology

Dr. Harold D. Kim
School of Physics
Georgia Institute of Technology

Dr. Blair K. Brettmann
School of Materials Science and Engineering
Georgia Institute of Technology

Dr. Johnna S Temenoff
Department of Biomedical Engineering
Georgia Institute of Technology

Date Approved: July 25, 2018

ACKNOWLEDGEMENTS

I would like to thank my advisor, Dr. Jennifer Curtis for her support, patience, intellectual guidance, trust and tolerance to radical ideas and encrypted English. I would also thank Dr. Daniel Kovari as a second mentor throughout my graduate study. I would also express sincere gratitude to Dr. Paul Weigel, Jennifer Washburn and Bruce Baggenstoss for the material and technical support on the hyaluronan synthases used in this thesis. I would appreciate the irreplaceable contributions of Patrick Chang, Jessica Faubel and Hemaa Selvakumar in developing and executing the techniques in this thesis.

My work was supported by the National Science Foundations (NSF) via grants awarded to my advisor (#0955811, #1709897) and financial support from the NSF-founded Physics of Living Systems research node at Georgia Tech (#1205878). My work was also supported by GaTech Fire Award.

I would like to thank all my instructors on math, physics, chemistry and biology for helping me to build an all-round knowledge foundation which is vital of the interdisciplinary research in this thesis.

Words fail me when I try to express my wholehearted gratitude to my father, Hong Wei and my mother, Ping Yang for their 22 years of support, caring and sacrifice throughout my education. Finally, I would like to thank my wife, Xinrui Zhang whose presence in my life is a blessing. It is hard to express how grateful I am to have felt her love and support.

TABLE OF CONTENTS

LIST OF TABLES

LIST OF FIGURES

SUMMARY

Polymer brushes are tethered polymers at an interface with high grafting densities. Polymer brushes have rich physics phenomena and wide applications. We developed a distinct class of polymer brush which increased the typical length scale of polymer brush thickness by nearly two orders of magnitude, from less than a few hundred nanometers to ten microns. The hyaluronan brush can be visualized using optical microscopy which makes them a unique tool to study the physics of polymer brushes in ways previously never accessible. Moreover, the brush and is also a promising biological material which mimics the backbone of the glycocalyx on the cell surface.

The super thick hyaluronan brush is achieved by attaching membrane fragments from bacteria overexpressing hyaluronan synthase to surfaces and then turning on the synthesis. We developed a toolkit to study the interactions between the hyaluronan brush and proteins, nanoparticles, bacteria and mammalian cells. We also developed a diffraction-based method to measure the dynamic thickness of the brush with great spatial and temporal resolution.

The resultant brush reached a thickness of $10.6\,\mu\mathrm{m}$ under physiological conditions after a synthesis duration of $16\,\mathrm{h}$ on a planar surface. The brush blocked $> 100\,\mathrm{nm}$ nanoparticles. The density profile was exponential-like, indicating the polymers in the brush were polydisperse. The kinetics of the brush growth suggest a length-dependent detachment tension in a polymer brush made of polydisperse polymers. In testing its potential in the application of implants, we found the brush allowed normal attachment and proliferation of mammalian fibroblast cells, but that blocks a strain of bacteria which is the most frequent pathogen associated with implants for at least two weeks.

CHAPTER 1
INTRODUCTION

Glycans are one of the four fundamental macromolecules in biological systems in addition to nucleic acids, proteins, and lipids. Glycans are involved in a broad spectrum of biological activities including both health and disease conditions [1]. Comparing glycans in normal and disease conditions have advanced the understanding of human health and disease [2]. However, much is still unknown. Glycans are made of different types of sugar units linked in multiple ways and a wide variety of glycans can be created. This huge number of possible structures is also multiplied by the complexity of interactions between glycans and other biological molecules [2]. This great structural and functional diversity poses challenges to probe and manipulate glycans. According to a report by the *Committee on Assessing the Importance and Impact of Glycomics and Glycosciences* convened by the National Research Council, new techniques and tools are in demand to close the large gaps in areas such as the chemical and enzymatic synthesis of glycans and the analytical characterization of glycan structures and functions [2].

As physicists, we have chosen to focus on the glycan hyaluronan (HA), and the molecular machine that makes it, hyaluronan synthase. Hyaluronan is a simple but unusual linear glycan of various biological functions [3, 1, 4]. An adult has $12\,\mathrm{g}$ to $15\,\mathrm{g}$ of hyaluronan 1/3 of which is turned over every day [5]. It is in many tissues in the body, and as a very high molecular weight polymer, it has been established to have a clear biomechanical role in numerous scenarios ranging from cartilage [6], to the umbilical cord [7], to fertilization [8, 9] . Many other scenarios strongly imply a biophysical role for hyaluronan, including its role in modulating cell adhesion and migration in embryogenesis [10], wound healing [11] and cancer metastasis [4], as well as its role in regulating synaptogenesis [12]. Yet, it is rare to have these questions investigated from a biophysical perspective. These ob-

servations combined with the ubiquity of hyaluronan in the human body, its necessity for embryonic survival [13], and its well defined and unmodified chemical composition (unlike many other glycans), we identified a unique intellectual space for a biophysics lab to enter glycan research.

Hyaluronan synthase, the enzyme which synthesizes hyaluronan, is the only synthase which synthesizes the polymer at the cell's plasma membrane while extruding its product into the extracellular space [14]. We are also motivated by our collaborator Dr. Paul Weigel[1] who is a world-class molecular biologist who has spent his career studying hyaluronan synthase, providing many useful data and insights about the molecular machine's functions. Unlike DNA and proteins, glycan synthases (also called glycotransferases) do not have a template to copy. Hence the size and distribution of sizes of their product (the final polysaccharide) depend on other factors. Dr. Weigel, after extensive research, proposed a mechanical model on how hyaluronan synthase makes hyaluronan of a relatively narrow length distribution. He hypothesizes is that an (unidentified) mechanical force on the growing hyaluronan chain exists that increases with the length of the polymer, resulting in a length-dependent detachment rate that determines the shape of the final distribution.

The initial and most ambitious goal of this body of work was to test our hypothesis that polymer physics provides a natural length dependent polymer tension and that if we can determine the functional dependence of this tension on length, we can explain using a kinetic model, the final length distribution of hyaluronan [15]. This interesting project led us to the Weigel lab where we learned to produce and handle hyaluronan synthase membrane fragments, providing us experimental access to the molecular machine.

As many ambitious scientific stories go, that final goal is still under pursuit. However, along the way, many discoveries and opportunities were realized with this hyaluronan-synthesizing system which has opened unexpected but valuable avenues of research in polymer physics, cell biophysics and antimicrobial biomaterials . At the heart of these

[1] with honor and pride

new directions is the discovery that one can leverage the high densities of hyaluronan synthase in membrane fragments to generate a distinct class of polymer brush. We achieve this by attaching the membrane fragments to surfaces and then turning on synthesis. The result is a quite robust system to generate the thickest polymer brushes ever realized with synthetic or natural biopolymers using a new methodology distinct from the traditionally grafting from and grafting to brush technologies.

In order to study this system, as well as to pursue the biophysical question of HA length regulation, we have developed many new experimental tools to study the kinetics of hyaluronan synthesis and the interactions of hyaluronan with nanoparticles and proteins. Many of the intriguing biophysical questions for the length regulation of hyaluronan and the synthesis process remain. However, with the efforts in this work to develop tools to handle, measure, interrogate hyaluronan and its synthase, future workers will be in a better position to pursue. Our relative simple system can also facilitate the development computer simulations of glycans with other entities such as proteins and nucleic acids before they are applied to more challenging systems. This thesis work should be able to make a contribution to glycoscience.

CHAPTER 2

BACKGROUND

2.1 Hyaluronan

Glycosaminoglycans are long unbranched polysaccharides consisting of a repeating disaccharide unit. Hyaluronan is the only unsulfuric glycosaminoglycan, and hence its chemical structure is always well-defined. The disaccharide unit in hyaluronan is composed of D-glucuronic acid (GlcUA) and D-N-acetylglucosamine (GlcNAc), linked via alternating $[\beta(1 \rightarrow 4)]$ and $[\beta(1 \rightarrow 3)]$ bonds. Each disaccharide unit is about $1\,\mathrm{nm}$ long and $0.5\,\mathrm{nm}$ wide [16]. The molecular mass of each disaccharide residue $C_{12}H_{21}NO_{11}$ is 389 g/mol thus the conversion factor between molecular mass and length of hyaluronan is $389\,\mathrm{g\,mol^{-1}\,nm^{-1}}$. The chemical structure of hyaluronan is shown in Figure 2.1. The carboxyl group on each glucuronic acid monomer makes hyaluronan negatively charged at physiological conditions. The carboxyl group is an easy site to perform chemistry with, and as such, it is frequently the target of materials scientists who modify hyaluronan with crosslinkers [17] or attachment of proteins or antimicrobials [18]. hyaluronan is synthesized at plasma membrane instead of the Golgi apparatus (where most other sugars are made) and mostly exists in extracellular regions. The transmembrane enzyme hyaluronan

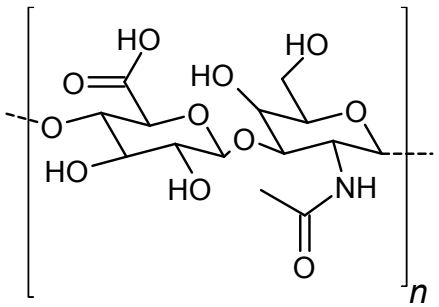

Figure 2.1: The chemical structure of hyaluronan.

synthase is responsible for assembling the polymer and extruding it simultaneously through the plasma membrane into the extracellular space [19, 20, 21].

Hyaluronan is among the largest polysaccharides in nature. Hyaluronan molecules can have up to $25,000$ disaccharide residues, corresponding to $9.5\,\mathrm{MDa}$ in molecular mass and $25\,\mu\mathrm{m}$ in length. Measured in $0.15\,\mathrm{M}$ NaCl at $37\,^{\circ}\mathrm{C}$ using multi-angle light scattering, the radius of gyration $\mathrm{R_g}$ of hyaluronan of molecular mass ranging from $40\,\mathrm{kDa}$ to $5.5\,\mathrm{MDa}$ can be well described by a single equation $\mathrm{R_g} = 2.75 \times 10^{-2}\mathrm{M}^{0.596}$, where $\mathrm{R_g}$ is in nm and molecular mass M is in $\mathrm{g\,mol^{-1}}$, and the persistence length of hyaluronan is estimated to be $7.5\ \mathrm{nm}$ [22]. Hyaluronan behaves as a stiffened random coil and exhibits non-Newtonian rheology properties which are heavily influenced by both hyaluronan concentration and length [23]. The characteristic relaxation time (rheology response to large-scale motions) of $10\,\mathrm{mg\,mL^{-1}}$ hyaluronan solution is $1.23\,\mathrm{s}$ for $1.27\,\mathrm{MDa}$ hyaluronan and $13.4\,\mathrm{s}$ for $2.88\,\mathrm{MDa}$ hyaluronan.

Hyaluronan is made of repeating disaccharide units but has various biological functions depending on its length[4]. Long hyaluronan ($> 1\,\mu\mathrm{m}$, $> 0.4\,\mathrm{MDa}$) fills space, lubricates joints, absorbs shocks, suppresses proliferation, inflammation and the formation of blood vessels [4]; intermediate length hyaluronan ($0.1\,\mu\mathrm{m}$ to $1\,\mu\mathrm{m}$, $40\,\mathrm{kDa}$ to $400\,\mathrm{kDa}$) is involved in ovulation [24] and embryogenesis [13]; short hyaluronan polymers ($20\,\mathrm{nm}$ to $100\,\mathrm{nm}$) are involved in signaling, enhancement of inflammatory effects and the formation of blood vessel [4]; hyaluronan oligomers of a few disaccharide residues promote early steps in metastasis and suppress programmed cell death [2]. The biological functions and properties of hyaluronan also depend on its conformation which is influenced by protein decoration and the mechanical and chemical properties of the local environment [2].

2.2 Hyaluronan Synthase

An enzyme called hyaluronan synthase produces hyaluronan. Figure 2.2, 2.2 and Figure 2.4 shows its predicted topology [25] and predicted structure [15]. hyaluronan synthase re-

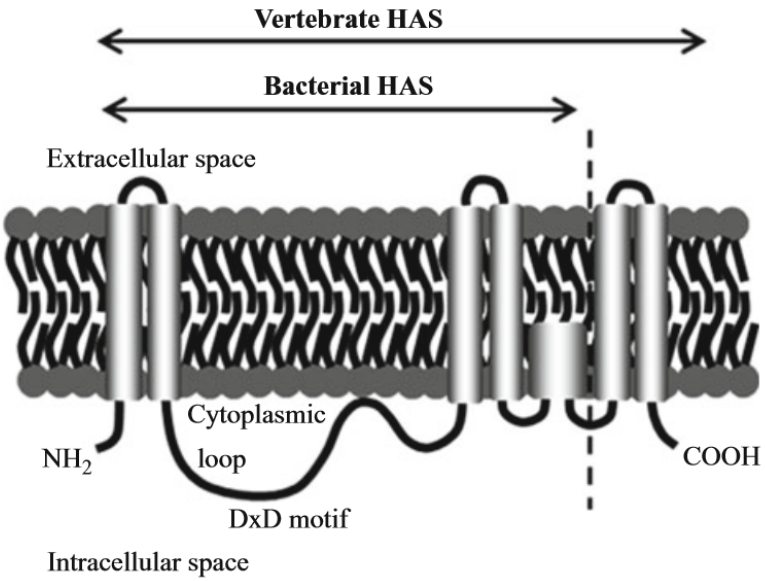

Figure 2.2: Predicted bacterial and mammalian topology of hyaluronan synthase, including a large cytoplasmic loop and clusters of transmembrane domains. Vertebrate hyaluronan synthase is predicted to have two more transmembrane protein domains than bacterial hyaluronan synthase [25]. The extra transmembrane domains may involve in the post-translational modulation [26]. The image was originally published by Itano *et al.* [25]. Reprinted here under the Attribution-NonCommercial 4.0 International (CC BY-NC 4.0).

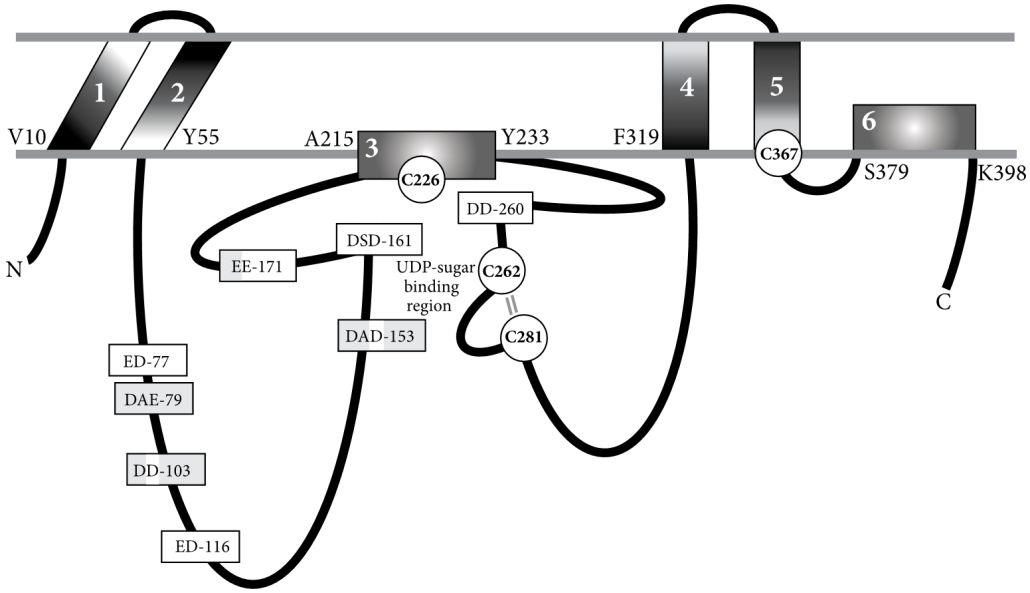

Figure 2.3: Predicted topology of hyaluronan synthase from *Streptococcus equisimilis*, incorporating recent results [27]. Amino acid residues are numbered starting from the N (-H_2) end. Four Cys residues (white circles) are located in or very near to the sugar-UDP binding sites [28]. Potential glycosyl-UDP binding sites are shown in rectangle boxes. The image was originally published by Weigel *et al.* [27]. Reprinted here under the Attribution-NonCommercial 4.0 International (CC BY-NC 4.0).

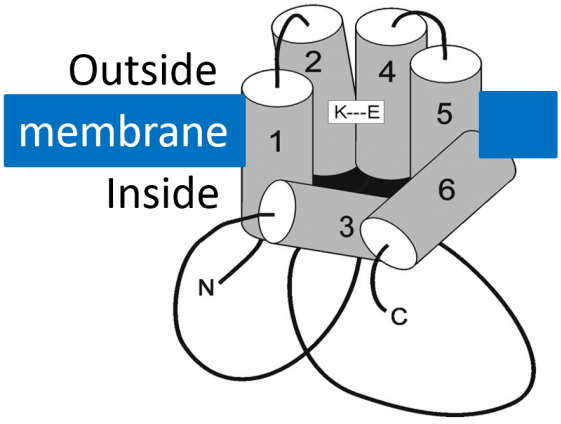

Figure 2.4: Predicted structure of hyaluronan synthase[15]. Hyaluronan synthase utilizes cardiolipin and its transmembrane domains to form an intra-protein pore. The image was originally published by Weigel *et al.* [15]. Reprinted here under the Attribution-NonCommercial 4.0 International (CC BY-NC 4.0).

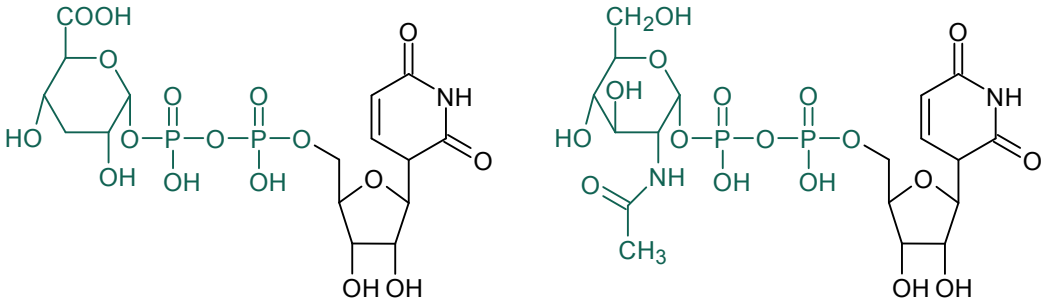

Figure 2.5: UDP-GlcUA and UDP-GlcNAc, Substrates for hyaluronan synthesis. UDP is colored in green. It is linked to the reducing end of the sugar.

quires Mg^{2+} ions and precursor UDP-sugars (UDP-GlcUA and UDP-GlcNAc), where UDP is short for uridine diphosphate glucose. The chemical structure of the two UDP-sugars is shown in Figure 2.5. The UDP-sugars serve both as substrates and energy sources to drive the reactions. Hyaluronan synthase is the only protein needed for hyaluronan synthesis [29]. The active streptococcal hyaluronan synthases we are using is a complex made of one hyaluronan synthase protein and about 14-18 molecules of cardiolipin [29]. Hyaluronan synthase uses its two glycotransferase activities to alternately add alternatingly add UDP-GlcUA and UDP-GlcNAc to elongate the hyaluronan polymer. Except for the hyaluronan synthase from *P. multocida* bacteria, all the other known hyaluronan synthases belong to the Class I hyaluronan synthases, including hyaluronan synthases from mammals, avians, amphibians, and some types of viruses and bacteria [19]. Class I hyaluronan synthases are processive in that they retain binding to the nascent hyaluronan chains during the synthesis. In contrast, hyaluronan synthase from *P multocida* is distributive and randomly binds to a hyaluronan polymer and releases it after elongating it by one monomer. It is the only member in the Class II hyaluronan synthase. In this thesis, we only study Class I hyaluronan synthases and use the hyaluronan synthase from *Streptococcus equisimilis* as the model enzyme.

Hyaluronan synthases are composed of 417-588 amino acids with a mass ranging from

$49 - 69\ \mathrm{kDa}$, with bacterial hyaluronan synthases on the lower end and mammalian hyaluronan synthases on the higher end of the size range [19]. Hyaluronan synthases across different kingdoms share sequence and structure similarities [19]. The hyaluronan synthases from the bacteria family *streptococcal* are 70% identical to each other and 25% identical to the vertebrate hyaluronan synthases [19]. Hyaluronan synthases have a large cytoplasmic loop [30]. In this loop, all hyaluronan synthases have conserved regions surrounding a DxD motif (D stands for aspartate and x stands for any amino acid) [19]. In most of the enzymes synthesizing polysaccharides, the DxD motif is a critical component for the binding of UDP precursors [31]. Based on the fact that UDP-sugar substrates exist inside the cell, it makes sense that the cytoplasmic loop of hyaluronan synthase is where catalytic reactions take place [25].

Unfortunately, there is no crystallographic data of hyaluronan synthases in public literature. The topology of hyaluronan synthase from *Streptococcus pyogenes* has been experimentally determined [30]. All the hyaluronan synthases are predicted to share the same overall domain configuration [14] (see Figure 2.2). All hyaluronan synthases are integral membrane proteins with multiple transmembrane domains [21]. Vertebrate hyaluronan synthases have six transmembrane domains, and bacterial hyaluronan synthases have four transmembrane domains. These transmembrane domains, together with cardiolipins, form an intra-protein pore which both binds the nascent hyaluronan for processive synthesis and allows the polymer to translocate into the extracellular space [32, 33]. Based on an estimation of the thickness of the cell membrane [34], the pore can make contact with 4-5 disaccharide monomers, which are $1\ \mathrm{nm}$ in length each.

Length of hyaluronan product (biochemical language for the hyaluronan released by the enzyme) depends on the type of hyaluronan synthase. Mammalians have three hyaluronan synthase isoforms HAS1, HAS2 and HAS3 to regulate hyaluronan production: HAS2 generates huge hyaluronan chains ($> 2\ \mathrm{MDa}$); HAS1 generates hyaluronan of molecular mass between $0.2\ \mathrm{MDa}$ and $2\ \mathrm{MDa}$; HAS3 generates hyaluronan of molecular mass from

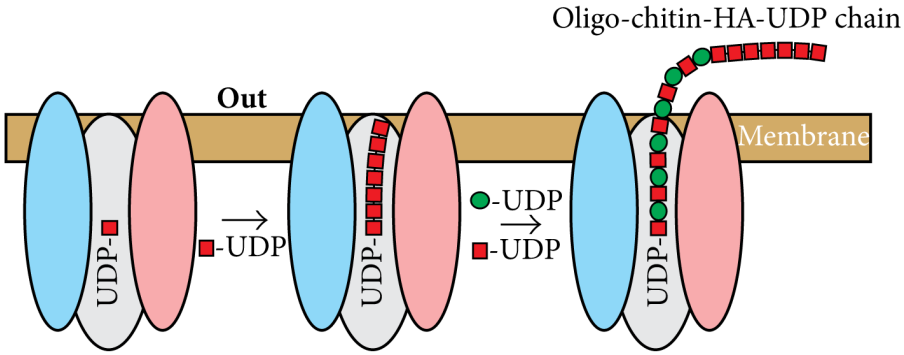

Figure 2.6: Hyaluronan synthase uses GlcNAc-UDP to form short chitin-UDP polymers. The short chitin is used as the primer for alternatively adding GlcNAc and GlcUA to the reducing end of hyaluronan [27]. The hyaluronan polymer is extruded into the extracellular region as its length increases. Hyaluronan synthase retains binding to hyaluronan until hyaluronan is released and synthesis is terminated. The image was originally published by Weigel *et al.*[27]. Reprinted here under the Attribution-NonCommercial 4.0 International (CC BY-NC 4.0).

0.1 MDa to 1 MDa [20]. Hyaluronan produced by hyaluronan synthase from *Streptococcus equisimilis*, which we used in this thesis work, has an average molecular mass of 3.78 MDa and the distribution spans from 0.1 MDa to 4 MDa [15].

2.3 Production of Hyaluronan

A schematic of hyaluronan synthesis by hyaluronan synthase is shown in Figure 2.6. Hyaluronan synthases do not require a primer to initialize hyaluronan synthesis. However, hyaluronan synthases can produce $\mathrm{GlcNAc_n - UDP}$ oligomers from UDP-GlcNAc substrates and these short chains could serve as self-primers for hyaluronan synthases [27]. After this initialization step, hyaluronan synthase enzyme starts to repeat the cycles of UDP-sugar addition for up to $50,000$ times: the UDP molecule on the tail of the nascent polymer hyaluronan-UDP is replaced with either a UDP-GlcUA or UDP-GlcNAc substrate molecule; hyaluronan is then translocated through the pore of hyaluronan synthase by one monomer into the extracellular region; now the hyaluronan synthase is ready for the next cycle [27]. The duration of each cycle is shorter than 0.5 s under optimized conditions [15]. There

exists a dilemma that hyaluronan synthase enables hyaluronan to rapidly slide through the intra-protein pore yet retains hyaluronan for hours to finish the processive synthesis. One plausible explanation is that the hyaluronan synthase cytoplasmic loop and intra-protein pore forms multiple bonds with the repeating monomers along hyaluronan including electrostatic interactions, hydrophobic interactions, van der Waals interactions and hydrogen bonds [15]. We speculate that, due to the repeating pattern of hyaluronan polymer, the hyaluronan synthase-hyaluronan binding energy remains unchanged if the hyaluronan polymer slide by the length of one repeating monomer and the energy barrier is much lower than breaking all the bonds between hyaluronan synthase and hyaluronan. Also, hyaluronan synthase also binds the hyaluronan via interaction to the UDP molecule at the tail of the polymer. This binding is temporarily lost in each cycle of monomer addition. We speculate this temporary phase without UDP favors hyaluronan translocation in the phase of catalytic reaction over the quiescent phase when hyaluronan synthase is waiting for new substrate molecules. The most likely phase of detachment can be tested by detecting UDP in the released hyaluronan polymers. hyaluronan synthase cannot elongate exogenously added free hyaluronan chains [35, 36]. Thus the length of a hyaluronan polymer is defined once it is released from its enzyme. Hyaluronan release and hyaluronan length regulation are tightly related.

2.4 Hyaluronan Length Regulation

The goal of this thesis is to understand how hyaluronan synthase produces hyaluronan with a specific length distribution. In a system of polymer synthesis, product length distribution is closely related to how and when the polymer is released from the enzyme, and we can infer properties of the enzyme based on its product length distribution. For example, in mammalian DNA replication, the detachment of nascent DNA is controlled by the terminated signal on the template DNA. Thus the product DNA polymer has an equal length as the template DNA. In contrast, imagining a polymer synthesis system where polymer

detachment is a fully random event and the probability is independent of polymer length, the probability of producing long polymers exponentially decreases as the polymer length increases, resulting in a geometric distribution of product length (see Section 5.5 for a detailed discussion). In hyaluronan synthesis, the length distribution of hyaluronan product peaks on the order of $10^6\mathrm{Da}$ and spans two orders of magnitudes (see Figure 5.2A). It is not as monodisperse as DNA nor as broad as the imaginary polymer product with length independent detachment probability. Therefore, in order to explain hyaluronan length distribution, we hypothesize that hyaluronan detachment is a stochastic event whose probability increases with increasing polymer length.

More than a decade of biochemical studies by Weigel and colleagues have led to the conclusion that hyaluronan release is most likely a mechanical process [15, 27]. It has been found that common length regulation mechanisms cannot explain hyaluronan synthase. First, hyaluronan length is not limited by the lifetime of hyaluronan synthase. Baggenstoss *et al.* [37] measured the rate of hyaluronan synthesis and the rate of hyaluronan product length increase by recombinant bacterial *Streptococcus equisimilis* hyaluronan synthase (seHAS). They found, under optimized conditions, the rate of hyaluronan synthesis was constant for at least 8 hours, but the length of hyaluronan reached a steady-state distribution within 2-4 hours. This result indicates that, at least within the first 8 hours, hyaluronan synthases stayed active and moved on to synthesize new hyaluronan polymers after the current hyaluronan polymers were released [37]. Second, hyaluronan release is not triggered by an external chemical signal. When hyaluronan synthases are introduced into a foreign host, and potential external chemical signal is eliminated, hyaluronan synthases still show length regulation ability [19, 37, 15]. Third, an internal chemical signal is also unlikely. The radius of gyration of a mature hyaluronan polymer is on the order of 100 nm while the 70 kDa hyaluronan synthase is smaller than 10 nm in diameter. Also, most of the amino acids of hyaluronan synthase are inside the cell [27]. Thus hyaluronan synthase cannot sense the real-time length/size of hyaluronan via contact and hyaluronan synthase needs to

keep the information of hyaluronan length inside itself if hyaluronan synthase dynamically determines the hyaluronan detachment. However, it is improbable that the small hyaluronan synthase protein (< 500 amino acid residues) possesses any counting machinery.

Results from mutagenesis studies of hyaluronan synthase do not support a counting model. In a counting model, parts of hyaluronan synthase responsible for hyaluronan synthesis also control hyaluronan product length, thus hyaluronan synthesis rate and hyaluronan length product should not be uncoupled by mutagenesis of a single amino acid, unless the same amino acid participate both functions. In of one the mutagenesis studies conducted by Dr. Weigel, 18 mutants of seHAS in four important cysteine amino acid residues were compared with the wildtype seHAS [15]. These four cysteines locate at the sites for catalytic reactions and are conserved in the mammalian hyaluronan synthase family. Among these 18 mutants, 4 showed no change in either synthesis rate or product length, 3 showed changes in both of the two functions and the remaining 11 mutants showed changes in only one of the two functions. This result suggests that synthesis rate and length control are discrete functions that can be uncoupled by mutagenesis. Therefore, this result does not support the counting model.

During the synthesis, hyaluronan synthase forms bonds with hyaluronan via the disaccharide residues and the UDP molecule at the tail of hyaluronan. None of these bonds is covalent [29] and their lifetime can be greatly reduced by external pulling force [38], unless hyaluronan synthase and hyaluronan-UDP form a catch bond that strengthens under tension [39]. Thus, an immediate candidate for the releasing trigger is the pulling force by hyaluronan on the binding sites between hyaluronan and hyaluronan synthase. This leads to the mechanical length regulation mechanism. This mechanism emphasizes the coupling between hyaluronan pulling force and HA-hyaluronan synthase interactions. An implementation of this mechanism was first proposed by Dr. Paul Weigel [19, 15, 27].

2.5 Mechanical Length Regulation Model

The original model proposed by Dr. Weigel is called the retain-release model [15]. Multiple diverse interactions between hyaluronan-UDP and hyaluronan synthase (e.g., H-bonds and ionic and hydrophobic interactions, within and surrounding the intra-protein pore, provides a net retention ($\mathrm{F_{retain}}$)). The hyaluronan-hyaluronan synthase interactions are independent of hyaluronan length or history of hyaluronan synthesis. $\mathrm{F_{retain}}$ serves to balance the opposing releasing force ($\mathrm{F_{release}}$). $\mathrm{F_{release}}$ results from multiple types of forces in the external environment, including random Brownian motion, fluid currents, interactions with cell surface or extracellular matrix proteins and inertial forces due to cell or surface membrane motion. $\mathrm{F_{release}}$ is hypothesized to increases as hyaluronan length increases, thus increasing the probability of hyaluronan release. We infer from Dr. Weigel's publication that hyaluronan-synthase interaction is not a catch bond and thus weakens under external force. Therefore the force should not decreases as hyaluronan length increases. Otherwise, long hyaluronan will not detach from hyaluronan synthase and its length will keep increase until hyaluronan synthase becomes inactive, which is against the fact that hyaluronan length plateaus.

Dr. Weigel's mechanical model is consistent with the experimental facts about hyaluronan length regulation. It can qualitatively describe the length distribution of hyaluronan product. The fact that Different hyaluronan synthases produce hyaluronan with different size distribution can be explained by the difference in binding affinity to hyaluronan. Microenvironmental factors may influence the pulling force and hyaluronan-hyaluronan synthase binding affinity and thus hyaluronan product size.

2.6 Polymer Brush

Polymer brush is an array of polymers one of which end is grafted on a surface. A commonly used parameter for quantitative describing the transition from an array of isolated

end-graftd polymers to a polymer brush is the reduced tethered density [40]:

$$\Sigma = \sigma \pi R_g^2, \tag{2.1}$$

where R_g is radius of gyration and σ is the grafting density which can be determined by $\sigma = 1/D^2$ and D is the distance between grafting points [40]. A literature survey by Brittain *et al.* [40] suggest that polymer brushes demonstrate strong repulsion effect in good solvent if $\Sigma >> 5$. According to the estimation and characterization in Chapter 4, we estimate the reduced tethered density is 11-42 (σ = $300\,\mu\mathrm{m}^{-2}$, $\mathrm{M_w} = 1\,\mathrm{MDa}$ to $3\,\mathrm{MDa}$) in our array of hyaluronan tethered on hyaluronan synthase. Thus we do generate polymer brush.

For a polymer brush of identical polymers and weak excluded-volume interactions and at moderately high surface coverage on a planar surface, using a self-consistent field method assuming , it has been calculated that there is a scaling law between the brush thickness H, polymer contour length L and grafting density σ [41],

$$H \propto L\sigma^{1/3}. \tag{2.2}$$

Later this scaling laws is found apply for brush made of polydisperse polymers of the same kind [42]. The same group also studied penetration of nanoparticles into a polydisperse brush [43].

2.7 Summary of Dr. Weigel's Paper

This is a brief summary of Dr. Weigel's paper for the interest of biophysical research.

Table 2.1: Summary of Dr. Weigel's Paper for the interest of biophysical research.

Key words	Key Points
Mutagenesis	Synthesis rate and hyaluronan product size are independent functions [15, 44].
Chemical Modification	Modifying Cys residues with N-ethylmaleimide deactivates hyaluronan synthases [28]. Modifying Cys residues with N-ethylmaleimide reduces transportation of dye through the pore in hyaluronan synthases [33]. Oxidization greatly reduce the activity of hyaluronan synthases [45]. Oxidization greatly reduces transportation of dye through the pore in hyaluronan synthases [33].
Substrate Dependent	Optimal UDP-sugar concentration is ($> 1\,\mathrm{mM}$) of equal molar concentration [46].
Chemical Environment	$30\,^{\circ}\mathrm{C}$ is a good compromise between thermal stability and activity for hyaluronan size [47]. Pretreatment at pH 5.5 reduces activity by $85\,\%$ [47]. The activity of hyaluronan synthase is stable up to 1M glycerol [47, 44]. UDP inhibits hyaluronan synthesis [47, 37]. UDP-sugars inhibit hyaluronan synthesis in a biphasic manner, leveling off around $0.1\,\mathrm{mM}$ [47].
Predicted Structure	Topological measurement [30] and prediction [19, 27]. Single hyaluronan synthesis monomer is active [29].
Mechanical Model	Weigel [19, 15, 27, 48]
Energy Analysis	Weigel [48]
Techniques	Radiation inactivation [29]. Size exclusion chromatography with multi-angle static light scattering [37, 15] Activity assay using radioactive UDP-sugars [37, 49]. Agarose gel electrophoresis assay [49] Eukaryotic cell membrane preparation [49]

CHAPTER 3

DEVELOPING EXPERIMENTAL PROTOCOLS

3.1 Hyaluronan Synthase

The HAS membrane fragments used in this work are a generous gift provided by our collaborator Dr. Weigel (Department of Biochemistry and Molecular Biology, The Oklahoma Center for Medical Glycobiology, The University of Oklahoma Health Sciences Center) and prepared by his research assistant Jennifer Washburn according to published protocols [46]. According to the results from protein gel electrophoresis (Figure 3.1), about $7\,\%$ of the membrane protein is HAS, rendering a high HAS density around $1000\,\mu\mathrm{m}^{-2}$ if one estimates that a typical membrane protein density of $30\,000\,\mu\mathrm{m}^{-2}$ [50]. We followed established protocols from the Weigel lab to handle the HAS membrane. The details can found below.

3.2 Hyaluronan Synthase Membrane Fragment Immobilization

We used the amine crosslinker glutaraldehyde to crosslink the amine groups on a polyethyleneimine (PEI) coated coverslips and the amine groups on membrane fragment carrying hyaluronan synthase. The amines on the membrane arise from the abundant protein content, which could be hyaluronan synthase or other proteins. As shown below, this attachment does not prevent hyaluronan synthase activity either due to chemistry or blockage of substrates from reaching the synthase. This protocol is adopted from a protocol to immobilize bacteria on glass surfaces [51]. Full details of the process are given below.

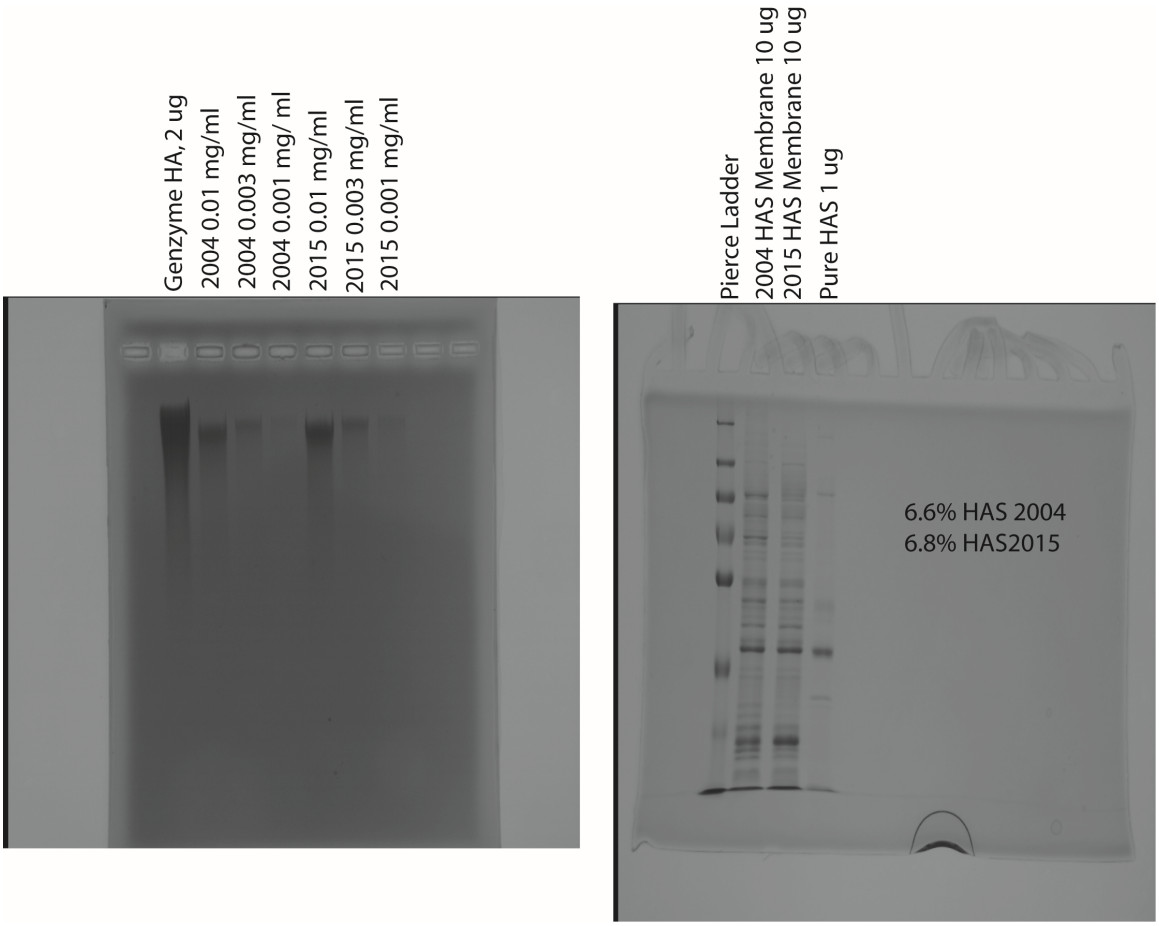

Figure 3.1: Characterization by Jennifer Washburn which was shipped together with the hyaluronan synthase sample. **Left** hyaluronan of a 1 h activity assay. **Right** western blotting to determine the yield of hyaluronan synthase.

3.2.1 Immobilizing HAS on Planar Glass Coverslip

Surface Cleaning

First, coverslips were sonicated in ultrapure water for $15\,\mathrm{min}$. Second, coverslips were soaked in reagent grade acetone in a sonicating water bath for 15 minutes. Third, coverslips were rinsed with ultrapure water and dried with nitrogen flow. Last the coverslips were cleaned in a plasma cleaner (Harrick Plasma, PDC-32G, High RF power, air, $1\,\mathrm{min}$). Now the glass surface has a high density of OH groups and is negatively charged.

Attaching Latex Microsphere to Coverslips

This step is for the diffraction-based microsphere tracking method to measure brush height. It took place between the sonication cleaning step and the plasma cleaning step. The latex beads are incompatible with acetone. Thus we replaced acetone with ethanol in the final sonication washing step before the plasma cleaning. We also extended the plasma cleaning process from $1\,\mathrm{min}$ to $3\,\mathrm{min}$ in order to compensate for the weaker cleaning strength of ethanol compared to acetone.

$3\,\mu\mathrm{m}$ latex microspheres were diluted 200 times with isopropanol. $8\,\mu$Lof the diluted latex microsphere suspension was pipetted onto each dried coverslip. After the isopropanol evaporated, the coverslips were baked $2\,\mathrm{min}$ in a $140\,^{\circ}\mathrm{C}$ oven in order to partially melt and permanently adhere them to the surface [52]. The coverslips were sonicated in ethanol for $15\,\mathrm{min}$ followed by sonication in ultrapure water for $15\,\mathrm{min}$.

Coating Poly(ethylenimine) on Coverslips

Polyethyleneimine (PEI) is positively charged and has a high affinity with the negatively charged glass surface. PEI (Sigma 482595, average Mw 1.3kDa, $50\,\%$ w/v in $\mathrm{H_2O}$) was diluted with ultrapure water. We adjusted its pH to 7 using HCl. The final concentration of PEI is $2.5\,\%$. Right after the plasma cleaning, $200\,\mu$L PEI was used to cover each coverslip

(facing up). The coverslips were incubated for 1 hour before they were rinsed with ultrapure water and dried in a nitrogen flow.

Modifying Coverslips with Glutaraldehyde

After coated with Poly(ethylenimine), coverslips were incubated in $2.5\,\%$ (w/v) glutaraldehyde. The glutaraldehyde was diluted with PBS. $200\,\mu\mathrm{L}$ glutaraldehyde was sandwiched between a piece of parafilm and the coverslip, with the side coated with poly(ethylenimine) facing the solution. The coverslips were incubated for 1 hour before they were rinsed with ultrapure water and dried in a nitrogen flow.

Attaching Membrane fragment on Coverslips

The activated coverslips are mounted on custom Teflon culture rings using vacuum grease to seal. $30\,\mu\mathrm{L}$ of $0.2\,\mathrm{mg\,mL^{-1}}$ membrane fragments carrying hyaluronan synthase was pipetted into the holes of each culture ring. The membrane fragment suspension is diluted from $1\,\mathrm{mg\,mL^{-1}}$ with phosphate buffer (pH 7.3, $75\,\mathrm{mM}$ $\mathrm{NaKPO_4}$, $50\,\mathrm{mM}$ NaCl, $50\,\mathrm{mM}$ $\mathrm{MgCl_2}$). The coverslips were incubated for 1 hour.

Sample Storage

The solution in the sample holder was exchanged five times with storage buffer (pH 7.3, $50\,\mathrm{mM}$ tris, $500\,\mathrm{mM}$ NaCl, $20\,\mathrm{mM}$ DTT, $5\,\%$ glycerol). The samples were stored in $-20\,^{\circ}\mathrm{C}$. Samples should be used within two weeks.

3.2.2 Immobilizing HAS on Silica Microspheres

We used the same chemistry for silica microspheres as for glass coverslips. However, due to their tiny size, the microspheres require different handling than coverslips. First, we left the microspheres in suspension throughout the preparation procedure. The microspheres were under constant stirring using a magnetic stir bar. Second, we used piranha solution instead

of a plasma cleaner. Finally, to improve coating efficiency, we used dialysis to remove excessive tris(hydroxymethyl)aminomethane from the storage buffer. After modified the microspheres with glutaraldehyde, the surface of the microspheres forms covalent bonds to amines. The amine groups in the tris buffer compete with the amine groups on the membrane fragments to attaching to the microspheres. The dialysis process took place in parallel with the chemical modification steps on the microspheres. By the end of the dialysis, the microspheres had been modified with glutaraldehyde.

Piranha Cleaning

We prepared a $90\,^{\circ}\mathrm{C}$ water bath on a stirring hot plate. We added $100\,\mathrm{mg}$ monodisperse silica beads(Cospheric LLC, $1.8\,\mathrm{g\,cm^{-3}}$, d_{50} =7.75 µm, CV=3.7 %, $< 1\,\%$ doublets) to $1\,\mathrm{mL}$ $30\,\%$ H_2O_2 in a $1.5\,\mathrm{mL}$ centrifuge tube. Next, we briefly vortexed to suspend the beads and then put the tube in a sonicating water bath for 15 minutes to disperse the beads. We added a stir bar and three mL sulfuric acid in a disposable glass vial ($22\,\mathrm{mL}$, VWR 470206-384). We gently pipette the 1 mL beads suspended in $30\,\%$ H_2O_2 into the vial. During the pipetting process, we slowly vortex the vial to mix the solution. Then we secured the vial with a clap in the stirring hot water bath. We let the piranha cleaning to last 2 hours during which we maintain the level of the water bath. Finally, we slowly added 10 mL ultrapure water to the vial and turned off the heating and stirring. We left the vial overnight and waited for the microspheres to settle.

On the next day, we used a glass pipette tube to remove most of the piranha solution. Then we turned on stirring to suspend the beads. We transfer the beads to a glass centrifuge tube. Using a swing bucket centrifuge, we exchanged the solution with ultrapure water for seven times and checked that the pH of the solution is above 6.

Coating Polyethylenimine on Silica Microspheres

We added poly(ethyleneimine) to a final concentration of $2.5\,\%$ w/v. The suspension was stirred for 2 hours before washed seven times with ultrapure water.

Modifying Silica Microspheres with Glutaraldehyde

We added glutaraldehyde to a final concentration of $2.5\,\%$ w/v. The suspension was stirred for 2 hours before washed seven times with ultrapure water.

Attaching Hyaluronan Synthase on Silica Microspheres

We exchanged the tris-based storage buffer into a phosphate buffer before mixing the membrane fragments with the beads modified with glutaraldehyde. We used a Slide-A-Lyzer$^{\mathrm{TM}}$ MINI Dialysis Device to perform the buffer exchange in an ice box ($4\,^{\circ}\mathrm{C}$). This dialysis device is ideal for low volume sample. The low temperature elongates the lifetime of the hyaluronan synthase. We refreshed the phosphate buffer twice with a $45\,\mathrm{min}$ interval to maintain a high concentration gradient of tris across the dialysis membrane.

3.3 Reinforced Hyaluronan Grafting

To form covalent bonds between the hyaluronan polymers and the grafting surface, we used carbodiimide conjugation to crosslink the carboxyl group on hyaluronan to the primary amine group ($-\mathrm{NH_2}$) on the grafting surface.

At the end of hyaluronan synthesis, we exchanged the solution with pH 7.0 $75\,\mathrm{mM}\,\mathrm{NaKPO_4}$, $50\,\mathrm{mM}$ NaCl. Here we did not add DTT to the buffer because DTT is more reactive to EDC than carboxyl group and reduces reaction efficiency. Next, we added $100\,\mathrm{mM}$(final concentration) EDC(carbodiimide) and $50\,\mathrm{mM}$(final concentration) sulfo-NHS to the sample. EDC and sulfo-NHS are high moisture sensitive. The containers were allowed to reach room temperature before opening to avoid water condensation. Both EDC and sulfo-NHS

were dissolved right before adding to the sample. After $30\,\mathrm{min}$ of reaction, we exchanged the solution with newly dissolved EDC and sulfo-NHS. This refreshing procedure is repeated after $30\,\mathrm{min}$ of reaction. We left the sample overnight at room temperature.
On the next day, we exchange the solution with pH 8.0 $50\,\mathrm{mM}$ borate buffer to quench the crosslinking reaction for $2\,\mathrm{h}$. Then we exchanged the buffer with PBS.

3.4 Hyaluronan Synthesis Activation and Quenching

3.4.1 Activating hyaluronan synthesis

The storage buffer was exchanged with activation buffer (pH 7.3, $75\,\mathrm{mM}$ $\mathrm{NaKPO_4}$, $50\,\mathrm{mM}$ NaCl, $50\,\mathrm{mM}$ $\mathrm{MgCl_2}$, $0.1\,\mathrm{mM}$ Ethylenediaminetetraacetic acid (EDTA)). After warming the sample for $45\,\mathrm{min}$, uridine 5'-diphosphoglucuronic acid trisodium salt(UDP-GlcA, Sigma-Aldrich U6751) and uridine 5'-diphospho-N acetylglucosamine sodium salt(UDP-GlcNAc, Sigma-Aldrich U4375) are added to a final concentration of $5\,\mathrm{mM}$.

3.4.2 Quenching hyaluronan synthesis

The activated buffer was thoroughly exchanged with quenching buffer (pH 7.3, $75\,\mathrm{mM}$ $\mathrm{NaKPO_4}$, $50\,\mathrm{mM}$ NaCl, $20\,\mathrm{mM}$ EDTA). The solution in the sample holder was pulled out as thorough as possible via pipetting. The sample holder was refilled with the quenching buffer. The solution was mixed by gently pipetting the liquid up and down for a few times. This buffer exchange procedure was repeated seven times.

3.5 Particle Exclusion Assays

The classical particle exclusion assay [53] is a method to visualize the transparent pericellular matrix. In that approach, fixed red blood cells are added to cells with a pericellular matrix. The matrix prevents the red blood cells from reaching the cell surface. Here we use an improved assay developed in our lab to characterize the hyaluronan brush structure

which is similar to the classical particle exclusion assay the quantitative particle exclusion assay [54, 55]. Instead of using red blood cells which have irregular shapes, we used fluorescent polystyrene spheres of monodisperse sizes ranging from $20\,\mathrm{nm}$ to $200\,\mathrm{nm}$. In the limit of large diameter, spheres are excluded from the brush. In the limit of small diameter, spheres can penetrate the brush and reach the grafting surface. We gained insights into the structure of the polymer brush from combining the penetration profiles of spheres of different sizes. To facilitate image analysis, we added $10\,\mathrm{kDa}$ fluorescent dextran. According to the size of dextran reported in a paper by Rubinstein [56], we estimated that the hydrodynamic diameter of this $10\,\mathrm{kDa}$ dextran to be $4.5\,\mathrm{nm}$. However, it is likely that the dextran is rather polydisperse [56]. In the later experiments, we used $20\,\mathrm{nm}$ fluorescent latex nanoparticles to label the grafting surface. They non-specifically aggregate to the grafting surface and produce a peak in the vertical intensity profile. We used low concentrations of these nanoparticles such that they produced negligible osmotic pressure [56].

3.5.1 Imaging Protocol of Hyaluronan Brush with Nanoparticles

FluoSpheres (Molecular Probes, Inc, Carboxylate-Modified) were added to a final concentration of 0.7% w/v (green, $20\,\mathrm{nm}$ (Catalog number: F8787); green, $100\,\mathrm{nm}$ (Catalog number: F8803); red, $200\,\mathrm{nm}$(Catalog number: F8810)). Fluorescent dextran (Molecular Probes, Inc), Alexa Fluor 647, $10\,\mathrm{kDa}$ to a final concentration of $33\,\mu\mathrm{g\,mL^{-1}}$. $0.007\,\%$ w/v $20\,\mathrm{nm}$ nanoparticles were added in the experiments where the grafting surface needed to be labeled. Optical characterization of the brush was made using confocal images on a scanning laser confocal microscope (FV1000, Olympus, Tokyo, Japan; Objective: PlanApo N, 60X/1.42 NA oil) for high-resolution confocal images. The scanning laser confocal system is capable of reducing the sweep angle of the illuminating laser and renders zoom factor up to 8x on top the magnification from the objective. When imaging planar polymer brushes, we used a $100\,\mathrm{nm}$ vertical step. When imaging the polymer brushes on microspheres, we used a $30\,\mathrm{nm}$ to $60\,\mathrm{nm}$ horizontal pixel size and $470\,\mathrm{nm}$ vertical step. A $4\,\mu\mathrm{m}$ thick z-stack

was taken for each microsphere. The vertical range was selected to at minimum measure to slightly above the bead center. Unless stated otherwise, we finished the imaging within $1\,\mathrm{h}$ since quenching hyaluronan synthesis to avoid significant desorption of the hyaluronan polymers.

3.5.2 Image Analysis

As is shown in Figure 3.2C, we selected the XY slice with the largest bead radius to analyze the brush. We estimate the thickness of the brush to be the difference between the radius of the exclusion area and the radius of the microsphere.

Dextran

We used the differences of Gaussian algorithm [57] to locate the edge of the microspheres using the dextran channel. Two blurred images were obtained by convolving the original image with a $\sigma = 25\,\mathrm{pixel}$ and a $\sigma = 5\,\mathrm{pixel}$ Gaussian kernel. The center of the microsphere was taken as the centroid of the segmented image converted from $\sigma = 25\,\mathrm{pixel}$-blurred image using Otsu's method [58]. From this center, we calculated the azimuthally averaged intensity profile (Figure 3.2B) of an image obtained by subtracting the two blurred images (Figure 3.2A). Intensity near the bead center was used as the reference to locate the edge of the microsphere.

Surface-Bound Nanoparticles

In each XY slices, the surface-bound nanoparticles appeared as a bright ring around the microsphere. We segmented the image using Otsu's method and located the bead center. From the center, we calculated the azimuthally averaged intensity profile. The peak in the profile was identified as the surface of the microsphere.

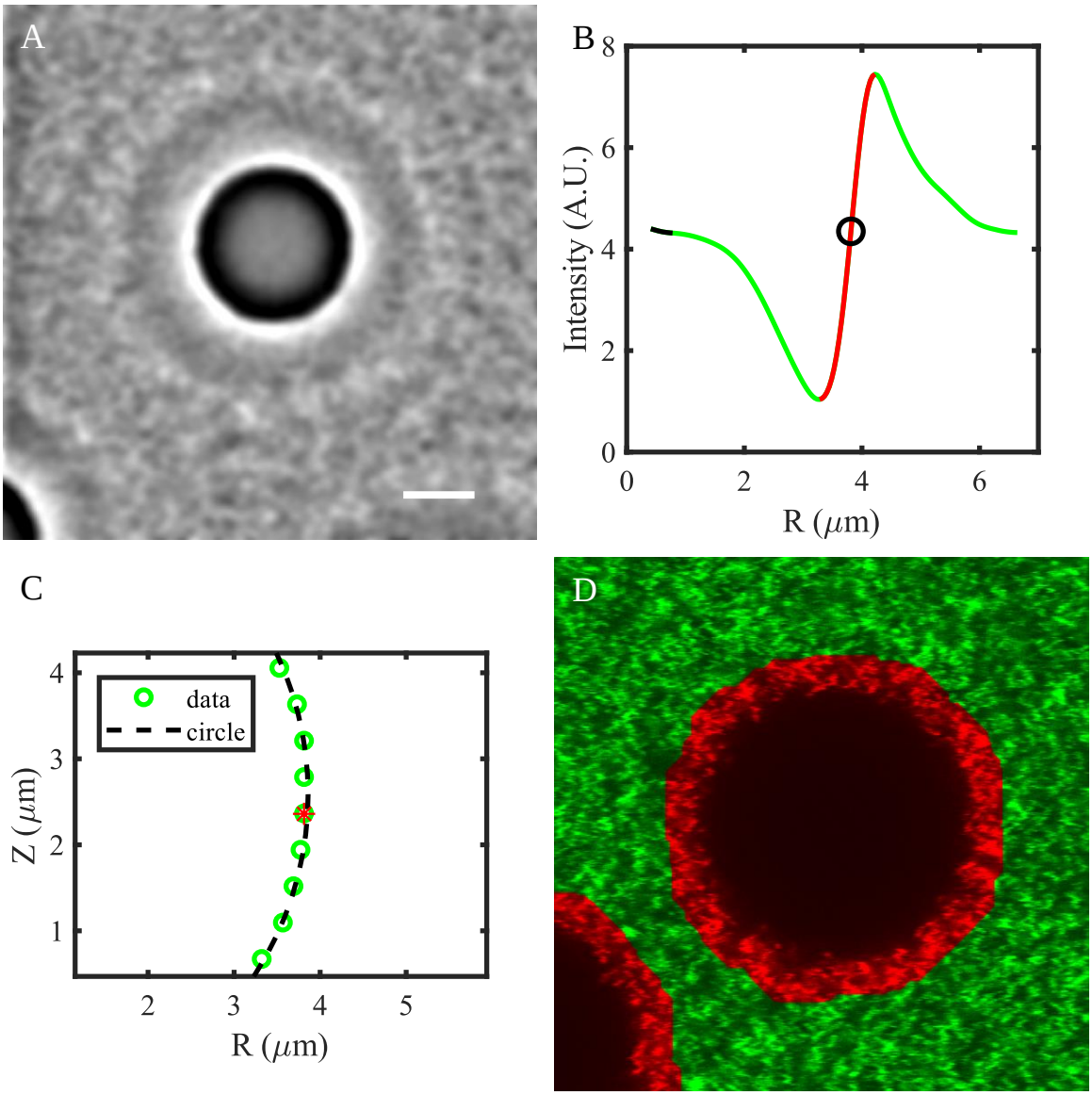

Figure 3.2: Intermediate results of image processing for particle exclusion assay on spherical polymer brush: **A** Difference of Gaussians of the dextran channel; **B** Radial profile of **A**; **C** Radius of microsphere measured at different z position; **D** pre-segmentation of the 200 nm nanoparticle channel. (the non-brush region(green) was used to calculate intensity for profile normalization).

Nanoparticle Distribution Profiles in the Brush

First, starting from the center of the bead found in the image channel of dextran or surface bound nanoparticles, we calculated the azimuthally averaged intensity of the channel of the excluded nanoparticles. The intensity profile was then normalized by the average intensity in the non-brush region (Figure 4.3D).

Analyzing Z-Stack Images

Starting from the surface of a microsphere, the region where the density of nanoparticles is smaller than the density sufficiently far away from the microsphere indicates the presence of polymer brush. It is upon convention to define the boundary of the exclusion region and we will discuss below. Because of the spherical symmetry of the microsphere and the brush, an image slice through the center of the microsphere provides adequate information to analyze the exclusion of nanoparticles. From a Z-stack image taken by a laser scanning confocal microscope, the XY slice of the maximum microsphere radius was identified as the central slice. At most we could miss the center by $350\,\mathrm{nm}$ which result in a negligible, $15\,\mathrm{nm}$, underestimation in bead radius. The data analysis is fully automated which greatly reduces the risk of human bias. We compared the radii measured against values provided by the manufactures. For $10\,\mu\mathrm{m}$ latex microspheres, the radius we measured was $10.47(15)\,\mu\mathrm{m}$ [1] (N = 48) which agreed with the manufacturer's value $10.52(25)\,\mu\mathrm{m}$. For $8\,\mu\mathrm{m}$ glass microspheres, we obtained $8.02(22)\,\mu\mathrm{m}$ (N = 56) which also agreed with the manufacture's value $7.76(28)\,\mu\mathrm{m}$. We checked that, in each experiment of different brush thickness, the radii of the grafting microspheres were consistent with the value provided by the manufacturer.

[1] The uncertainty is represented by the standard deviation.

3.6 Miscellaneous Protocols

3.6.1 Chemical Handling

All the chemicals were stored according to the manufacturer's instruction unless stated here. Dithiothreitol (DTT) and sulfo-NHS were stored in a sealed bag with silica gel in a $4\,^{\circ}\mathrm{C}$ fridge. N-(3-Dimethylaminopropyl)-N'-ethylcarbodiimide hydrochloride (EDC) was aliquoted upon arrival into cryogenic storage vials and stored in a $-20\,^{\circ}\mathrm{C}$ freezer. DTT, sulfo-NHS and EDC solutions were prepared right before use. $0.3\,\mathrm{M}\ \mathrm{NaKPO_4}$ was stored in a $4\,^{\circ}\mathrm{C}$ fridge for up to 2 months. All other buffers were stored at room temperature. Premixed buffer ($\mathrm{NaKPO_4}$, glycerol, EDTA, NaCl) was used within two weeks. NaCl solution, $\mathrm{MgCl_2}$ solution, EDTA solution and polyethyleneimine (PEI) solution, was used within six months. Borate buffer and MES buffer were used within a month.

3.6.2 Hyaluronan Binding Protein

Rauch et al. designed a cDNA strand for a protein where a green fluorescent protein (GFP) is connected to the hyaluronan-linking domain of neurocan [59]. The resulting protein, called GPFn, specifically binds to hyaluronan. Aggrecan (from bovine articular cartilage, Sigma A1960) is a proteoglycan similar to neurocan and share a similar structure, including a hyaluronan-linking domain. The hyaluronan binding domain (G1) in the proteoglycan aggrecan and the GFPn have critical disulfide bonds. If these disulfide bonds are reduced, the proteins lose the binding activities [60, 61, 62]. As a result, we need to wash out the reducing agent DTT in the solution before adding the hyaluronan binding proteins. To each assay of $80\,\mu\mathrm{L}$ final volume, we added $5\,\mu\mathrm{L}$ GFPn from the first elution process. We added aggrecan to a final concentration of $0.1\,\mathrm{mg\,mL^{-1}}$. We also added BSA to a final concentration of $10\,\mathrm{mg\,mL^{-1}}$ to block the grafting surface.

Hyaluronan Binding Proteins

First, we identified the center of the microspheres by segmenting either the image of the dextran channel or the GFPn channel using Otsu's method [58]. Second, we calculated the azimuthally averaged intensity profiles of each fluorescent molecules. To process the images where beads were close to each other, the azimuthal average was calculated for each 30° conical sector. We only used sectors clear of neighboring beads (Figure 4.5). In the case where the dextran channel was not present, the peak in the GPFn profile was identified as the surface of the microsphere. We define the hyaluronan region as the region where the intensity is higher than the background intensity by twice the standard deviation of the background region.

3.6.3 Adding SDS Detergent

When breaking up the membrane fragments and hyaluronan synthase, we gently added $1\,\mathrm{mg\,mL^{-1}}$ SDS(Sodium dodecyl sulfate, Sigma-Aldrich L6026). The process was used to check the formation of covalent bonds between hyaluronan and the coating surface. Please refer to section 3.3.

3.6.4 Hyaluronidase Enzyme Treatment

To digest hyaluronan in the brush, we added 0.5 unit of bacterial hyaluronidase (from Streptomyces hyalurolyticus, Sigma-Aldrich H1136) or 20 units of bovine hyaluronidase (from bovine testes Type I-S, Sigma-Aldrich H3506) to $80\,\mu\mathrm{L}$ samples. In experiments sensitive to flow or bursts of osmotic pressure associated with sudden injection of concentrated molecules, we injected bovine hyaluronidase using a glass pipette connected to a syringe pump which pumped $6\,\mu\mathrm{L}$ at a rate of $12\,\mu\mathrm{L}/\,\mathrm{min}$. In experiments where hyaluronan regeneration was desired, $20\,\mathrm{mg\,mL^{-1}}$ bovine serum albumin (BSA) was added together with hyaluronidase to block the non-specific binding of hyaluronidase.

3.6.5 Scanning Electron Microscopy

Membrane fragments were immobilized on $5\,\mathrm{mm}$ by $5\,\mathrm{mm}$ by $1\,\mathrm{mm}$ glass slides using the method described above. Next, the slides were immersed in $2.5\,\%$ w/v glutaraldehyde for $1\,\mathrm{h}$. Then the slides were rinsed with ultrapure water and air-dried. Finally, the slides were coated with carbon using chemical vapor deposition (Cressington 108A carbon coater) and imaged with a Scanning Electron Microscopy (Zeiss Ultra 60 SEM). Dr. Joanna Tsao from Behrens Lab (GaTech) imaged the samples.

Estimating Coverage of Membrane Fragments

We process the SEM image of a planar surface coated with membrane fragments where the hyaluronan synthase was embedded. The image was de-noised using the Wiener method (Matlab®function wiener2). We generate a binary image using adaptive thresholding (Matlab adaptthresh(img, 0.6)).

The binary image contains a lot of small objects which are not the membrane fragments. To screen these non-fragment objects, we used a different method to generate a binary marker image. Ideally, the bright pixels in the marker image is a subset of the perfect segmentation. We used the Sobel method [63] (Matlab edge(img,'sobel')) to detect the edges of fragments. This algorithm did not generate the complete edges of the fragments, but the result is sufficiently good as a marker of the fragments. Using the marker image, we used Matlab's immreconstruct function to pick the objects which are more likely to be the membrane fragments.

3.7 Diffraction Based Microsphere Tracking

We adopted a diffraction-based tracking method for microspheres [64] to study the dynamics of the brush height with high time and space resolution and statistics with minimal labor (see Figure 3.5). This method is commonly used in magnetic tweezers setup. Weakly co-

herent light from an LED is collimated to achieve parallel illumination. Under the parallel illumination, light scattered by the beads interferes with the un-scattered light. The interference generates concentric diffraction rings below the beads (between the beads and the objective). This diffraction pattern of rings is sensitive to the position of the focal plane of the objective. To infer the height of a bead, the diffraction ring pattern is compared with a look-up table containing the diffraction ring patterns as a function of objective position for that specific bead. The patterns are highly sensitive to the size of the microsphere, thus we need to record the patterns of each microspheres. A set of tracking beads are placed on the top of the brush. Another set of reference beads are immobilized on the coverslip. We subtract the motion of the reference beads from the motion of the tracking beads to measure the change in the brush height. More details are discussed below.

3.7.1 Challenges

Although the protocols for making an enzyme-synthesized hyaluronan brush and the single molecule manipulation using magnetic tweezers are established, we faced two challenges when combining the two, and in particular, in establishing the desorption experiment to study the length-dependent release of hyaluronan from hyaluronan synthase.

Immobilizing Reference Beads

We needed to securely immobilize both hyaluronan synthase and reference beads on the coverslip. Some methods to immobilize beads may disrupt either the activity of hyaluronan synthase or the uniformity of protein coating. The hyaluronan brush also expels weakly bound beads.

Hyaluronan Removal

To minimize the brush disturbance by the tracking beads, the tracking beads are not tethered to the hyaluronan brush. As a result, the freely diffusing tracking beads follow Brownian

motion in all dimensions. It is crucial to minimize flow during the measurement to keep the beads localized. Further, we measured that the vertical Brownian motion is on the order of $100\,\mathrm{nm}$(Figure). This jiggling greatly reduces the potential precision of the vertical look-up table, which can reach $5\,\mathrm{nm}$ for fixed beads. As a result, we determined it is best to establish the look-up table without the brush in order to obtain optimal z-resolution.

We cannot build the look-up table before the synthesis because the calibrated beads will be washed away during the extensive washing stage required to halt the hyaluronan synthesis. Thus we remove the hyaluronan and then build the lookup table at the end of the desorption measurement. This led to the need for a method to efficiently remove hyaluronan but not to cause large displacement of the unbound tracking beads.

3.7.2 Microspheres

We used $4\,\mu\mathrm{m}$ glass beads as tracking beads and $3.2\,\mu\mathrm{m}$ latex beads were immobilized on the coverslip to track the position of the coverslip.

There are a few reasons we chose these two set of microspheres. First glass microspheres have a higher density than latex microspheres and water and hence sink faster due to gravity than latex microspheres. Second, the latex beads can be conveniently immobilized onto the coverslip via partial melting. This immobilization method is fully compatible with the chemistry to immobilize hyaluronan synthase. Finally, the two kinds of beads produce distinct diffraction patterns in that, within the working range, a glass bead has a bright center while a latex bead has a dark center. This difference in the patterns allows for simple and robust automatic bead recognition which facilitates to find a field of view with a reasonable number of tracking beads and reference beads.

3.7.3 Sealing the Sample Holder

We mounted the coverslip on a custom Teflon culture ring. After quenching the synthesis and adding tracking beads, we made a $6\,\mathrm{mm}$ square coverslip using a glass cutter and

mount it on the top of the Teflon ring while leaving a $3\,\mathrm{mm}$-wide opening. This top coverslip eliminates lensing effect of the solution in the sample which distorts the parallel illumination. The opening provides access to the solution. We then filled the sample until the solution fully wet the top coverslip. The $3\,\mathrm{mm}$ opening was covered with mineral oil to reduce evaporation. We did not maintain a high level of humidity in the chamber during the desorption measurement to avoid water condensation on the top coverslip, , but since the sample was covered with mineral oil, the risk of evaporation from the sample was already minimized.

3.7.4 Building the Microscope

We used a homemade microscope to implement this diffraction based tracking method (Section 3.5). The framework of the microscope was designed and built by a previous postdoc Dr. Jan Schimgeour (see Figure 3.3). We modified three major components of the microscope: illumination, objective housing and the optical path for image collection (see Figure 3.4 for the modified microscope).

Illumination

We used a LED (ThorLabs M625D2, $625\,\mathrm{nm}$, $700\,\mathrm{mW}$) as the light source. The LED was powered by a LED driver (T-cube LED driver, ThorLabs). The light is collimated using a lens (D = 1 inch, f = $5\,\mathrm{cm}$, AC254-050-A, ThorLabs). When adjusting the position of the lens and making the light collimated (parallel), we projected the image of the LED chip onto a distant wall.

Objective Housing

We mounted a Nikon objective (Apo, tirf, 60x/1.49, oil) on a piezo scanner (Physik Instruments, P-721.CDQ). We also raised the motorized stage to accommodate the height of the objective. We used a paper tube to suppress reflection from the metal components which

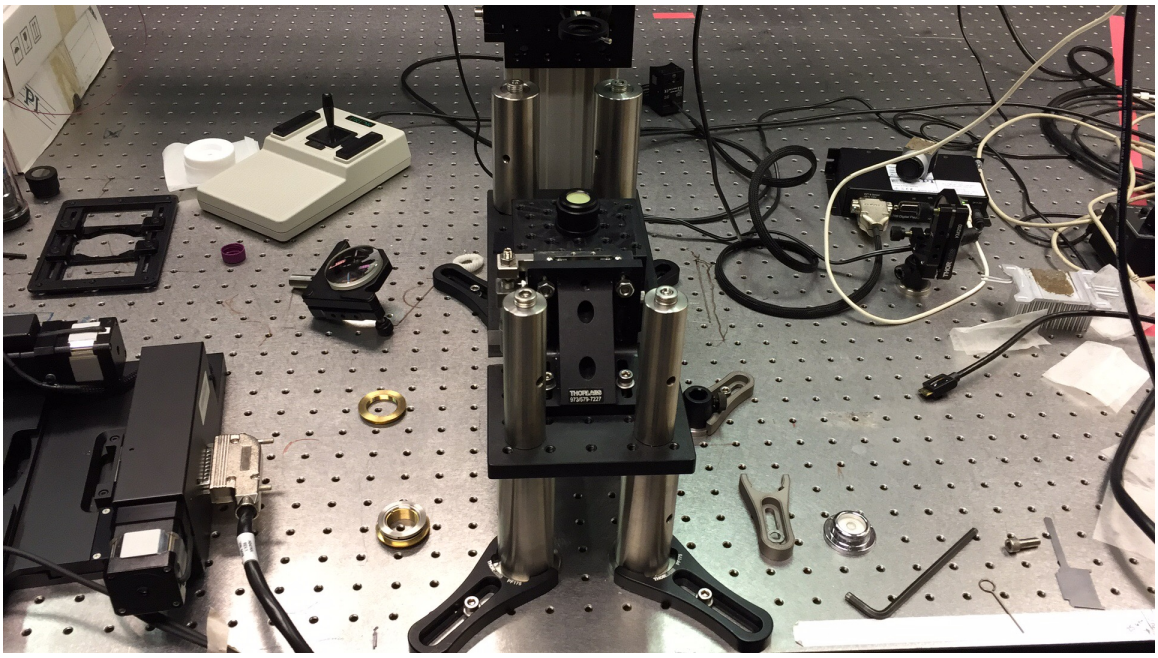

Figure 3.3: Base of the microscope.

produce hot spots in the image.

Image Collection

We used a collection lens (D = 2 inch, f = $10\,\mathrm{cm}$, AC508-100-A, ThorLabs) to achieve a 30X final magnification. This magnification provides sufficient tracking resolution and relatively large field of view which is ideal for gathering good statistics. We used a CMOS camera (Basler, acA1300-200um, Python 1300 sensor, 8-bit readout, $4.8\,\mu\mathrm{m}$ pixel size, 1280 by 1024 pixels, 200 fps) to capture the image.

Alignment

We used a laser collimator for a telescope (Astromania) to facilitate aligning the microscope. The laser is mounted in the illumination slot.

First, we aligned the laser with the objective holder (Figure 3.6**A**). An alignment tool with a mirror was mounted on the objective holder. The light should reflect from the center of

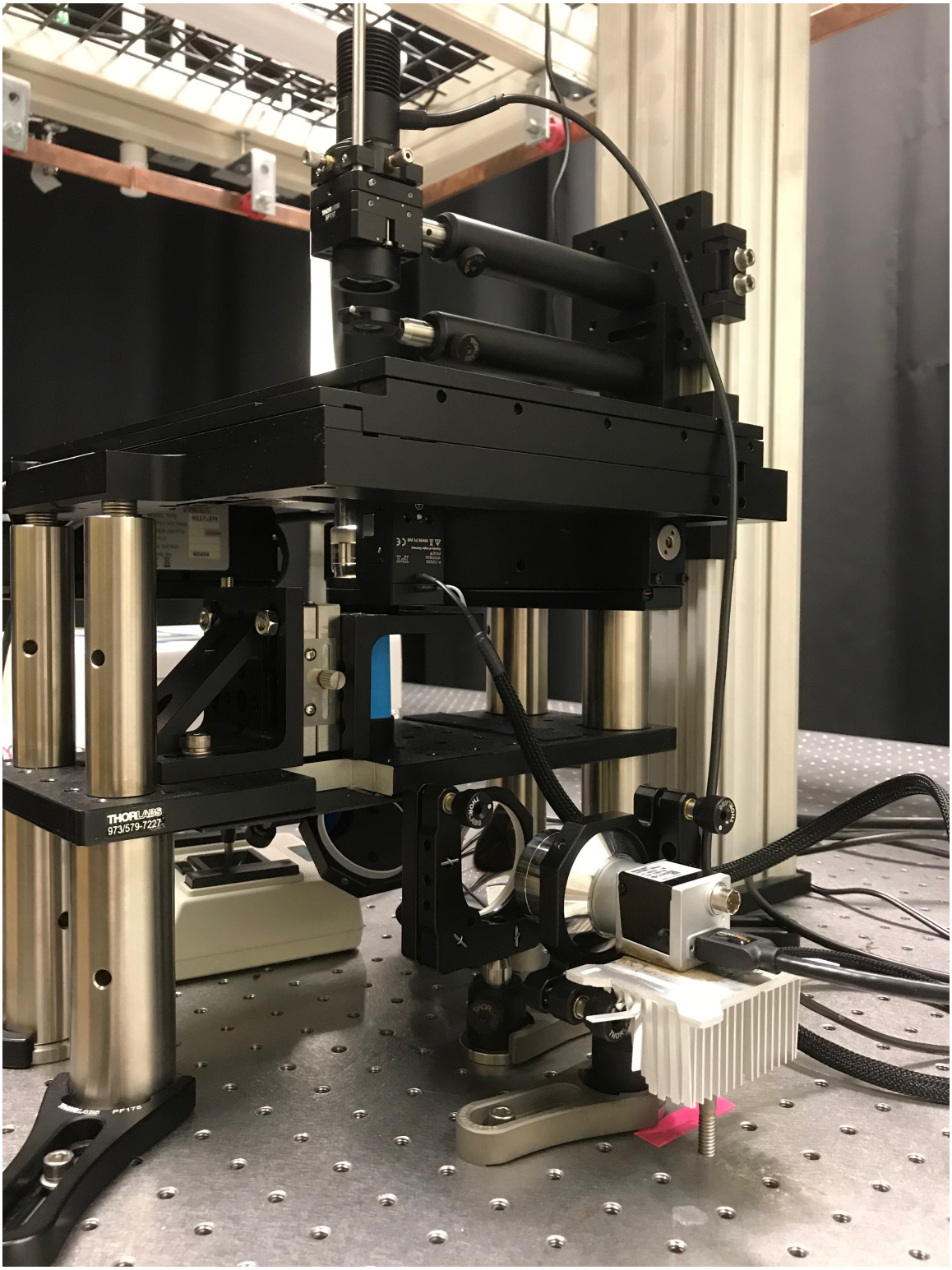

Figure 3.4: Fully assembled microscope.

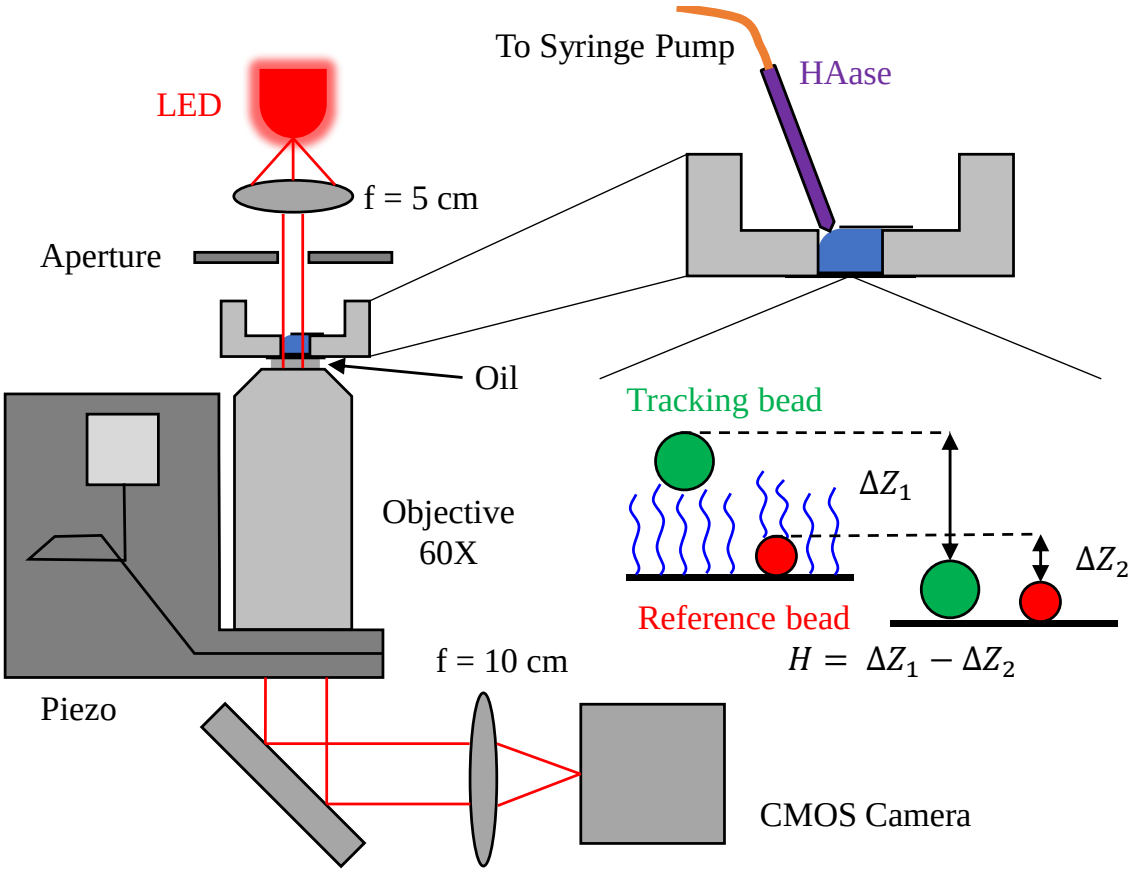

Figure 3.5: Schematic representation of the experimental configuration for measuring the height of hyaluronan polymer brush. A diffusion cell is built up from two microscope coverslips mounted on the hole of a custom built Teflon ring. The top coverslip does not completely seal the cell, leaving a gap which allows for injection of hyaluronidase using a syringe pump. Latex reference beads are immobilized on the surface of the bottom coverslip. In the vicinity of the reference beads, tracking beads are located. The tracking beads are made of glass and settle on the top of the brush. Above the cell, collimated LED provides parallel illumination. Below the bottom coverslip, an objective is located. The objective seats on a piezoelectric scanner which adjusts the vertical position of the focal plane. A CMOS camera records the diffraction patterns of the beads from the focal plane of the objective.

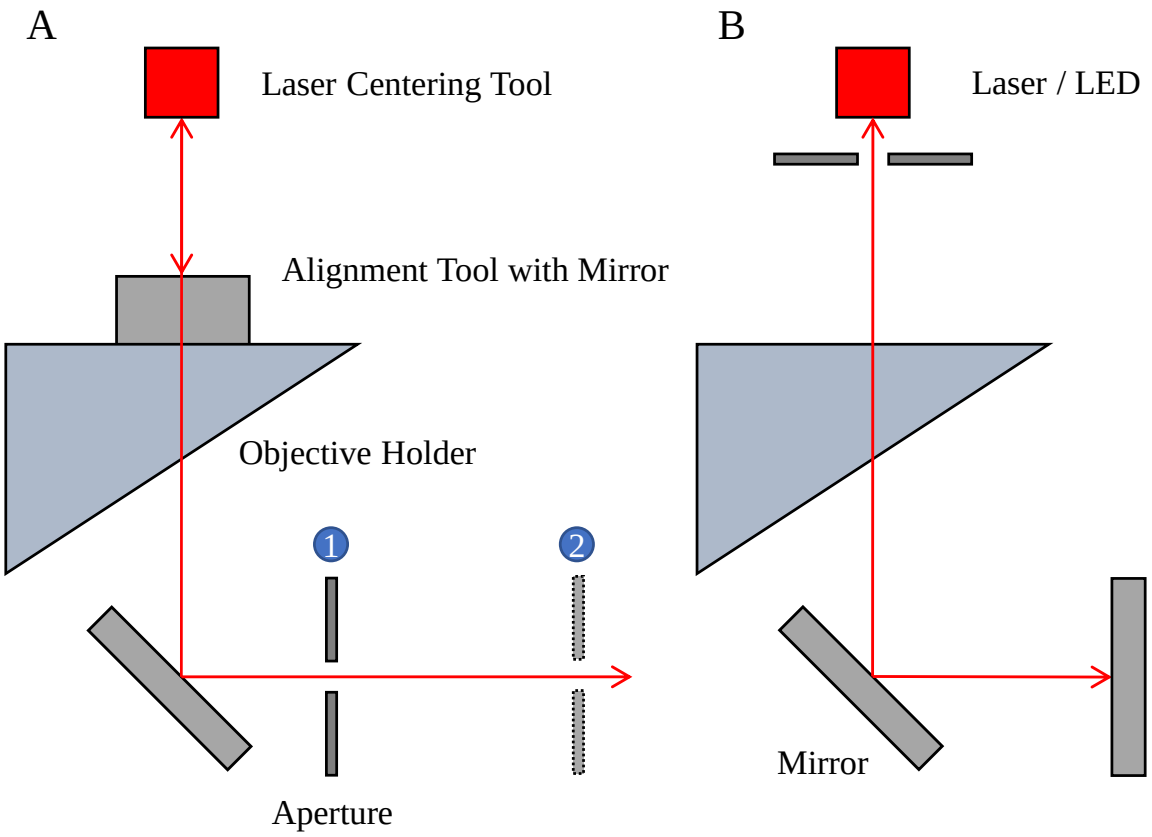

Figure 3.6: Schematic representation of the alignment procedure. **A** Procedure to align the centering tool and the $45°$ mirror. **B** Procedure to align collection lens, the camera and the illumination system.

the alignment tool back to the laser. The objective holder defines the vertical light path of the microscope.

Second, we align the $45°$ mirror (D = 2 inch, BB2-E02, ThorLabs) at the base of the microscope (Figure 3.6**A**). This mirror defines the horizontal light path of the microscope. We centered the aperture at position 1. Then we placed the aperture at position 2. We adjusted the mirror such that the light spot is halfway closer to the center of the aperture. We repeated this step until the light passed the aperture at the two positions. Now the reflected path was leveled.

Third, we aligned the holders for the collection lens and the camera (Figure 3.6**B**). We mounted a mirror of which center is labeled on of lens holder facing the alignment laser. We adjusted the position and angles of the holder such that the light hit the center of the mirror and the light was reflected back to the laser. Then we unmount the mirror and place the camera at the back focal plane of the collection lens. The sensor in the camera is reflective, and we read position of the light spot from images captured by the camera

Finally, we aligned the illumination LED (Figure 3.6B).To do this, we mounted and aligned an aperture $2\,\mathrm{cm}$ above the temperature chamber (LiveCell, Pathology Devices) which holds the Teflon sample. We replaced the laser with the collimated LED and aligned it using the aperture we just mounted and the alignment tool on the objective holder.

3.7.5 Protocol for Microsphere Tracking Experiment

After seeding the quenched sample with tracking beads, we moved the XY stage until we found a field of view with at least three reference beads which are also at least $3\,\mathrm{mm}$ away from the injection gap. Next, we built $25\,\mu\mathrm{m}$ lookup tables of these reference beads which covers $5\,\mu\mathrm{m}$ above the beads and $20\,\mu\mathrm{m}$ below the beads at a $40\,\mathrm{nm}$ step. It usually took about $10\,\mathrm{s}$ to build the look-up table. We used these reference beads to maintain the focal plane of the microscope. Then we collected images for $2\,\mathrm{h}$ in 9 different regions. The nine regions consisted of a three by three grid of field of view. Each imaging cycle of the

total took approximately $4.5\,\mathrm{sec}$. After $2\,\mathrm{h}$, we carefully injected hyaluronidase through the injection gap. After another $2\,\mathrm{h}$ of imaging to wait for the hyaluronidase to deliver and degrade the brush, we built lookup tables which covered $15\,\mu\mathrm{m}$ below the beads for all the tracking and reference beads in all field of view using a $20\,\mathrm{nm}$ step. The look-up tables contain information for $15\,\mu\mathrm{m}$ below the beads.

3.7.6 Image Analysis

Preprocessing

Non-uniformity in the background caused by either non-uniform illumination or dusk on the optical elements alters the diffraction patterns and reduce the accuracy of locating the beads. A blurred image is obtained by convolving the original image with a $\sigma = 5\,\mathrm{pixel}$ Gaussian kernel. The original image is divided by the blurred image pixel by pixel.
Reflection from the tubes in the optical path causes glare in the center of the field of view at some focal height. We discarded the image within 100 pixels from the center.

Bead Identification

We used the feature of the concentric diffraction patterns from the microspheres. The concentric rings are either significantly brighter or darker than the background. We compare the value of each pixel with the global average intensity and standard deviation. In the segmentation step, a pixel is classified as foreground if its value deviates from the average intensity by twice the standard deviation. We then morphologically closed image using a 3-pixel disk. Next, we fill holes in the binary image. Finally, we selected round and isolated objects using Matlab's regionprops function. For each candidate object: its solidity should be larger than 0.9; its eccentricity should be smaller than 0.5; and the nearest object should be at least 40 pixels away. At a focal plane $5\,\mu\mathrm{m}$ to $15\,\mu\mathrm{m}$ below the microspheres, the $3\,\mu\mathrm{m}$ reference beads have dark centers while the $4\,\mu\mathrm{m}$ tracking beads have bright centers. Figure 3.7 shows a sample pre-processed image.

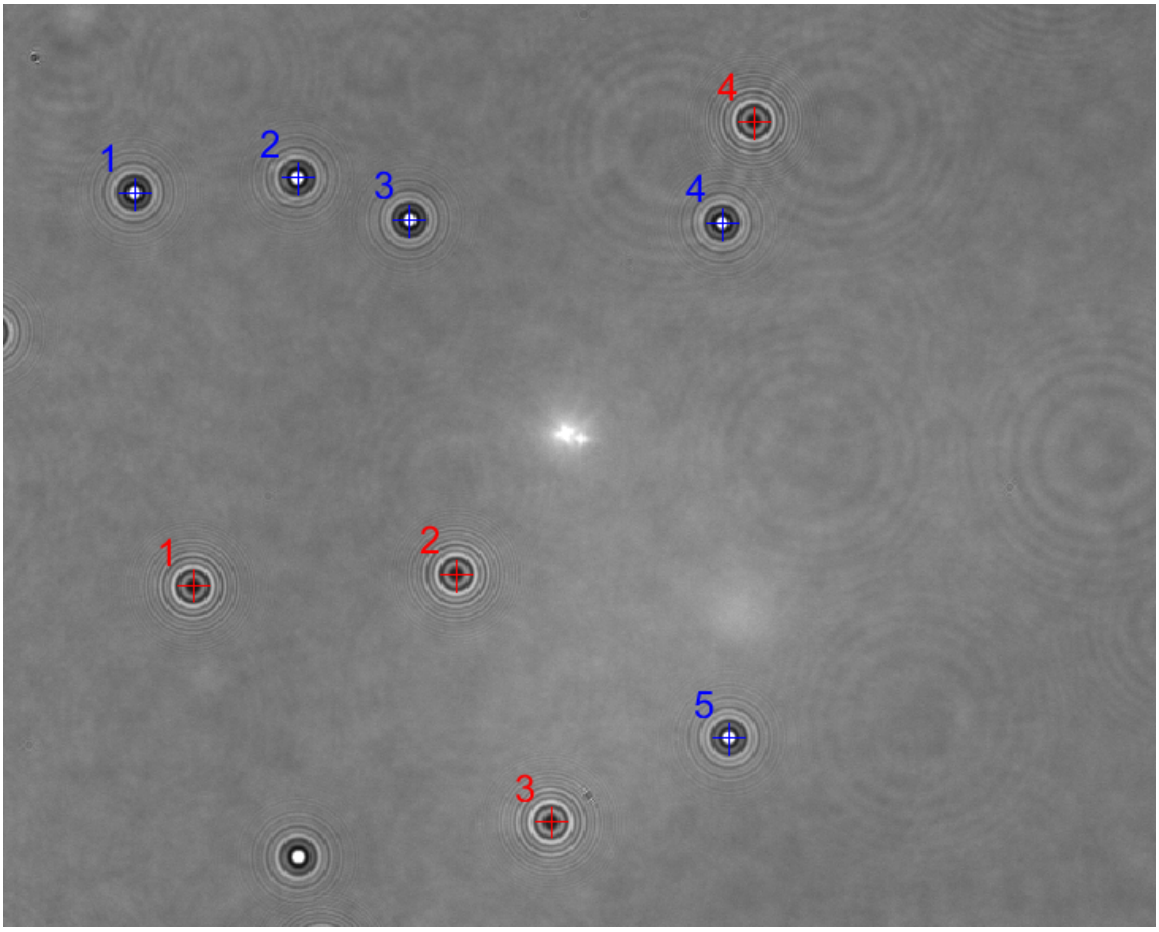

Figure 3.7: Snapshot from a desorption experiment. Tracking beads were numbered in blue, and reference beads were numbered in red.

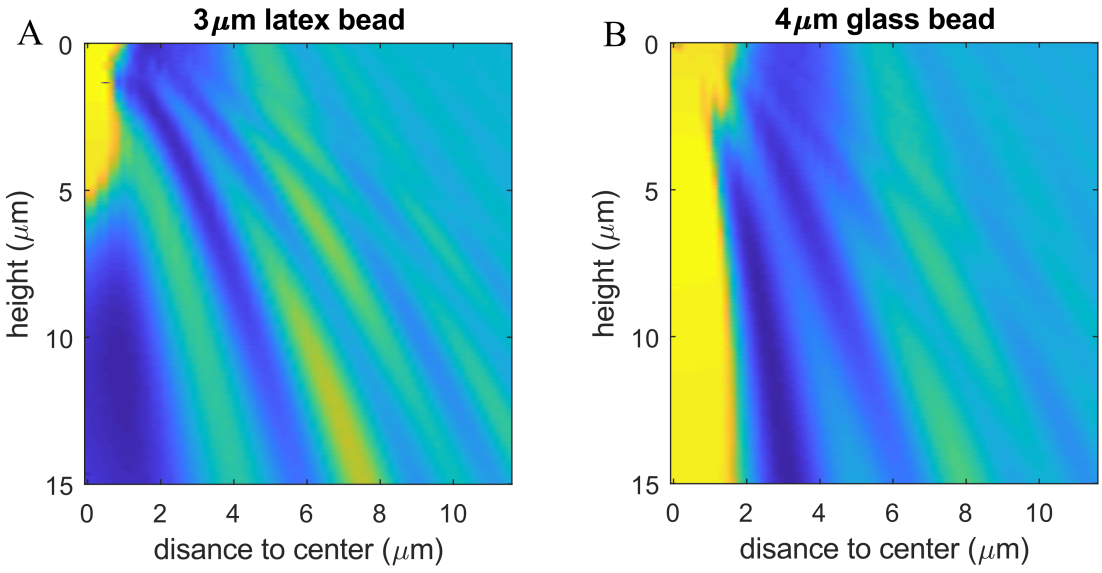

Figure 3.8: Look-up tables of a $3\,\mu\mathrm{m}$ latex bead (**A**) and a $4\,\mu\mathrm{m}$ glass bead (**B**).

Radially Symmetry Detection

We used Parthasarathy algorithm [65] which was later extended by Kovari [66] to identify the sub-pixel location of each microsphere using the collected images. In the absence of noises, the symmetric center is the intersection point of every gradient-line. When noise is present, we calculated the point which minimizes the weighted distance to each gradient-line. The weighting is proportional to the magnitude of the gradient and suppresses the skew in gradient direction for low-gradient-magnitude pixels because of noise. The centroid found in the object identification step was used as the initial guess of the center of symmetry.

Z-localization from Diffraction Patterns

From the symmetry center found in the previous step, we can compute the radially averaged intensity profile of a microsphere (Figure 3.8). By recording the profile at a series of focal plane, we build a lookup table (LUT) for each microsphere. The size of the LUT is M by N, where M is the number of focal planes and N is the length of the radial profile. The

next step is to determine the Z-position by comparing a measured profile with the LUT. We used the spline method from Kovari [66]. Each $\mathrm{M} \times 1$ column of LUT is fitted to a Reinsch-type smoothing spline (MATLAB, CSAPS), which is defined by minimizing the objective function,

$$E = p\sum_{j=1}^{M}(I_j^i - f(z_j))^2 + (1-p)\int |f''(t)|^2 dt, \tag{3.1}$$

where $\mathrm{I_j^i}$ is the intensity in the profile at the ith radial position at the jth focal plane. We chose the smoothing factor $\mathrm{p} = (1 - \Delta \mathrm{z}^3)^{-1}$ where Δz is the z spacing of the LUT. The LUT was fitted to N coupled spline equations $\mathrm{f^i(z)}, \mathrm{i} \in [1, \mathrm{N}]$. The sub-step location was found by solving the coupled equation in the least-square sense using the Gauss-Newton method. The measured profile $\hat{\mathrm{I}}$, is used to create the objective function to minimize,

$$\phi(z) = \sum_{i=1} N(\hat{I}^i - f^i(z))^2. \tag{3.2}$$

3.7.7 Calibration and Error Analysis

We identified three major sources of errors in tracking the vertical positions of the microspheres: generating the look-up table, interpolating the look-up table and unevenness in the background image. Detailed analysis can be found below.

Errors in the Look-up Table

We assume that, when building the look-up table, the vertical distance between adjacent images should be identical. This assumption is partially broken by the resolution of the piezoelectric scanner and the relative drifting between the objective and the coverslip. According to the specifications from the manufacturer, the scanner we use has a closed loop resolution of $0.7\,\mathrm{nm}$. We can estimate the drifting speed by tracking the positions of reference beads. Figure 3.9 shows the drifting at the beginning of an experiment. The average

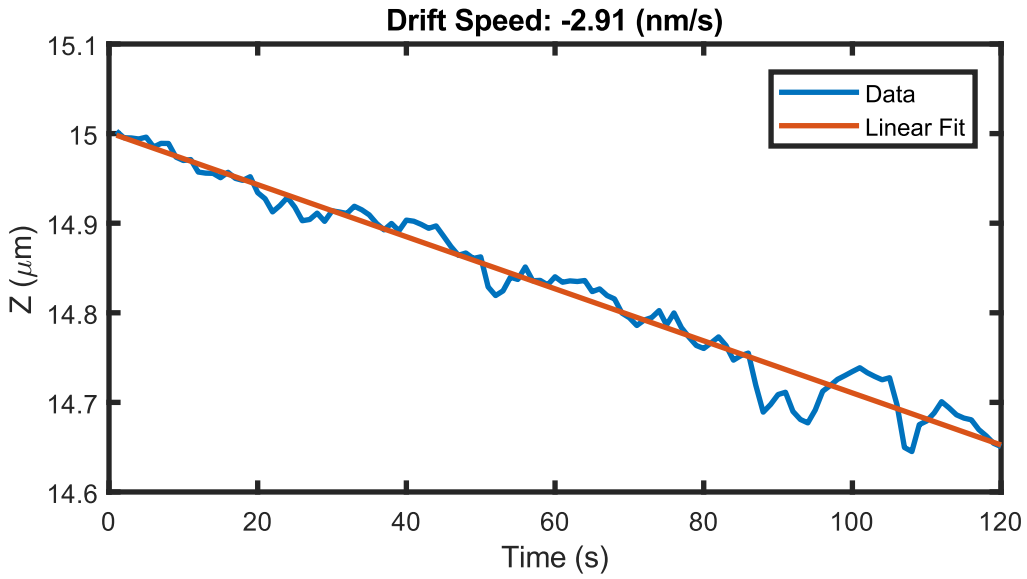

Figure 3.9: Vertical drift at the beginning of an experiment.

drifting speed was $-2.9\,\mathrm{nm\,s^{-1}}$. The drifting greatly slowed down later of the experiment when the temperature of the sample was fully equilibrated. The speed of building the image stacks for the look-up table is $1\,\mu\mathrm{m\,s^{-1}}$. Thus the relative error from drifting is on the order of $0.1\,\%$.

Another factor which affects the tracking resolution is the amount of information stored in the look-up table. We used a bright LED to utilize the dynamic range of the sensor fully. The tracking resolution also depends on how fast the diffraction pattern changes as a function of the vertical position. In general, smaller microspheres have faster-changing patterns but more blurred images which reduce the information stored in the image.

Tracking Error of Fixed Beads

We used the look-up table itself to estimate the total errors discussed above. We split the look-up table into odd-frames and even-frames by the index in the Z-stack. We built a new look-up table using the odd-frames and calculated the positions of each even-frame. As we know the z-position of every frame, we can compare it with the calculated z-position. The histograms of the errors for a latex microsphere and a glass microsphere is plotted in

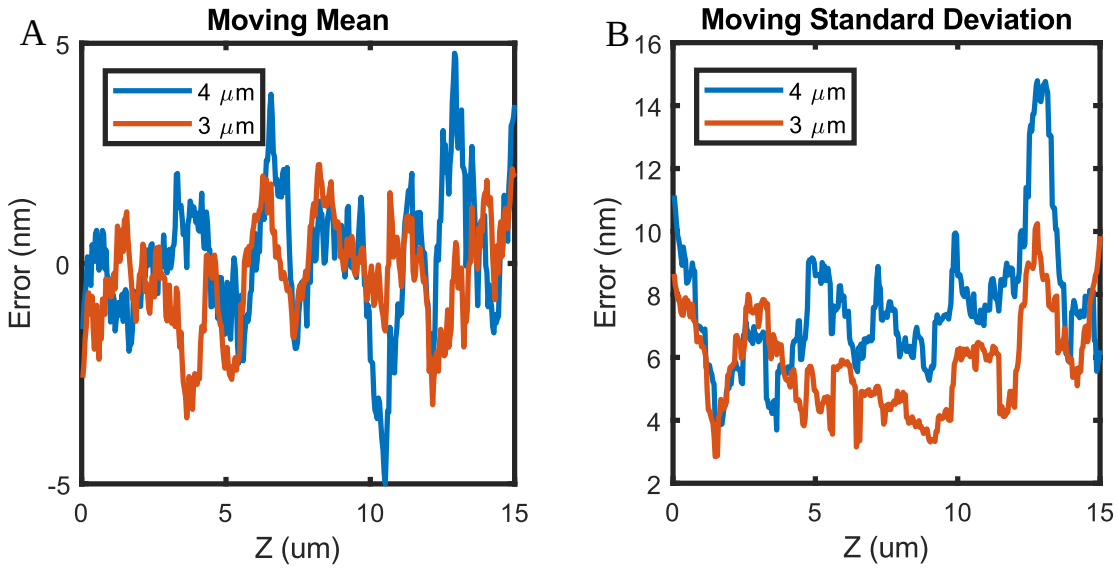

Figure 3.10: Z tracking error of a $3\,\mu\mathrm{m}$ latex bead (**A**) and a $4\,\mu\mathrm{m}$ glass bead (**B**). Moving mean and standard deviation are caculated in a window of 20 data points.

Figure 3.10.

Calibration Error from Horizontal Drift

The diffraction image collected by the microscope is susceptible to dust on the optical components. The alignment of the microscope is also not perfect. These imperfections make the background image not fully uniform, and the diffraction patterns of a microsphere may have a weak dependence on its position in the field of view. Compared with the reference beads, this error from horizontal displacement is more prominent on the tracking beads because they are free to diffusion and have larger displacement. The reference beads, on the other hand, only have a small range of motion. We estimated this error by comparing the look-up tables of the same bead taken at two diagonal positions in the field of view. The comparison algorithm of this cross-checking is the same as for the self-checking from above. The histograms of the errors for a latex and a glass microsphere is plotted in Figure 3.11.

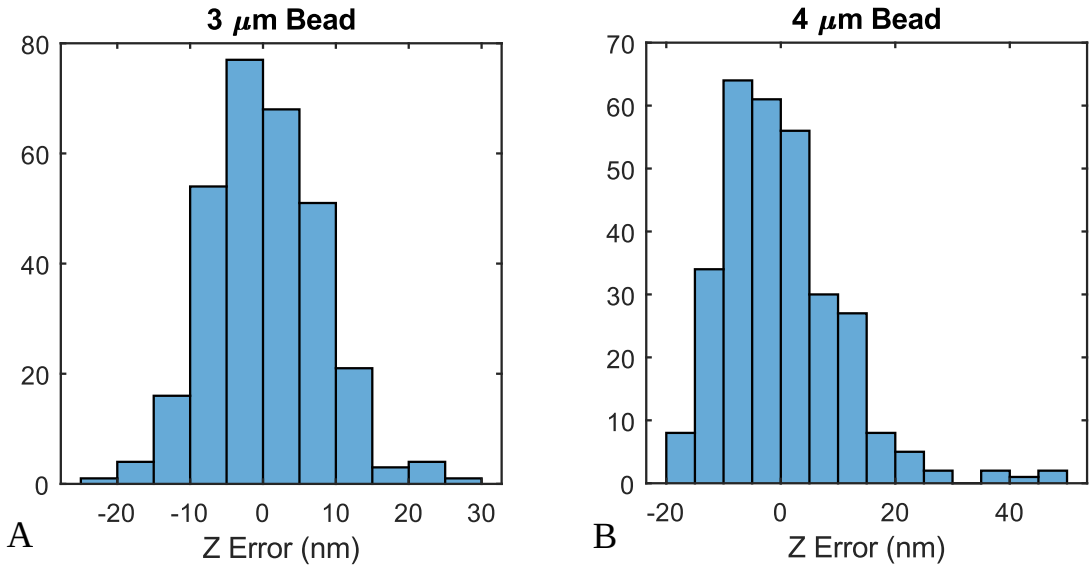

Figure 3.11: Comparing two LUTs of a bead taking at two diagonal positions in the field of view. **A** $3\,\mu\mathrm{m}$ bead, mean: $0.23\,\mathrm{nm}$, median: $-0.15\,\mathrm{nm}$, standard deviation: $7.7\,\mathrm{nm}$. **B** $4\,\mu\mathrm{m}$ bead, mean: $0.12\,\mathrm{nm}$, median: $-1.7\,\mathrm{nm}$, standard deviation $10\,\mathrm{nm}$.

3.7.8 Inferring Polymer Desorption from Brush Thickness Reduction

The density of grafted polymers, $mathrm\sigma$, is related to the height of a polymer brush as captured by the scaling law from polymer physics,

$$H = cL\sigma^{\nu}, \tag{3.3}$$

where H is the brush thickness, L is the average contour length of the hyaluronan polymers and σ is the grafting density of hyaluronan. In the presence of desorbing polymers (for releasing hyaluronan from hyaluronan synthase), the grafting density is changing in time and hence, so is the brush height. Since the height is detectable, we can estimate the rate of hyaluronan release by taking the time derivative of the scaling law:

$$\dot{H} = cL\nu\sigma^{\nu-1}\dot{\sigma} \tag{3.4}$$

Dividing equation 3.4 with equation 3.3, we find that the relative reduction rate of height is proportional to the relative reduction rate of density by the scaling factor ν,

$$\dot{H}/H = \nu\dot{\sigma}/\sigma \tag{3.5}$$

This simple and linear relation between relative reduction rates makes the measurement robust and insensitive to the details of the brush. For example, the pre-factor in the scaling law 3.3 disappears. It is possible the polydispersity of the polymer brush changes during the synthesis. However, the measurement on height reduction does not have any bias because of the possible differences resulting from polydispersity.

3.8 Cell Experiments

3.8.1 *Pseudomona aeruginosa* Bacteria

Seeding Bacteria

After the reinforcement treatment, the buffer in the sample holder was exchanged with LB broth. Then $5\,\mu\mathrm{L}$ of overnight-cultured *Pseudomona aeruginosa* bacteria was added on top of the brush. The sample was incubated at $37\,^{\circ}\mathrm{C}$ without shaking. $70\,\%$ of the LB broth was gently refreshed daily. $33\,\mu\mathrm{g\,mL^{-1}}$ (final concentration) of the Alexa 647 dextran was used to image the bacteria using the same microscope for the particle exclusion assay. The dextran cannot penetrate the membrane of live bacteria, thus the bacteria were inversely labeled. Effectively, we performed a 'bacteria exclusion assay'.

Washing Bacteria

The samples had the total volume of liquid removed. The sample was tilted and the M9 buffer (Sigma, M9956) was added to the top of the sample via pipette, allowed to flow to the bottom of the Teflon ring opening, extracted, and then added again to the top of the sample - this recycling wash was repeated three times. Then, this liquid was disposed of,

and another fresh M9 wash began. Overall, three fresh M9 washes were performed per sample.

3.8.2 Mouse Embryonic Fibroblasts

We used mouse embryonic fibroblast to study how cells interact with the hyaluronan brush generated by hyaluronan synthase. This cell line is a gift from Garcia Lab (GaTech) and is transfected to produce GFP-vinculin.

Following established protocol from Garcia Lab, cells were cultured in Dulbecco's Modified Eagle's Medium (DMEM) supplemented by $10\,\%$ FBS (fetal bovine serum, Corning CellGro:35-010-CV), 1% penicillin and $4\,\mathrm{mM}$ L-Glutamine. Cells were passaged at $80\,\%$ to $90\,\%$ confluency. The growth media was aspirated, and the cells were washed twice with PBS. $1\,\mathrm{mL}$ $0.05\,\%$ Trypsin is added, distributed and quickly aspirated. The culture flask is placed in the cell incubator for $60\,\mathrm{s}$ before the cells were resuspended in fresh culture media and seeded to new culture flasks or on top of hyaluronan brush.

CHAPTER 4

CHARACTERING SUPER-SIZED POLYMER BRUSH

4.1 Overview

Our super-sized (up to $10.6\,\mu\mathrm{m}$ under physiological conditions) hyaluronan brush provides a unique opportunity to be visualized using optical microscopy. In contrast, synthesized polymer brushes reported in literature seldom exceed $1\,\mu\mathrm{m}$ in thickness [67, 68, 69] and are difficult to be measured using optical microscopy. Comparing other methods typically used to characterize polymer brushes such as atomic force microscopy (AFM) [70, 71, 72, 69], ellipsometry [73]and neutron reflectometry [74, 75, 76, 77], optical microscopy has a relatively high resolution in all three spatial dimensions and super high temporal resolution. Even more powerful, single-molecule fluorescence microscopy can provide information of dynamic processes on single monomer level which is inaccessible before. In the previous work of Dr. Patrick Chang, quantitative particle assay and florescent hyaluronan-binding proteins were used to characterize the pericellular matrix whose structural backbone is made of hyaluronan. In this work, we adopted these assays and improved them for more systematic analysis.

In this chapter, first, we characterize the spatial distribution and surface coverage of the immobilized membrane fragments that contain embedded hyaluronan synthases. Second, we study how nanoparticles of different sizes and hyaluronan-binding proteins interacted with the hyaluronan brush produced by the surface immobilized hyaluronan synthase. Third, we characterized the polymer assembly after covalently linking hyaluronan to the underlying substrate. For the experiments presented in this chapter, the hyaluronan brushes were produced by hyaluronan synthases embedded in membrane fragments bound to $8\,\mu\mathrm{m}$ glass microspheres. To reduce variability, we used HAS-microspheres generated in one prepara-

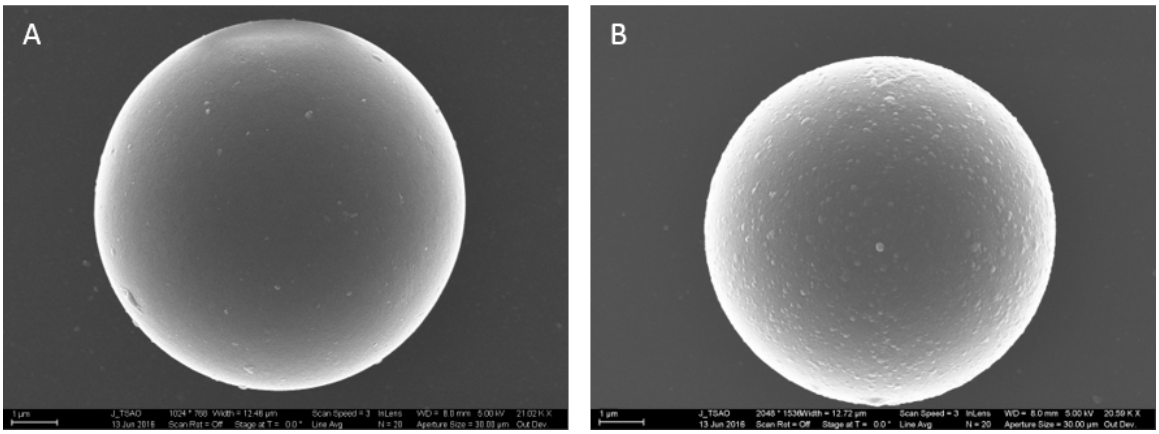

Figure 4.1: SEM image of $8\,\mu\mathrm{m}$ silica microspheres. **A** A control microsphere coated with PEI and glutaraldehyde but not membrane fragments. **B** A microsphere coated with membrane fragments. Scale bars are $1\,\mu\mathrm{m}$.

tion.

4.2 Immobilized Membrane Fragments

Scanning electron microscopy images of microspheres with and without membrane fragment treatment are presented in Figure 4.1. The comparison of the two in Figure 4.1, shows that microspheres exposed to all chemical processing except for binding the membrane fragments (Figure 4.1A) versus microspheres exposed to the membrane fragments after such treatment (Figure 4.1B) shows relatively uniform coverage of the microspheres with the fragments.

Analysis of the SEM image of planar glass surfaces prepared in the same way (it was difficult to analyze spherical surfaces) indicated that $30\,\%$ of the area was covered by membrane fragments. The size of the fragments is approximately $100\,\mathrm{nm}$ which is consistent with measurements using dynamic laser scattering (data not shown).

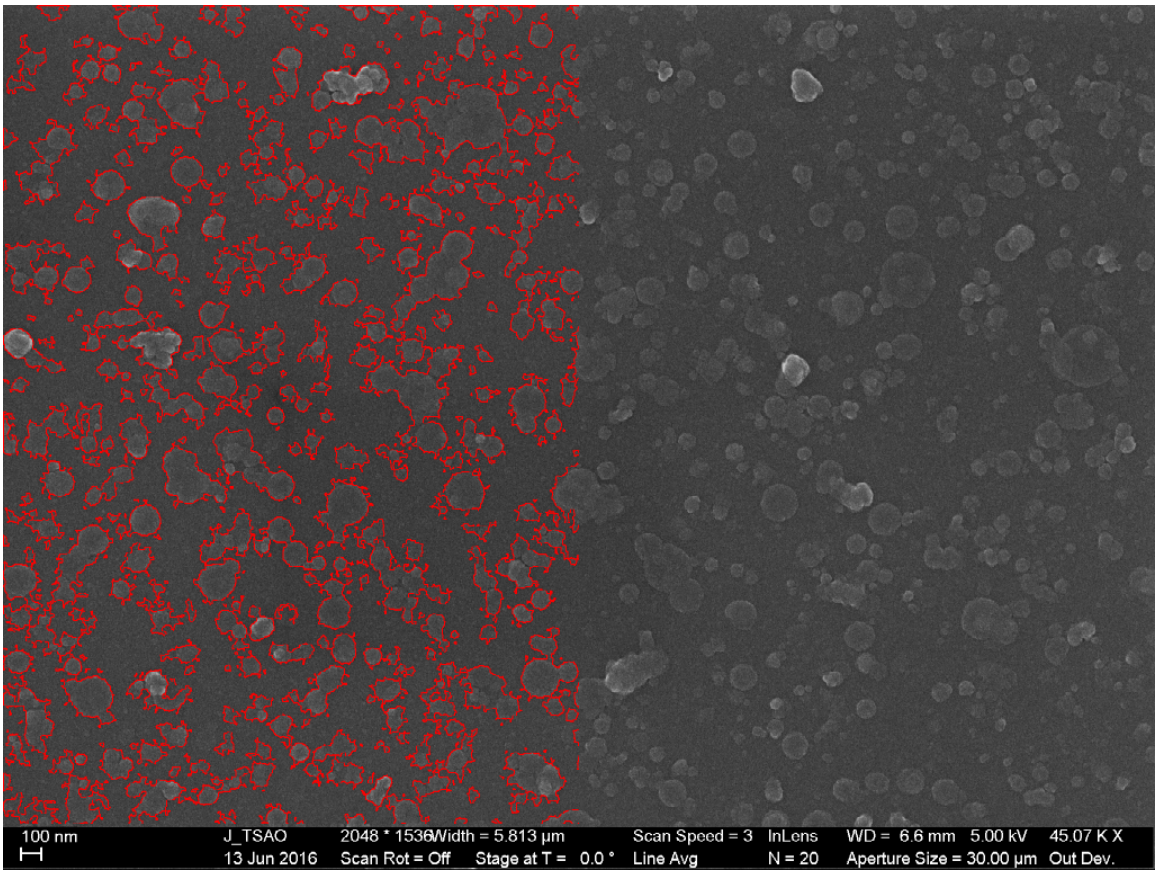

Figure 4.2: SEM image of membrane fragments on planar glass slide, taken by Dr. Joanna Tsao. The fragments cover approximately $30\,\%$ of the area. The segmentation result of the left half image is traced in red. Scale bar is $100\,\mathrm{nm}$.

4.3 Quantitative Particle Exclusion Assay

The traditional particle exclusion assay uses red blood cells to probe the edge of the pericellular matrix. However, the irregular shape of the erythrocytes hampers the accuracy of the assay. The relatively large size of the erythrocytes also limits characterization of the internal structure of the brush. In the previous work of Dr. Patrick Chang of the Curtis lab ([54, 55]), a complementary assay, referred as the quantitative particle exclusion assay, was developed where the erythrocytes were replaced with nanoparticles of well-defined sizes to probe the accessibility of the pericellular matrix. In this work, we used this assay to study the physical structure of the hyaluronan brush. When relatively large particles were used, particles were excluded from the brush, and the assay resembles the traditional assay using erythrocytes. Particles of intermediate sizes partially penetrated into the brush and established a density gradient. In the limit of small size particles, the brush hardly blocked the particles. $10\,\mathrm{kDa}$ anionic dextran efficiently penetrated the brush and was used to trace the surface of the microsphere.

4.3.1 Particle Penetration Profile

In the previous work of Dr. Patrick Chang of the Curtis lab ([54, 55]), it has been shown the pericellular matrix acts as a sieve for particles of different sizes. We expect similar phenomena in the hyaluronan brush. de Vos *et al.* performed a self-consistent-field analysis on the interaction of particles with a polydisperse uncharged brush. However, future work is needed to match parameters in the theoretical analysis and experimental parameters of our hyaluronan brush before a quantitative comparison can be made.

Hyaluronan synthases were activated for $4\,\mathrm{h}$ to allow polymer growth. Figure 4.3 shows the results of quantitative particle exclusion assay for different particle sizes. It is clear that the dextran and nanoparticles of different sizes have distinct penetration profiles.

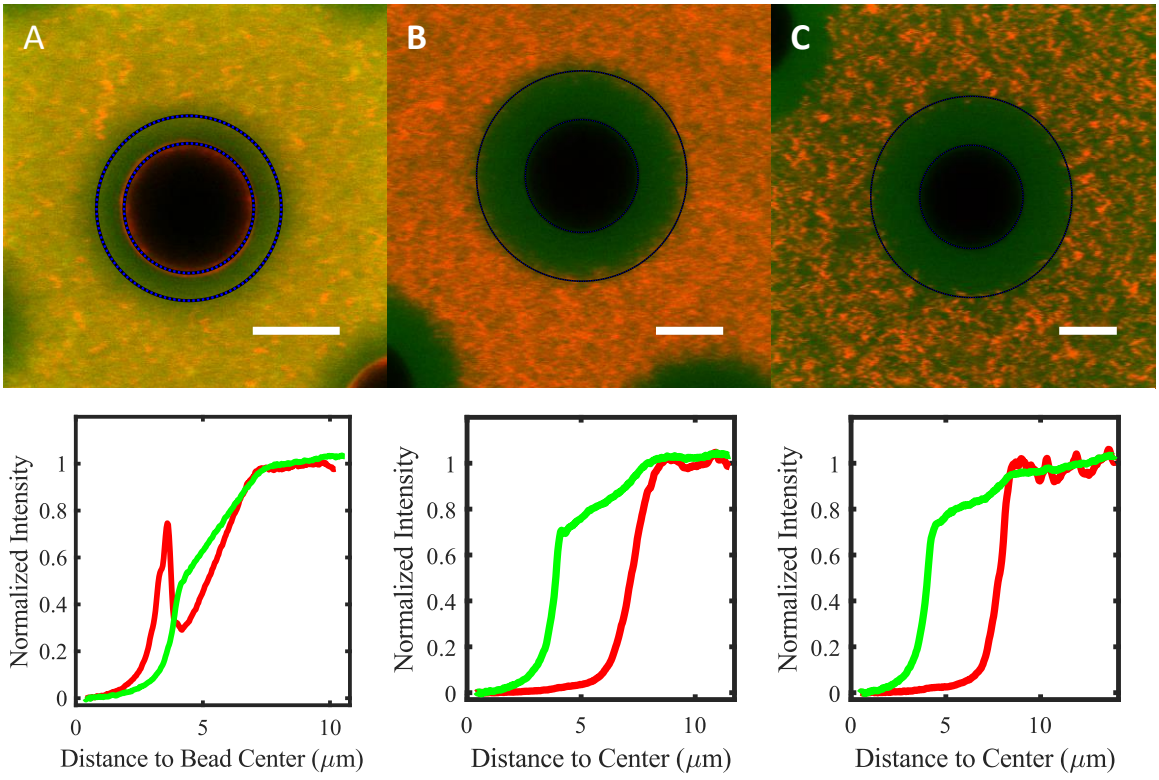

Figure 4.3: Fluorescence images of nanoparticles and 10 kDa Dextran. The corresponding intensity profiles are plotted below each image. Nanoparticle sizes: **A** 20 nm; **B** 100 nm; **C** 200 nm. Scale bars are 5 µm.

$20\,\mathrm{nm}$ *Nanoparticles*

At $3.68(53)\,\mu\mathrm{m}$ (N = 59) away from the grafting surface, nanoparticles started to be partially excluded by the brush. At $1.81(43)\,\mu\mathrm{m}$, their density dropped to $50\,\%$ as of the density in the non-brush region. Their density right next to the surface is about $30\,\%$ as of the density in the non-brush region. A small portion of the nanoparticles adhered to the surface of the microsphere and formed a peak in the intensity profile.

$100\,\mathrm{nm}$ *and* $200\,\mathrm{nm}$ *Nanoparticles*

$100\,\mathrm{nm}$ and $200\,\mathrm{nm}$ nanoparticles could not reach the grafting surface and had much steeper intensity gradient near the edge of the brush. For $100\,\mathrm{nm}$ nanoparticles, they started to be excluded at $4.22(23)\,\mu\mathrm{m}$ (N = 52) away from the grafting surface and their density dropped to $50\,\%$ at $3.41(20)\,\mu\mathrm{m}$. For $200\,\mathrm{nm}$ nanoparticles, they started to be excluded at $4.55(30)\,\mu\mathrm{m}$ (N = 148) and their density dropped to $50\,\%$ at $3.75(30)\,\mu\mathrm{m}$. The exclusion thickness of $200\,\mathrm{nm}$ nanoparticles was only about $300\,\mathrm{nm}$ larger than the exclusion thickness of $100\,\mathrm{nm}$. This weak increase suggested the exclusion thickness measured with both particle sizes was a good estimation of the brush thickness.

$10\,\mathrm{kDa}$ *dextran*

With the present of $20\,\mathrm{nm}$ nanoparticles, the density of dextran at the grafting surface is about $50\,\%$ as of the density in the non-brush region. In contrast, about $70\,\%$ dextran reached the grafting surface. This difference in dextran profiles was not an optical artifact that the emission light from nanoparticles leaked into the dextran channel because the dextran profile did show a peak at the grafting surface where $20\,\mathrm{nm}$ aggregated. Thus, the reduced density of the dextran at the grafting surface in the $20\,\mathrm{nm}$ assay, compared with the $100\,\mathrm{nm}$ and the $200\,\mathrm{nm}$ assay, was caused by volumetric and electrostatic repulsion of the $20\,\mathrm{nm}$ particles which were coated with carboxyl groups and partially penetrated the brush. Thus, the density profile of the $20\,\mathrm{nm}$ was hardly influenced by the dextran because

the mass concentration of the $20\,\mathrm{nm}$ particles was 211 times higher than that of the dextran.

4.3.2 Polymer Brush Thickness

The thickness of a brush is the difference between the radius of the particle exclusion region and the radius of the grafting microsphere (Section 3.5.2). While we developed an accurate method to measure the radius of each microsphere, determining the radius of the exclusion zone was more complicated because there was no sharp transition from the exclusion region and the non-brush region in the intensity profile of nanoparticles. If we adopt the method in a Rubinstein's work [56], we need to linearly extrapolate the transition part of the profile to zero intensity where the edge is defined. However, this method underestimates the exclusion radius and reports a negative brush thickness on a bare microsphere. In Dr. Patrick Chang's work, the edge of the exclusion region was manually selected where the intensity was close to the non-pericellular-matrix region. This method suffered from fluctuations in the concentration of nanoparticles. In this work, we define the edge of the exclusion region as the position where the intensity is $50\,\%$ of the intensity in the non-brush region.[1] This is a natural extension of the method to process a microscopy image of a sharp step function. The image is the convolution of a Gaussian kernel whose width is determined by the microscope with a step function. The position of the edge is where the intensity is $50\,\%$ of the higher value of the step function.

4.4 Brush Interactions with Proteins

4.4.1 GFPn

The molecular weight of GFP is $27\,\mathrm{kDa}$ and the G1 domain of neuroncan is $37\,\mathrm{kDa}$. Assuming the shape of the GPFn is globular and scaling from the molecular weight and size of BSA, we estimated the size of GPFn is $7\,\mathrm{nm}$ to $10\,\mathrm{nm}$. Based on the penetration profiles

[1] See Figure 3.2 for how the non-brush region was selected.

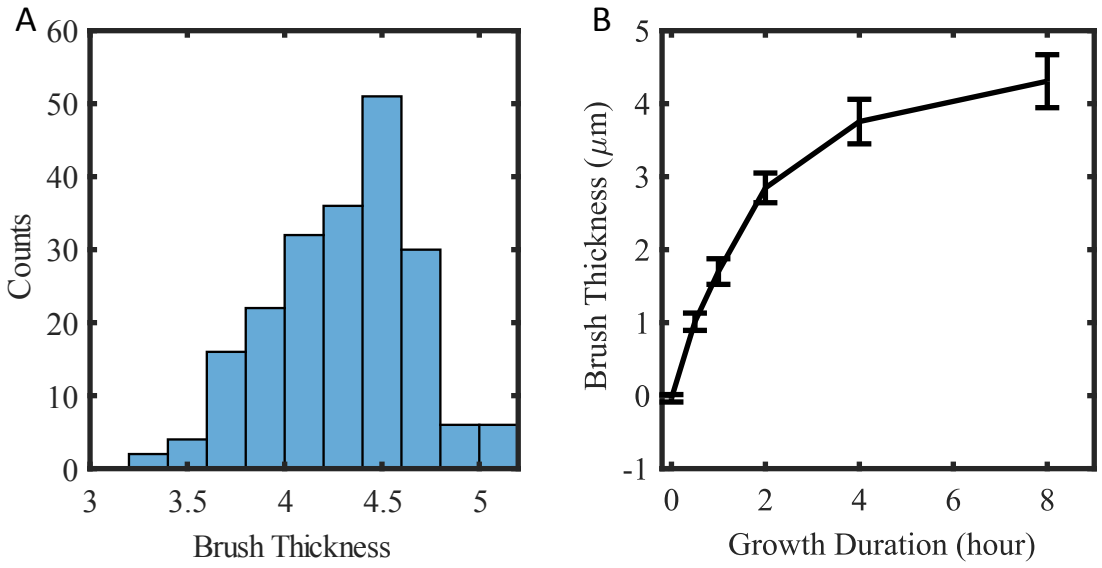

Figure 4.4: Thickness of spherical hyaluronan brush. **A** Histogram of brush thicknesses measured from $8\,\mu\mathrm{m}$ mcirospheres with $8\,\mathrm{h}$ hyaluronan grown. **B** Brush thickness over growth duration. Error bar is standard deviation ($\mathrm{N} > 120$).

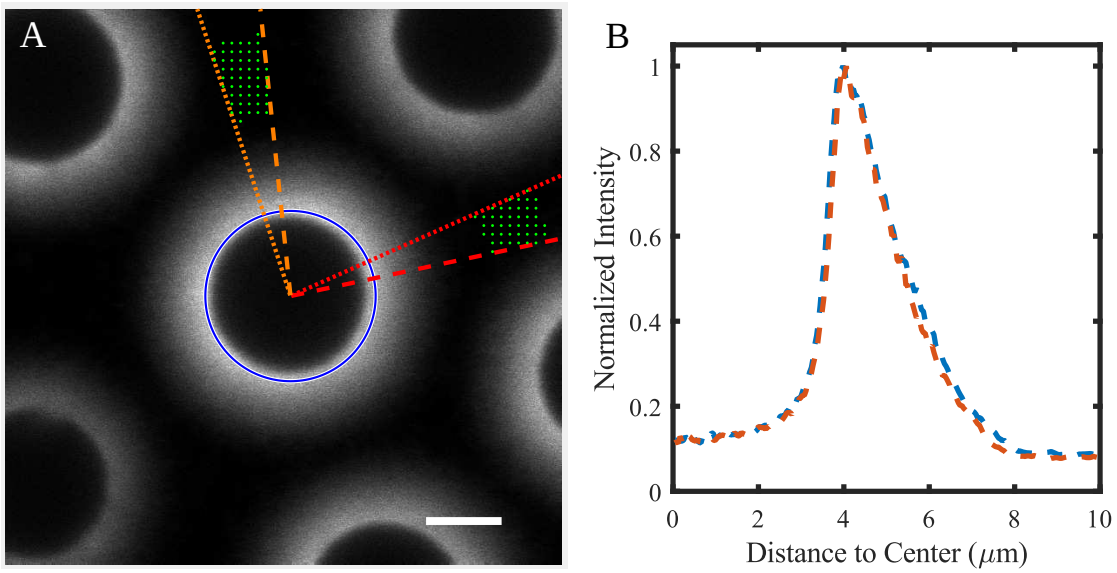

Figure 4.5: **A** Hyaluronan brushes on microspheres fluorescently labeled with GPFn. **B** Radially averaged fluorescence intensity profiles from two conical regions in **A** are similar(blue, red). During the washing step to remove DTT, the microspheres were flushed together, and most data analysis was on microspheres with neighbor microspheres. Scale bar is $5\,\mu\mathrm{m}$.

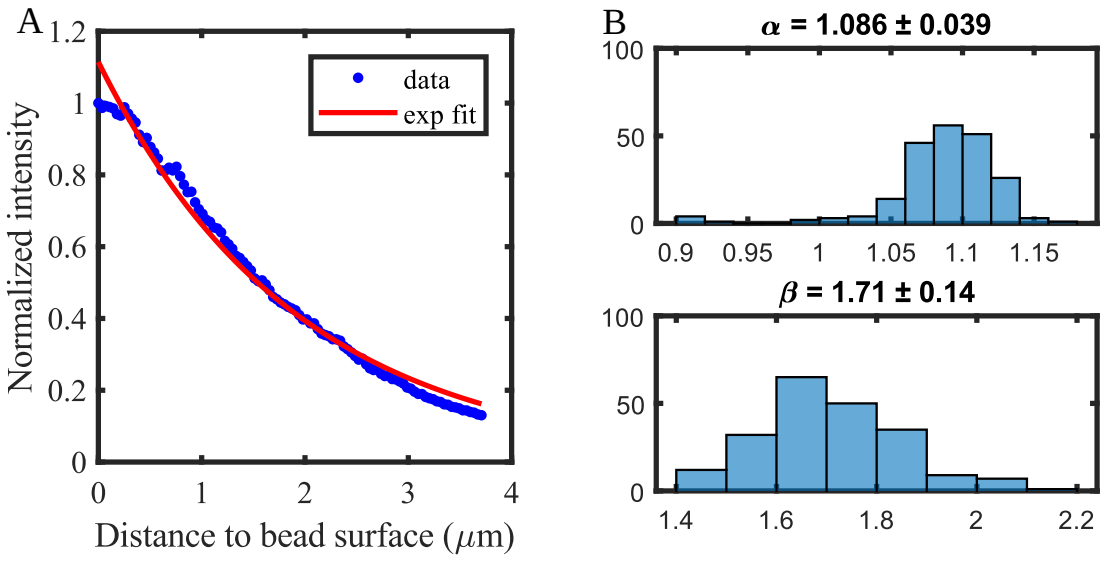

Figure 4.6: Fitting $\alpha \exp(-x/\beta)$ to the GFPn intensity profiles. **A** A single profile (data and exponential fit). **B** Histograms of the fitted parameters on 211 profiles from 112 microspheres.

of $10\,\mathrm{kDa}$ ($4.1\,\mathrm{nm}$) dextran and $20\,\mathrm{nm}$ nanoparticles, GPFn was able to penetrate the brush, and its binding energy should overcome the exclusion barrier inside the brush. Thus, we concluded the intensity profile of GPFn was a good approximation of the mass profile of the hyaluronan brush. The thickness of the brush which was under 4 hours of growth was $3.70(25)\,\mu\mathrm{m}$. We need to point out that during the washing step, the flushing aggregated the microspheres and all the brushes analyzed had a few neighboring brushes which may interfere the profiles. It is known that the polymer brush has very low surface friction [78]. If there were significant pressure between neighboring microspheres, the pressure would push the microsphere away, and thus the pressure would be released. This is supported by the fact that the brush-bearing microspheres were uniformly spaced.

After we normalized the GFPn intensity profiles by the intensity at the grafting surface, the profiles can be well approximated by exponential curves $\alpha \exp(-\mathrm{x}/\beta)$. The fitting results are plotted in Figure 4.6. β in the fitting results is about half of the brush thickness. The convex shape of the profile is consistent with the calculated density profile of a brush made

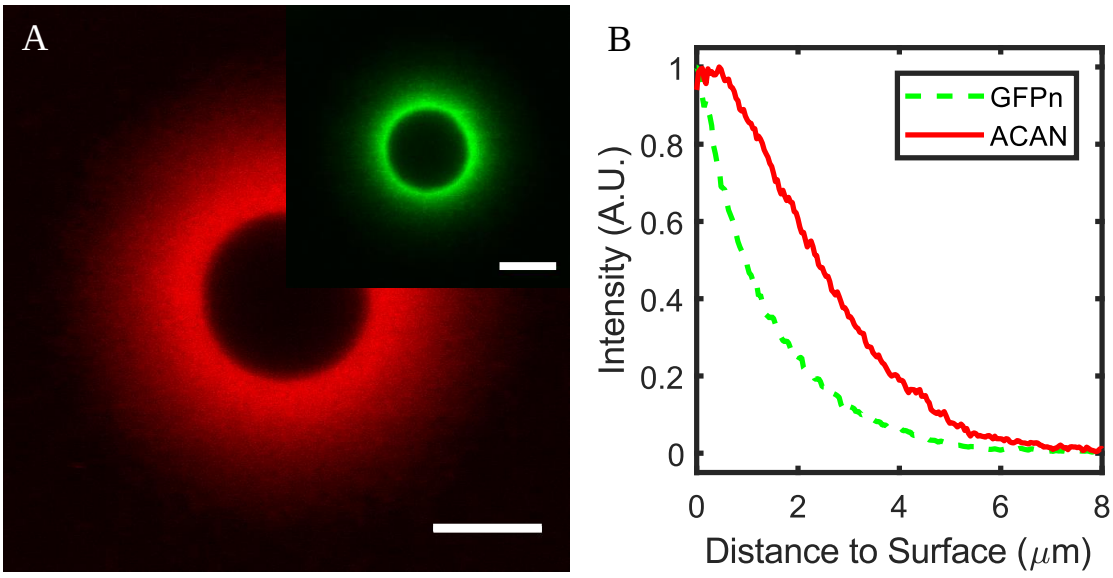

Figure 4.7: Fluorescent aggrecan bound to hyaluronan brush. **A** Fluorescence image. Inset: A GFPn image of the same brush. **B** Radially averaged intensity profiles for aggrecan and GFPn. Scale bars are $5\,\mu\mathrm{m}$.

of polydisperse polymers using self consistent field analysis [42].

4.4.2 Aggrecan Binding to Hyaluronan Brush

Comparing with GPFn, aggrecan is a much larger molecule. Aggrecan exhibits a bottle brush structure where glycosaminoglycan chains are attached to a long core protein. Bovine aggrecan is approximately $100\,\mathrm{nm}$ wide and $500\,\mathrm{nm}$ long [79]. We had seen that $100\,\mathrm{nm}$ nanoparticles did not penetrate the brush and we speculated that aggrecan, with a similar size, should be only able to bind the edge of the brush because of steric exclusion. However, as shown in Figure 4.7, aggrecan molecules do penetrate the brush, bind throughout the brush and reach the grafting surface. We hypothesize that this can be explained by the semi-flexible structure of the aggrecan [80]. Unlike the hard and solid latex nanoparticles, aggrecan is flexible and has internal spaces. Aggrecan is made of a protein backbone and sugar sidechains along the backbone. The protein backbone is flexible. The sugar sidechains are flexible, and there is space between the sugar sidechains. Because of this

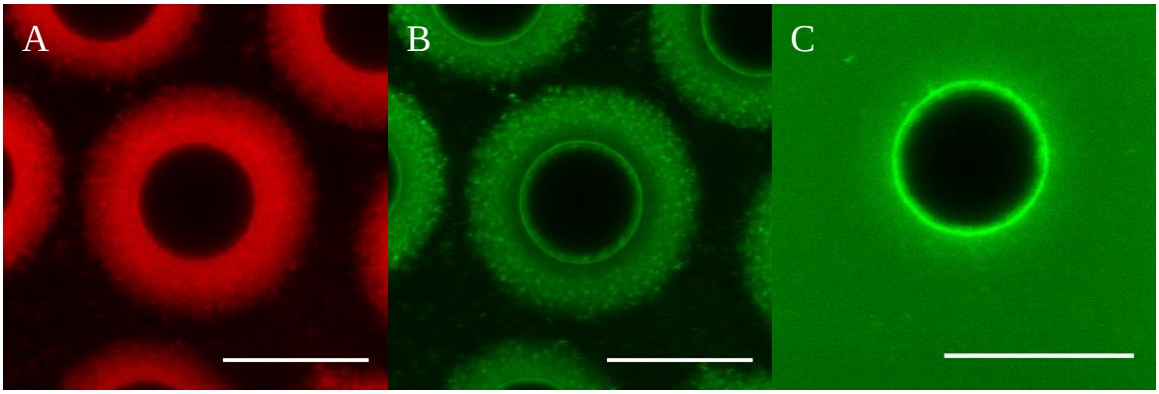

Figure 4.8: Negatively charged aggrecan sequesters positively charged histone proteins. **A** Fluorescence image of aggrecan (with histone present) in hyaluronan brush. **B** Fluorescence image of histone of the same microsphere in **A**. The solution with proteins was partially exchanged with protein-free buffer. **C** Histone and hyaluronan brush without aggrecan. The solution was not exchanged after the addition of histone. Scale bars are $10\,\mu\mathrm{m}$.

flexible and dynamic structure, aggrecan was able to penetrate the flexible and dynamic hyaluronan brush. Aggrecan partially swelled the brush and thickness after $4\,\mathrm{h}$ of synthesis measured from the aggrecan image was $4.86(63)\,\mu\mathrm{m}$ (N = 48) comparing with the thickness $3.70(25)\,\mu\mathrm{m}$ measured before aggrecan was added to the sample.

The intensity profile of aggrecan, compared with the GFPn profile (taken with aggrecan present), indicates that volume close to the grafting surface was saturated with aggrecan. As we were scanning from the edge of the brush to the grafting surface, the intensity of GFPn kept increasing which indicated the density of hyaluronan increased. However, the intensity of aggrecan plateaued near the grafting surface. Although there were more hyaluronan monomers and binding sites, we hypothesize that there was not enough space to fit more aggrecan.

4.4.3 Histone

The sidechains of aggrecan are negatively charged. Because aggrecan carries many sidechains, aggrecan is a highly negatively charged molecule. Chang showed in his work that the

pericellular matrix absorbed positively charged molecule such as histone. This suggested cell may take advantage of the negatively charged to efficiently collect some important molecules from the environment such as the positively charged growth factor. However, we did not know whether histone molecules were absorbed by the hyaluronan or the aggrecan because they both carry negative charges and present in the pericellular matrix. The hyaluronan brush provided a unique opportunity because it is free of intrinsic aggrecan.

In the case without aggrecan, there was much less difference in the intensity of histone in the brush region and the non-brush region (Figure 4.8C). However, when aggrecan and histone were added, a significant amount of histone aggregated onto the brush(Figure 4.8 B). Moreover, they formed visible and granular clusters. Comparing the results, we found it was the aggrecan that absorbed the histone. A similar phenomenon has been observed when multivalent ions were added to polyelectrolyte brushes [81, 82, 83].

For the experiments above, we see the potential for this model system to analyze complex interactions of various players in the glycocalyx and to test long-standing hypotheses about the sequestration of growth factors in pericellular matrix.

4.4.4 GFPn and Nanoparticles Aggregated around HA Brush

The thickness of the brush measured using $200\,\mathrm{nm}$ PEA $3.75(30)\,\mu\mathrm{m}$ is consistent with the value measured using GPFn $3.70(25)\,\mu\mathrm{m}$. These values were collected from separate experiments using PEA and GFPn. We wanted to simultaneously measure GFPn and excluded particles on the same hyaluronan brush. GFPn was first added to the sample. $30\,\mathrm{min}$ later, we added $200\,\mathrm{nm}$ nanoparticles. Nanoparticles non-specifically bound to the GFPn proteins which were attached to brush. As shown in Figure 4.9, some nanoparticles formed a shell around the brush, and the thickness of the brush was reduced. In the top left corner of the image, we observed bridges made of hyaluronan, GFPn, and nanoparticles between some microspheres. The brush greatly reduced the diffusion of the nanoparticles and made it possible to capture in the middle of the diffusion process.

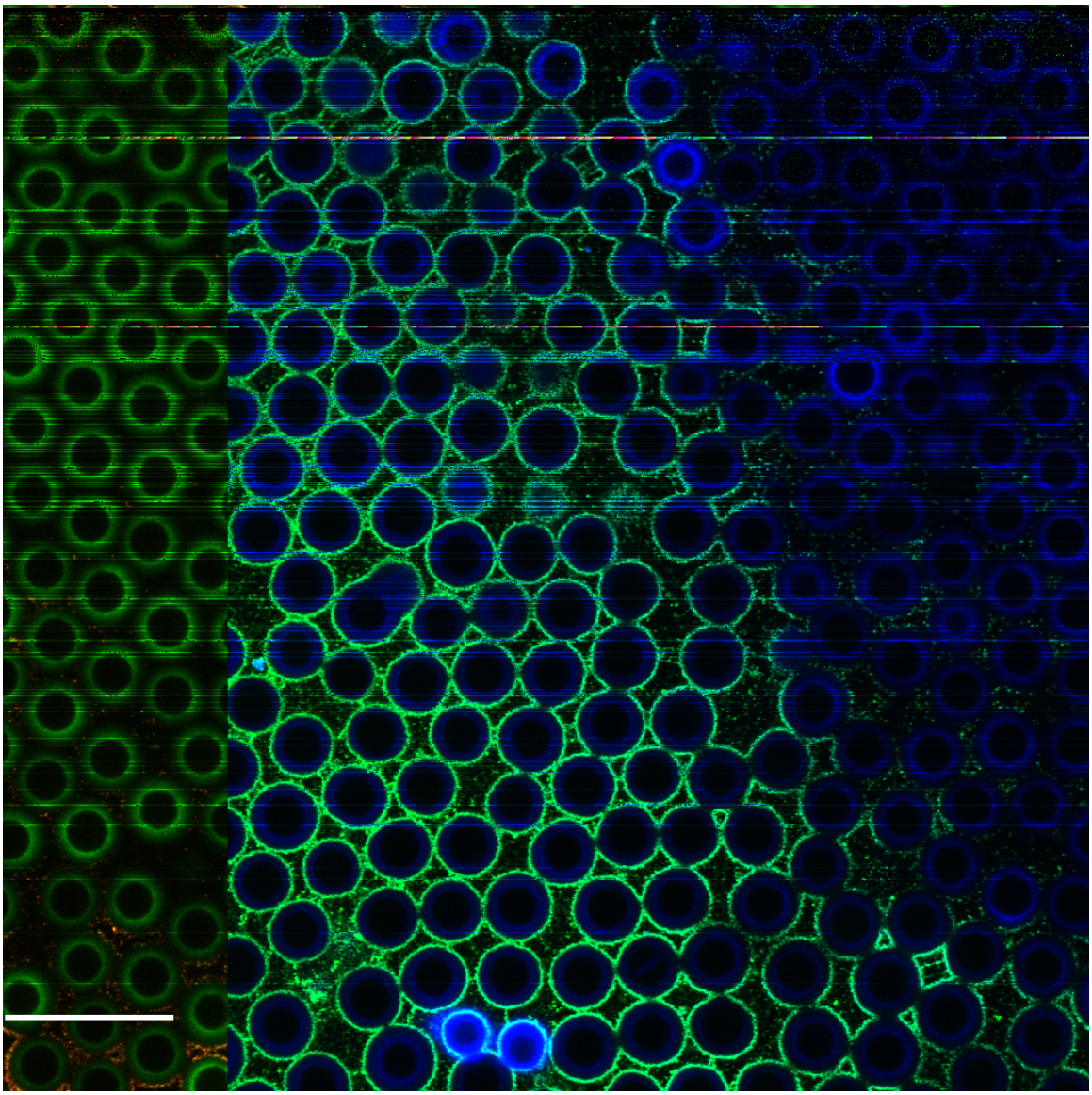

Figure 4.9: Hyaluronan brush had been labeled with GFPn before $200\,\mathrm{nm}$ nanoparticles were added to the sample. The image was taken in a region packed with microspheres carrying brushes. Nanoparticles were diffusing into the region from the left of the field of view. Scale bar is $50\,\mu\mathrm{m}$. The contrast of the image was adjusted using Fiji [84].

4.4.5 Polymer Entanglement in the Brush Is Weak

In this section, we tested if the hyaluronan polymers are entangled and can hold the structure without the grafting on the hyaluronan synthases. We used a detergent to break the grafting between hyaluronan and hyaluronan synthase. Sodium dodecyl sulfate (SDS) is a denaturing detergent which disrupts lipid membranes and denatures proteins by breaking protein-protein interactions. SDS breaks the grafting of hyaluronan by disrupting the membrane fragments and denaturing hyaluronan synthases in the membrane. The dynamic process of hyaluronan detaching from the grafting glass beads is shown in Figure 4.10. This is one of the earlier experiments where we used low-quality polydisperse glass beads and the protocol for coating hyaluronan synthases on glass surfaces was not well established. The synthesis duration was $3\,\mathrm{h}$. The timing labeled in the figures was started about $30\,\mathrm{s}$ after $10\,\mathrm{mg\,mL^{-1}}$ (final concentration) of SDS was gently added into the sample. At $8\,\mathrm{s}$, a significant portion of hyaluronan started to detaching the glass beads, and the exclusion region of nanoparticles swelled. Osmotic pressure increases the local concentration of the nanoparticles at the edge of the polymer region. At $12\,\mathrm{s}$, hyaluronan and nanoparticles started to mix, and the boundary of the exclusion region of nanoparticles started to blur. At $2\,\mathrm{min}$, hyaluronan brush was destroyed. Variation in the density of nanoparticles suggests the unevenness of the concentration of hyaluronan. This experiment suggests that the entanglement between hyaluronan polymers in the brush is low and insufficient to constraint the polymers after the grafting to hyaluronan synthases was destroyed.

4.4.6 Hyaluronan Responding to Low Ionic Strength

The carboxyl groups on hyaluronan polymers partially dissociate and release hydrogen ions. This causes hyaluronan to become negatively charged under neutral and basic pH. In the measured above, we used a relatively high ionic strength ($100\,\mathrm{mM}$), and charges on hyaluronan were mostly shielded by the counterions. However, at lower salt concentration, the apparent charge of carboxyl groups is larger. The increase in the electrostatic repulsion

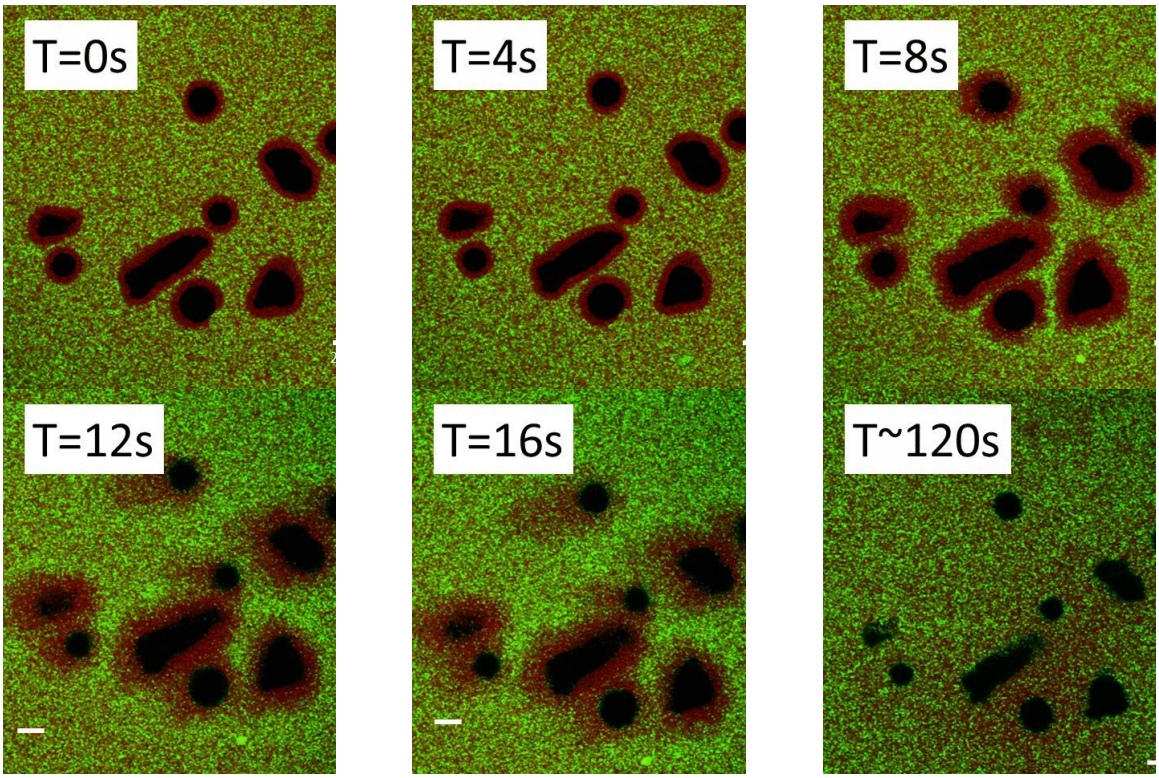

Figure 4.10: Desorption of hyaluronan after SDS destroyed the membrane fragments. 200 nm nanoparticles and dextran were added to facilitate the visualization of the process. After SDS, the region filled with HA, as labeled by exclusion region of nanoparticles expands; at t=12s, the nanoparticles begin to penetrate as the freed hyaluronan continues to diffuse. By t=120 s the polymer, dextran and nanoparticles are well mixed. Scale bars are 2 µm.

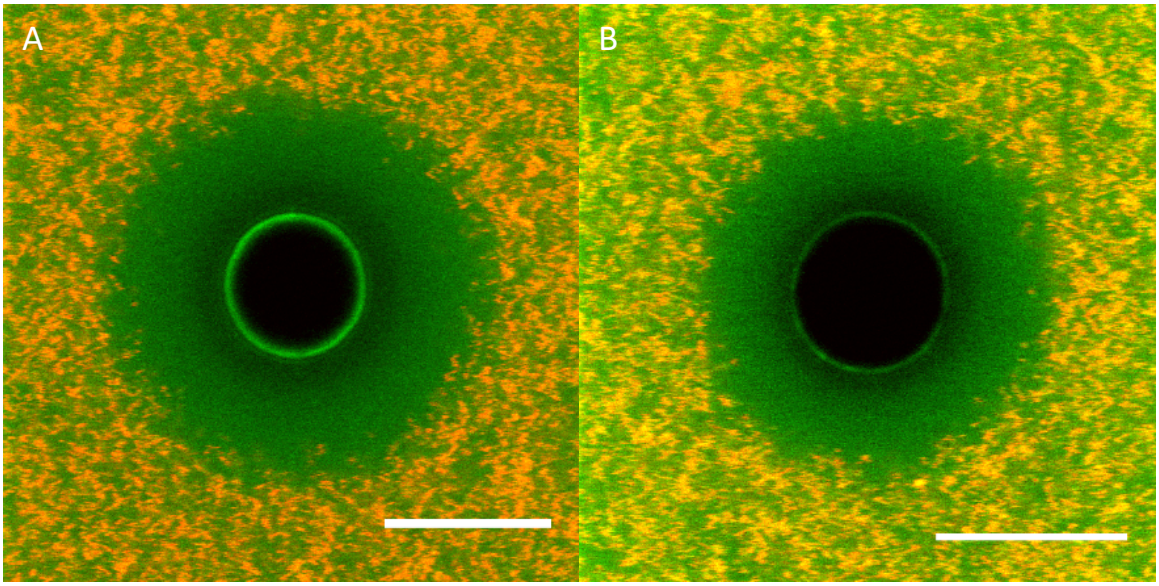

Figure 4.11: Particle exclusion assay at low ionic strength. **A** Hyaluronan brush without the reinforcement treatment. **B** Hyaluronan assembly after the reinforcement treatment. Sclar bars are $10\,\mu\mathrm{m}$.

inside and between hyaluronan polymers further stretches the polymers and increases the brush thickness. In work by Attili [69], it has been shown that the thickness of hyaluronan brush is remarkably close to the contour length of the polymers under very low salt concentration ($\leq 0.5\,\mathrm{mM}$).

After lowering the buffer concentration to $1\,\%$ of the normal concentration, we observed a significant increase in the thickness of hyaluronan brush ($4\,\mathrm{h}$ synthesis duration). The super-sized structures visualized by particle exclusion assay are shown in Figure 4.11. The thickness increased from $3.75(30)\,\mu\mathrm{m}$ to $7.64(42)\,\mu\mathrm{m}$ (N = 68). In work by Dr. Weigel, where the same hyaluronan synthase was used, the steady-state molecular weight of the hyaluronan product was $3.78\,\mathrm{MDa}$ which corresponded to a contour length of $9.45\,\mu\mathrm{m}$. For the hyaluronan assembly after a reinforcement treatment which is described in the next section, the thickness increased from $2.82(30)\,\mu\mathrm{m}$ (N = 151) to $5.15(46)\,\mu\mathrm{m}$ (N = 32).

4.5 Covalently Grafted Hyaluronan Assembly

Our hyaluronan brush has a limited lifetime. Refer to chapter desorption. Within $7\,\mathrm{h}$, $50\,\%$ hyaluronan polymers detach from the hyaluronan synthase proteins from *Streptococcus equisimilis*. This is because the binding between the polymer and the protein is noncovalent. To increase the lifetime of the hyaluronan brush, we developed a procedure where the grafting of hyaluronan on the underlying surface was reinforced. We used EDC chemistry to form covalent bonds between the carboxyl groups on the hyaluronan with the amine groups on the surface.

Every disaccharide residue of hyaluronan has a carboxyl group, and each carboxyl group has the potential to be crosslinked with an amine group on the surface. However, according to polymer physics, only the disaccharide residues close to the surface have dominating probability to reach the surface. Thus the covalent grafting will take place close to the tail of the polymer, and the structure of the treated polymer assembly should resemble an end-grafted polymer brush. In this section, we characterized the reinforced hyaluronan assembly using the same tool for the native hyaluronan brush. The hyaluronan assembly has similar physical and chemical structure as the native brush but has much stronger stability. However, carboxyl groups in the hyaluronan, after activated with EDC, can form bonds to the -OH groups to itself or neighboring hyaluronan polymers. Further characterization using such as infrared spectroscopy and nuclear magnetic resonance is needed to exam the chemical component of the reinforced polymer assembly.

4.5.1 Particle Exclusion Assay

Qualitatively, the PEA profiles (Figure 4.12) of the reinforced hyaluronan assembly was similar with the untreated hyaluronan brush. However, the thickness was significantly reduced after the reinforcement. The comparison of thickness before and after the reinforcement is shown in Figure 4.13. According to the results below, we did not observe

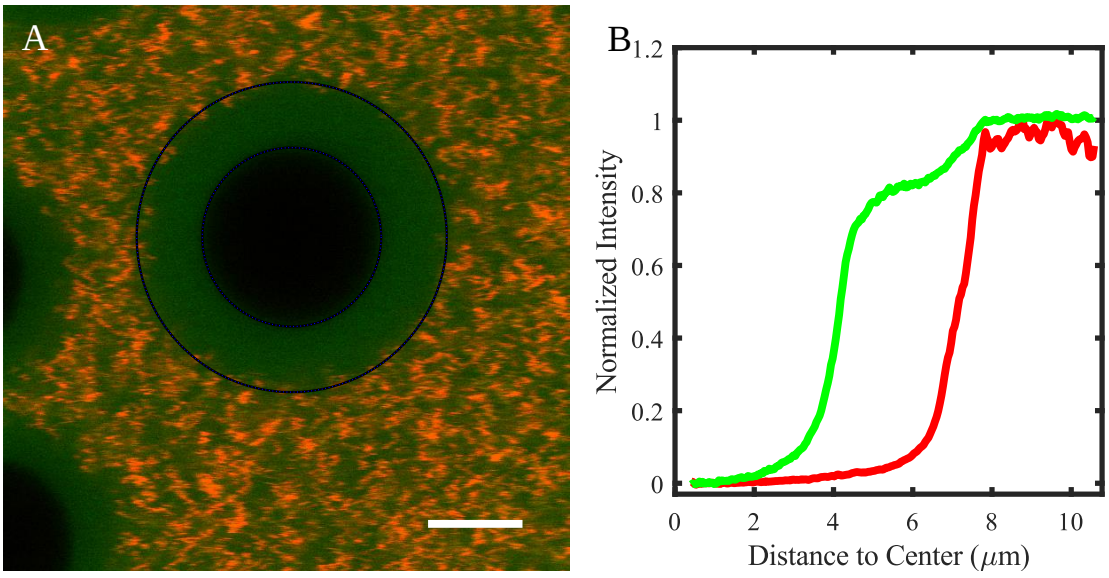

Figure 4.12: Particle exclusion assay using $200\,\mathrm{nm}$ nanoparticles and $10\,\mathrm{kDa}$ dextran on reinforced brush ($4\,\mathrm{h}$ growth). Scale bar is $5\,\mu\mathrm{m}$.

a significant change in the physical structure of the polymer assembly. The major reason for the thickness reduction is that a portion of the hyaluronan polymers detached before they formed covalent bonds with the grafting surface. In Figure 4.13 B, we estimated the portion of remaining hyaluronan according to the scaling law $\mathrm{H} \propto \mathrm{L}\sigma^{1/3}$ (see Section 2.6). The reinforced grafting efficiency was higher for the brush of shorter polymers. A potential explanation is that longer polymers desorb faster than shorter polymers. Another potential explanation is that the thicker brush reduces the amount of EDC and sulfo-NHS chemicals to the grafting surface and reduces the probability of forming covalent bonds. More research is needed to understand the reinforcement process.

4.5.2 GFPn Profile

The profiles of GFPn (Figure 4.14) bounded to the reinforced polymer assembly were similar to the untreated polymer brush. The profiles can also well approximated by an exponential function $\alpha \exp(-\mathrm{x}/\beta)$ (Figure 4.14). The fitted β parameter was also about half of the thickness of the assembly. This suggests that the physical structure of the polymer

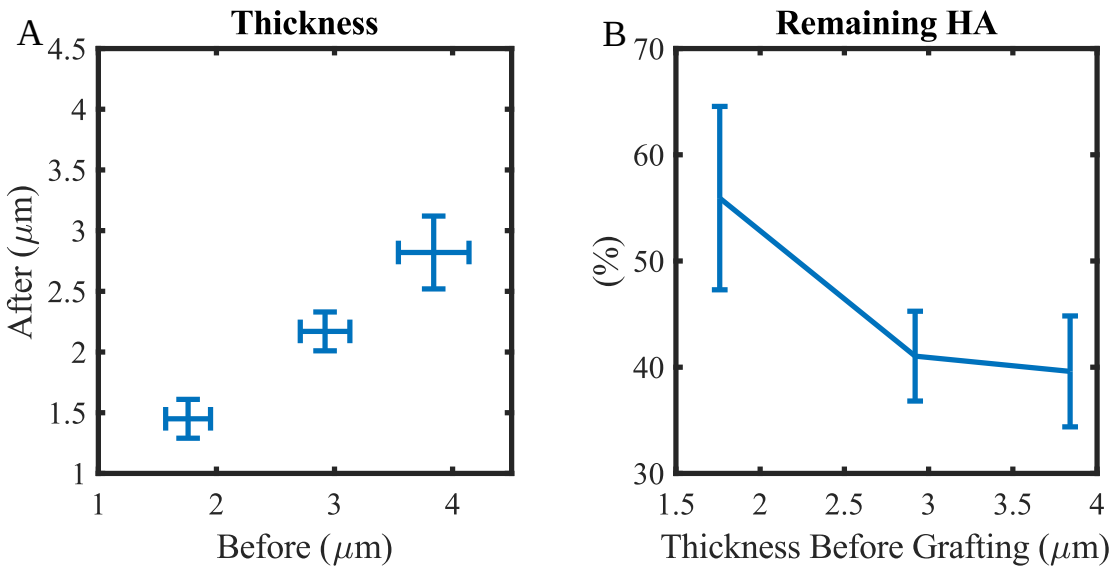

Figure 4.13: Comparing the amount of hyaluronan before and after the reinforcement treatment. **A** Thickness of brush. **B** Estimated normalized grafting density using scaling law for polymer brush. $N_1 = 74, N_2 = 42, N_4 = 151$

assembly is similar to the untreated polymer brush. However further characterization, such as force spectroscopy, is required to understand the structure of the reinforced assembly.

4.5.3 Hyaluronidase

Similar to the untreated hyaluronan brush, the reinforced hyaluronan assembly can be disrupted by hyaluronidase. This suggests the chemical structure of hyaluronan was protected in the reinforcement procedure.

4.5.4 Detergent Resistance

Detergent SDS destroyed the untreated hyaluronan brush within 2 minutes. But the reinforced hyaluronan assembly stayed intact upon SDS (Figure). This confirms the formation of covalent bond between hyaluronan polymers and the grafting surface.

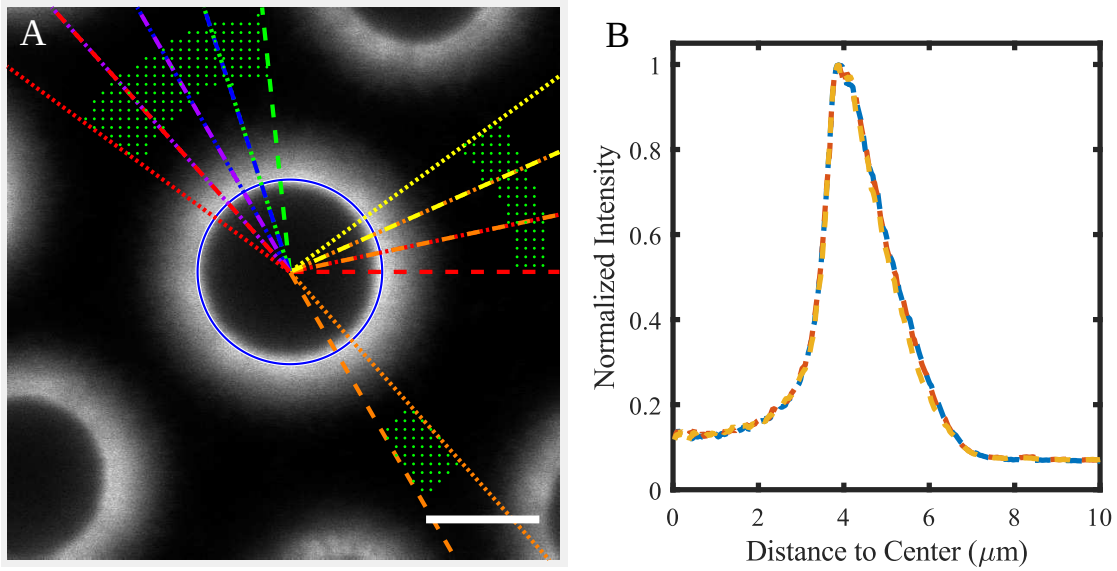

Figure 4.14: Reinforced hyaluronan assembly labeled by GPFn. **A** Fluorescence image.**B** Radially averaged intensity profiles in the eight conical regions in **A**. Scale bar is $5\,\mu\mathrm{m}$.

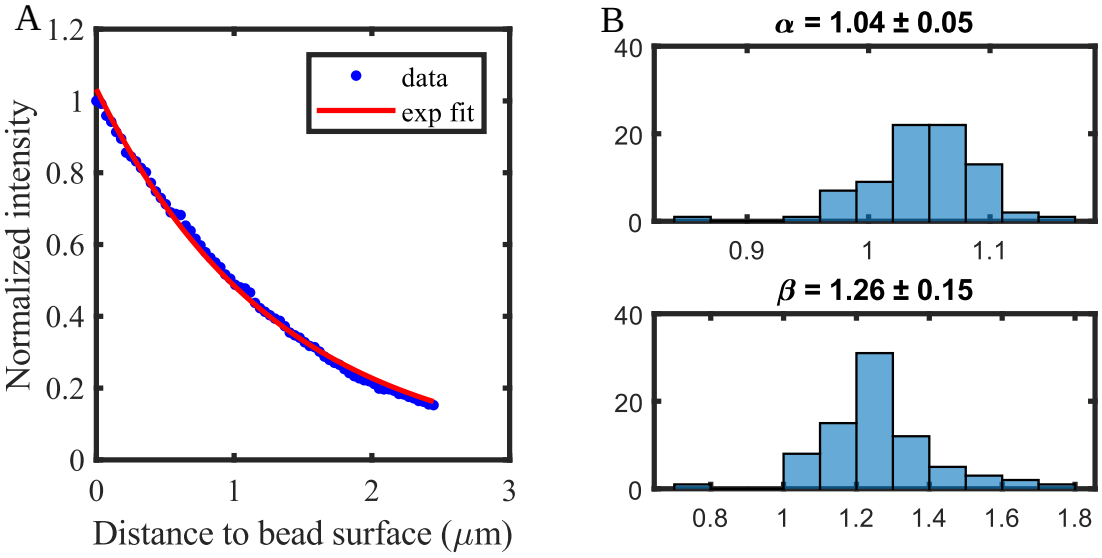

Figure 4.15: Fitting $\alpha \exp(-x/\beta)$ to the GFPn intensity profiles. **A** A single profile. **B** Histograms of the fitted parameters on 81 profiles from 78 microspheres.

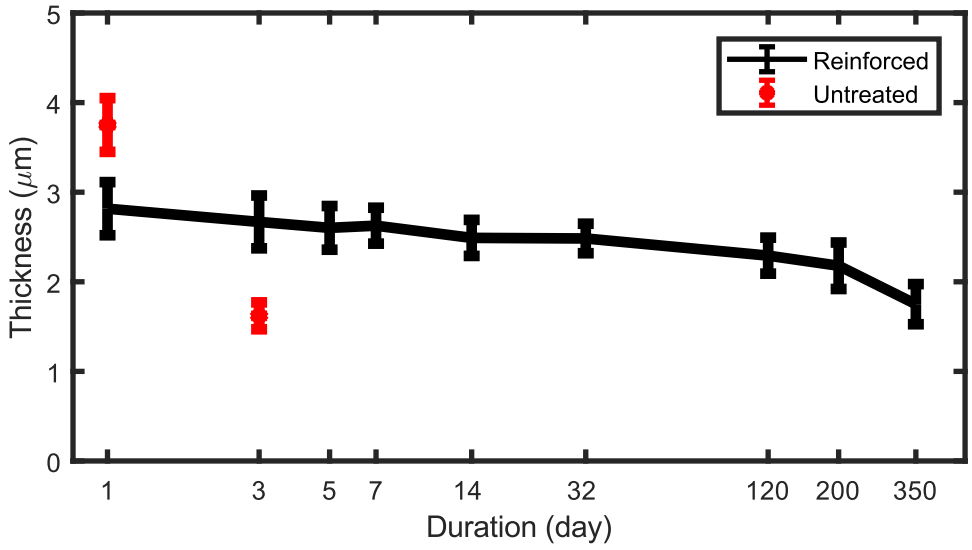

Figure 4.16: Thickness of the reinforced hyaluronan assembly over a period of 350 days. In comparison, the thickness of the untreated brush dropped significantly in three days. $\mathrm{N} > 30$.

4.5.5 Longterm Stability of Hyaluronan Brushes

The reinforcement procedure greatly extended the stability of the hyaluronan assembly. After reinforcement, the thickness after 350 days of storage under room temperature was higher than the thickness of an untreated sample after three days under the same condition (Figure 4.16). On a timescale of months, thermal degradation of hyaluronan polymer is significant [85] which partially explains the reduction in the thickness.

4.6 Summary

In this chapter, we characterized the physical structure of the hyaluronan brush produced by surface-coated hyaluronan synthases. Due to its micrometer thickness, we were able to visualize the brush using a scanning laser confocal microscope. To our knowledge, this is the first work to systematic study polymer brush purely made of hyaluronan using optical microscopy. Interactions with nanoparticles and proteins provided the physical structure of the brush. The pore size of the brush is about $20\,\mathrm{nm}$ and the brush has a vertical density

profile which can be approximated by an exponential decay. We used EDC chemistry to reinforce the grafting between the polymers and the surface. The reinforced product has a similar structure as the untreated brush but much improved stability.

CHAPTER 5
PROBING THE MECHANISM OF HYALURONAN LENGTH REGULATION

5.1 Overview

As physicists, only when we build a mathematical model which predicts the length distribution of hyaluronan in the brush and released into the solution, can we state that we understand the mechanism of hyaluronan length regulation. In this chapter, we first introduce a generic model for the length regulation mechanism. Its instantiations[1] are specific models which can be tested against experimental results. Then, starting from the simplest model, we use results from the literature and our experiments to instantiate and adjust the model. According to our results, we reduced the pool of possible candidates to a set of models where hyaluronan serves as the memory of the polymer-enzyme molecular machine and Dr. Weigel's model is one of the candidates. By the time of writing this thesis, we are stuck on the measurement of hyaluronan desorption rates versus brush growth time. In the end, this work does not quite reach the final goal of testing Dr. Weigel's mechanical model of hyaluronan length regulation, but the work effort and vision to reach the goal have nearly converged.

5.2 Generic Model of Hyaluronan Length Regulation

Figure 5.1 shows the framework of the generic model of hyaluronan length regulation. We focus on the information processing perspective of the polymer-synthesizing system composed of hyaluronan, hyaluronan synthase, and the external environment. The input information includes the concentrations of chemicals, geometric distribution of hyaluronan synthase, temperature, shear flow and other environmental variables. The output informa-

[1] Instantiation is the creation of a real instance of an abstraction

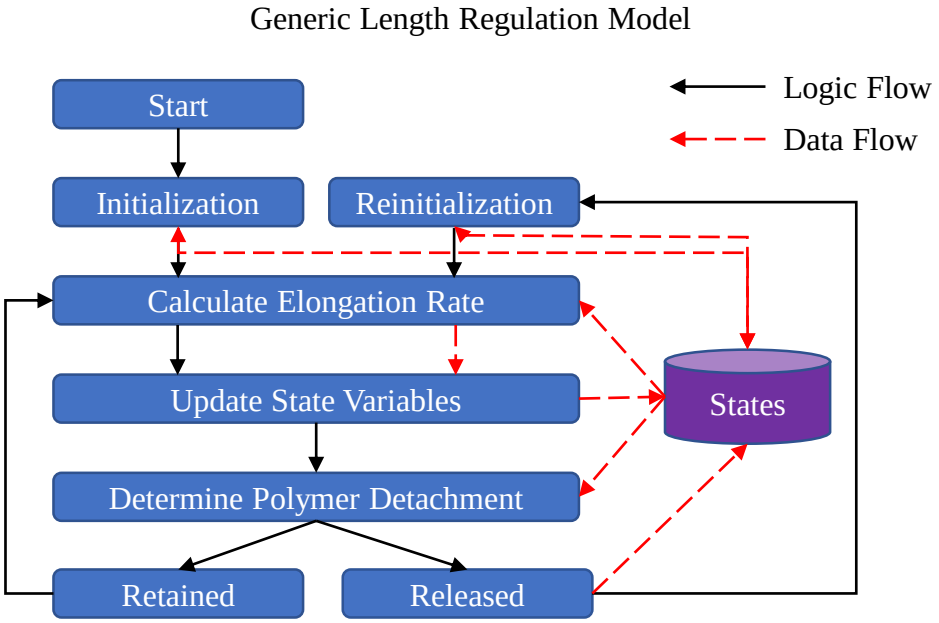

Figure 5.1: Framework of the generic model of hyaluronan length regulation. Logic flows are represented as black solid arrows and data flows are represented as red dash arrows. At the start of the synthesis, there is an initialization step when hyaluronan synthase synthesize a chitin oligomer (only containing GlcNAc monomers) as the primer [48]. Then the system enters the loop of hyaluronan elongation (attaching monomers to hyaluronan). The elongation rate depends on the state variables which may be updated due to the change in hyaluronan length. Then an unidentified mechanism determines, according to the state variables, whether the hyaluronan is retained for another round of elongation or the hyaluronan is released into the solution which consequently terminates the elongation and defines the hyaluronan length. It has been shown that, after the detachment of hyaluronan, hyaluronan synthase moves on to synthesize a new polymer and a hyaluronan synthase enzyme can synthesis multiple hyaluronan polymers within its lifetime [37]. If the hyaluronan is detached, state variables are updated, and the hyaluronan synthase needs to reinitialize. It is unknown whether there is a lag in the reinitialization step. After the reinitialization, the system enters the loop of hyaluronan elongation.

tion is length distribution of hyaluronan attached to the hyaluronan synthases and released into the solution. The system is dynamic and time-dependent. In Figure 5.1 we expand the logic for hyaluronan synthesis and the folded states represent all relevant state variables of the system. Many details must be integrated into this generic model to obtain a concrete model which can be tested against experimental results.

5.3 Elongation Rate Is Constant

In Dr. Weigel's work [37], it has been established for the hyaluronan synthase we are working on (from *streptococcus equisimilis*), under the conditions of sufficiently high concentrations of UDP-sugars and constant removal of the byproduct UDP (which competitively binds to the enzyme with the UDP-sugars), that the rate of the consumption of UDP-sugars is constant for at least eight hours. Our experimental conditions satisfy the criteria for a constant synthesis rate. First, the UDP-sugar was abundant. The mass of UDP-sugars added is 2000 fold of the mass of the final hyaluronan product. This estimation was based on the assumptions that the maximum average molecular mass of hyaluronan is $3\,\mathrm{MDa}$ (see Figure 5.2 A) and a surface density of $1000\,\mathrm{nm}^{-2}$ (see Section 3.1). UDP-sugars are small molecules with a diffusion coefficient on the order of $1 \times 10^3\,\mu\mathrm{m}^2\,\mathrm{s}^{-1}$ which means hyaluronan synthases are never depleted of the substrate. Second, the UDP byproduct was constantly removed from the system via diffusion. UDP has a diffusion coefficient on the order of $1 \times 10^3\,\mu\mathrm{m}^2\,\mathrm{s}^{-1}$. Once produced, a UDP molecule effectively leaves the brush region within $1\,\mathrm{s}$. The final concentration of UDP is 2000 fold lower than the UDP-sugars, and its competition with UDP-sugars for binding with hyaluronan synthases should be negligible. Thus the elongation rate is a constant during the synthesis. Thus, in this chapter, we focus on the understanding mechanism of the detachment of hyaluronan from hyaluronan synthase.

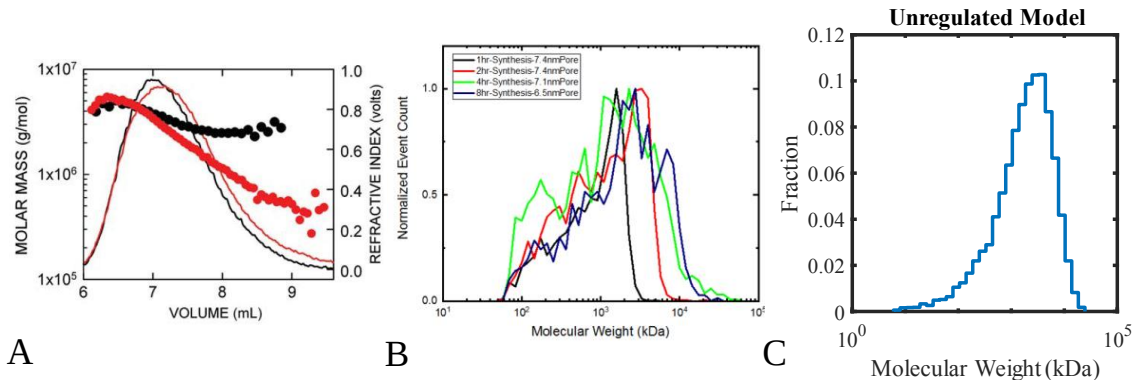

Figure 5.2: **A** size exclusion chromatography multi-angle laser light scattering analysis measured by Bruce Baggenstoss in the Weigel Lab [15].**B** length distribution of hyaluronan measured using nanopore technology to assess polymer length on a single molecule basis [87]. The data were measured by Felipe Rivas in the Hall Lab (Virginia Tech-Wake Forest University School of Biomedical Engineering and Sciences, Wake Forest School of Medicine). **C** Predicted length distribution of hyaluronan generated by the unregulated model.

5.4 Determination of Polymer Detachment Is Stochastic

In the replication of DNA from a DNA template, the synthesis is completed when the new DNA reaches the length of the template DNA [86]. Unlike DNA polymerases, hyaluronan synthase does not have a template, and indeed the final size distribution spans two orders of magnitude, ranging from $0.1\,\mathrm{MDa}$ to $10\,\mathrm{MDa}$ (Figure 5.2B). This indicates detachment of hyaluronan is a stochastic process. In determining polymer detachment (Figure 5.1), a probability which depends on the state variables needs to be calculated, and hyaluronan is released randomly according to the computed probability.

5.5 Unregulated Model

At this stage, we are already able to construct a naive model which is simple enough to obtain analytical predictions. This simple model, which we call the 'unregulated' model, serves as a baseline. We divide the state variables into external variables which describe the environment and internal variables which describe hyaluronan and hyaluronan syn-

Unregulated Model

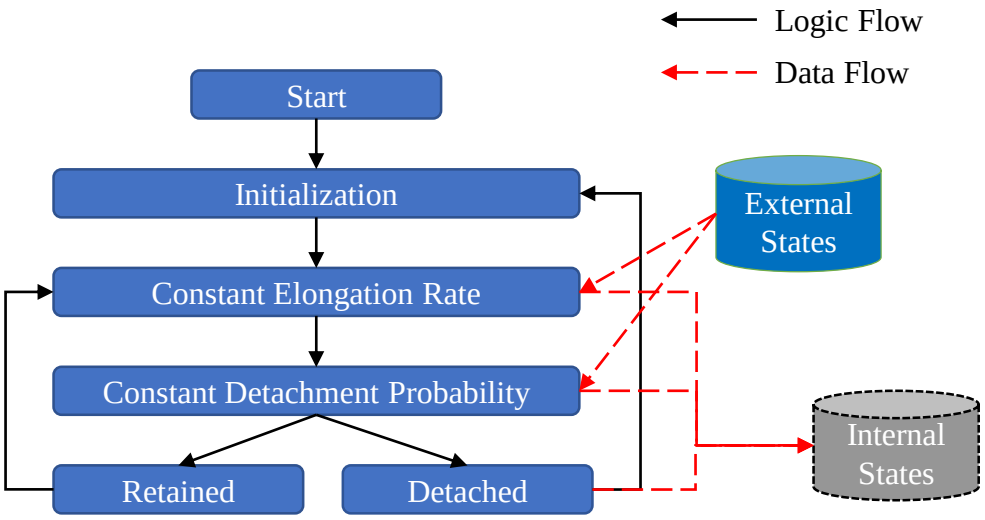

Figure 5.3: Framework of the regulated model of hyaluronan length regulation. Detachment is a stochastic process of a constant probability which only depends on the external variables (not describing hyaluronan and hyaluronan synthase).

thase. The key assumption to be tested in this simple model is that the constant detachment probability p for all polymers does not depend on other variables such as synthesis time, synthesis rate or polymer length. We also assume the initialization and the reinitialization are identical and can be finished in negligible time. The framework of the unregulated model is shown in Figure 5.3.

However, one can quickly assess, as we do below that the prediction of this model does not agree with the experimental results (see Figure 5.2 and Figure 5.6). Comparison with the results, suggests that shorter polymers are less likely to be released than longer polymers -– a necessary assumption to achieve the distribution measured. This leads us to conclude that the probability of polymer detachment p must, in fact, depends on one or more internal state variables.

5.6 Steady State Length Distribution

5.6.1 Prediction of the Steady-state Length Distribution by the Unregulated Model

Given the detachment probability p, the probability of a released hyaluronan of a given length L is equal to,

$$P(L) = p(1-p)^{L-1}, \tag{5.1}$$

which generates a geometric distribution as shown in Figure 5.2 C.

5.6.2 Experimental Results of Steady-state Length Distribution

Length distributions of hyaluronan product measured by size exclusion chromatography–multiangle light scattering [37, 15] and nanopore [87] are shown in Figure 5.2. It is clear to see that the unregulated model fails to predict the length distribution.

5.7 Kinetics in Hyaluronan Brush Thickness During Growth

During the synthesis of hyaluronan of which length distributions were measured, the sample was under constant shaking (using a vibrating Taitec mixer in Dr. Weigel's work [15], and an Innova 44 bacteria shaker in our lab at 250 RPM for the nanopore measurements) which may generate significant shear stress. In this subsection, we compare the prediction of the regulation model and experimental results on the kinetics of hyaluronan brush thickness during growth without shear stress.

5.7.1 Prediction of the Kinetics in Hyaluronan Brush Thickness During Growth

The unregulated model can also be used to help make predictions about the brush height as a function of time. Given a constant elongation rate r (discussed in Section 5.3), at the time t, the maximum possible number of monomers in the polymers is $N = rt$. For a specific

hyaluronan polymer in the brush, its probability of having n monomers at time t is,

$$P(n|N = rt) = c(N, p)p(1 - p)^n, \tag{5.2}$$

where $c(N, p)$ is the normalization factor. This equation states that, in order to reach length n, the previous hyaluronan polymer needs to detach at time $t_0 = (N - n)/r$ and the current hyaluronan has not detached. This length distribution is identified to be a truncated geometric distribution. To simplify the analysis, we approximate the distribution as a truncated exponential distribution $TEXP(\lambda = -\ln(1 - p), N)$ which is the continuous analogue of the discrete truncated geometric distribution [88]. The continuous length distribution of hyaluronan is,

$$f(n|\lambda, N) = \frac{\lambda \exp(-\lambda n)}{1 - \exp(-\lambda N)}. \tag{5.3}$$

We can calculate the average length of polymers in the brush as a function of time t from expectation value of the truncated exponential distribution [89],

$$E(N = rt) = \frac{1}{\lambda}\left[\frac{1 - (\lambda rt + 1)\exp(-\lambda rt)}{1 - \exp(-\lambda rt)}\right]. \tag{5.4}$$

According to the scaling theory for polymer brushes, including polydisperse polymer brushes [42], the average polymer length is proportional to the thickness of the brush, $H \propto E(N)$. As $t \to \infty$, $E(N) \to \frac{1}{\lambda}$ and H approaches a constant which is the height at steady state. We need to point out that as $t \to \infty$, the truncated geometric distribution approaches to a geometric distribution. Thus after sufficiently long growth duration, according to the unregulated model, the length distributions of bound and released hyaluronan are the same. Using this result, we can predict the brush height versus time (brush growth curve) as the enzymes generate the polymers using the unregulated model. In the next section, we compare measurements of brush growth with the prediction of this unregulated model.

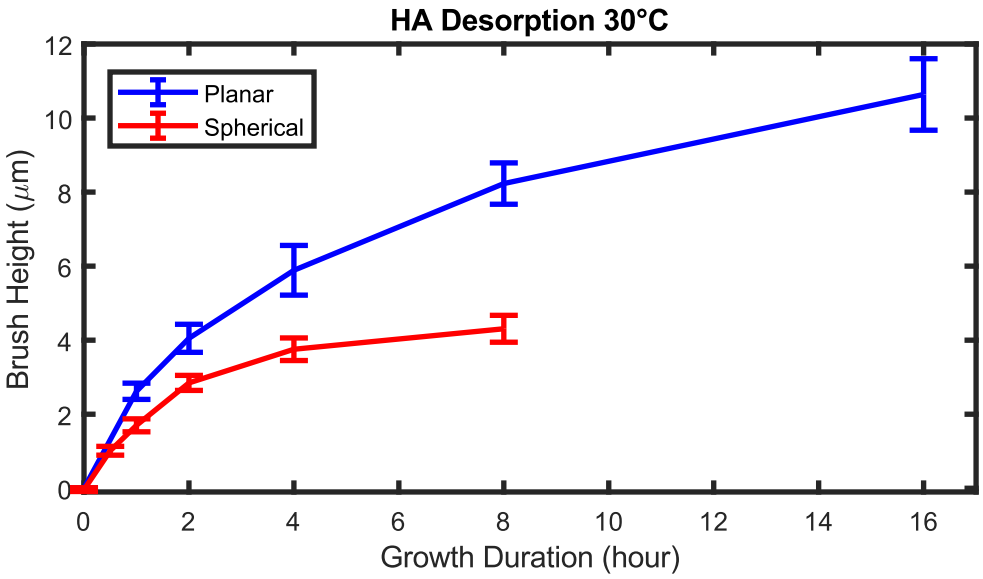

Figure 5.4: Kinetics of a growing planar hyaluronan brush.

5.7.2 Experimental Results of Brush Growth Curves

Planar Hyaluronan Brush

For the data collected in this chapter, we used planar hyaluronan brush configurations where the hyaluronan synthase fragments were coated on coverslips. This configuration allows for fast solution exchange which is required for the following experiments. If we used hyaluronan brushes coated on glass microspheres, we would have great difficulty in not flushing the microspheres away during buffer exchange. Jessica Faubel, a graduate student from our lab, measured the heights of brushes after different growth durations using $200\,\mathrm{nm}$ particle exclusion assay. The results are plotted in Figure 5.4. Here we need to point out a key observation. Assuming the polymer elongation rate is constant as we have discussed in Section 5.3, all the nonlinearity in the growth curve is caused by hyaluronan detachment. Without hyaluronan detachment, the growth curve will be a straight line of which slope equals the elongation rate.

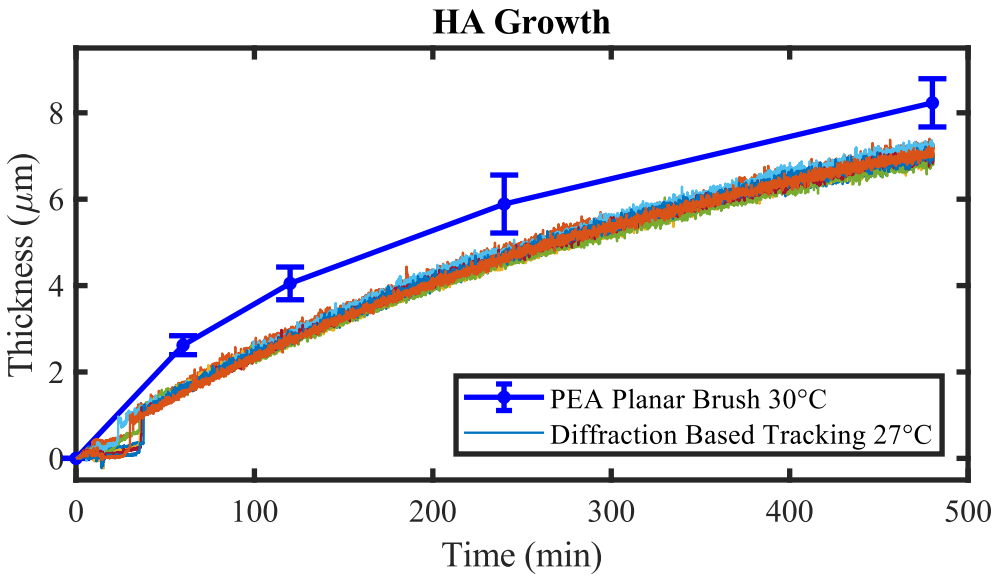

Figure 5.5: Kinetics of the thickness of planar hyaluronan brush using the diffraction-based tracking method. Positions of five tracking beads and two reference beads are plotted. Initially, the tracking beads were stuck on the coverslip due to nonspecific interactions. As the thickness of the brush increased and thus the pressure between the tracking beads and the coverslip, tracking beads were detached from the coverslip. At the same time, the magnitude of Brownian motion of the tracking beads greatly increased. Growth curves measured by particle exclusion assay are also plotted. The experiments were conducted under different temperature thus cannot be compared. However, this figure clearly shows the increased resolution.

High Resolution Growth Curve

It was a lot of work to collect the data to generate the growth curve in Figure 5.4 using particle exclusion technique. It required two hours of active confocal microscopy work to collect each data point with error bars. Furthermore, it is too easy to overfit the unregulated model which has two free parameters using the results from particle exclusion assay which have only five data points. To achieve a strong resolving power on theoretical predictions, we thought higher time-resolution growth curves would be beneficial. We used the diffraction-based tracking method to trace the positions of glass microspheres which settle on the top of the brush and then calculated the brush heights. The beads result in negligible

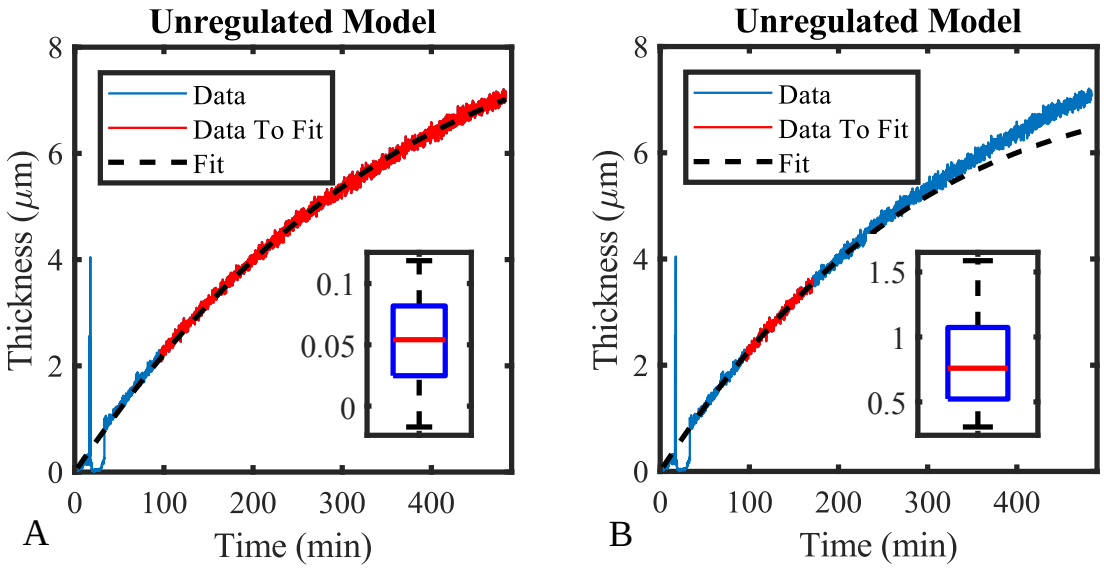

Figure 5.6: Fitting unregulated model to the growth curve. Data used in the fitting is plotted in red. The fitting and the data deviates at a later time. Inset: for each growth curve (N = 24), we calculated the difference between the measured thickness at the end of the curve. The fitting errors (μm) are shown in the boxplots.

compression [2]. We used a stage top incubator to maintain the temperature. The incubator was set to 30 °C but the temperature of the objective was not controlled. Measured using a calibrated thermocouple, the steady-state temperature of the sample was 27 °C. Details of the hardware setup and data analysis procedures are described in the Methods chapter. We measured the growth of the brush using this diffraction based tracking methods. Typical growth curves are plotted in Figure 5.5. As expected, this method has much higher temporal and spatial resolution than the particle exclusion assay.

5.7.3 Comparing with Prediction of the Unregulated Model with the Brush Growth Curves

We fit the growth curve to the prediction of the unregulated model (Section 5.7.1),

$$H(t) = H_\infty \left[\frac{1 - (\alpha t + 1)\exp(-\alpha t)}{1 - \exp(-\alpha t)} \right], \tag{5.5}$$

[2] We can estimate the pressure using $\mathrm{P} = \rho \mathrm{gh}$. The result is less than $0.01\,\mathrm{Pa}$ and negligible compared with the Brownian fluctuation.

where H_∞ is the brush thickness at steady state and $\alpha = \lambda r$. r is the elongation rate and $p = 1 - \exp(-\lambda)$ is the discrete detachment probability. We skipped the data before the microsphere detached from the coverslip and used nonlinear least square fitting. When fitting the model, we used two fitting methods. In the first method, we used all the data after the microsphere has detached. The fitting results are plotted in Figure 5.6 A. In general, the fitting error is small, and there is minor deviation at both ends of the curve. In the second method, we used 1000 data points which spanned $70\,\mathrm{min}$ after the bead detached from the coverslip (Figure 5.6 A). If the model is correct, it should be able to predict the data beyond the fitting data. This time, the fitted curve deviated from the growth curve at around $5\,\mathrm{h}$. We analyzed other growth curves as well using both fitting methods. We quantify the deviation by the difference between the measured thickness and the predicted thickness at the end of the growth (Figure 5.6 Insets). The positive deviation suggests that the brush thickness can surpass the limit set by unregulated detachment. Thus the length of hyaluronan is regulated, at least to some extent. However, the brush growth curves have much lower resolving power to different length regulation models than the length distribution of hyaluronan (Figure 5.2 A).

5.8 Locating the State Variables for Length Regulation

In the above sections, we have seen that the detachment probability is not a constant and has to depend on the internal states of either the hyaluronan polymer or the hyaluronan synthase enzyme. In this section, our goal is to locate the internal state variable on which the detachment probability depends. In Figure 5.7, we build a smart polymer model where the polymer carries the state variable for length dependent detachment. At this point, the state variable is unidentified and abstract. It could be the length of the hyaluronan or some collective variables such as brush thickness. On the flip side, in Figure 5.8, we build a counter model, a smart enzyme model, where the hyaluronan synthase carries the state variable for length dependent detachment.

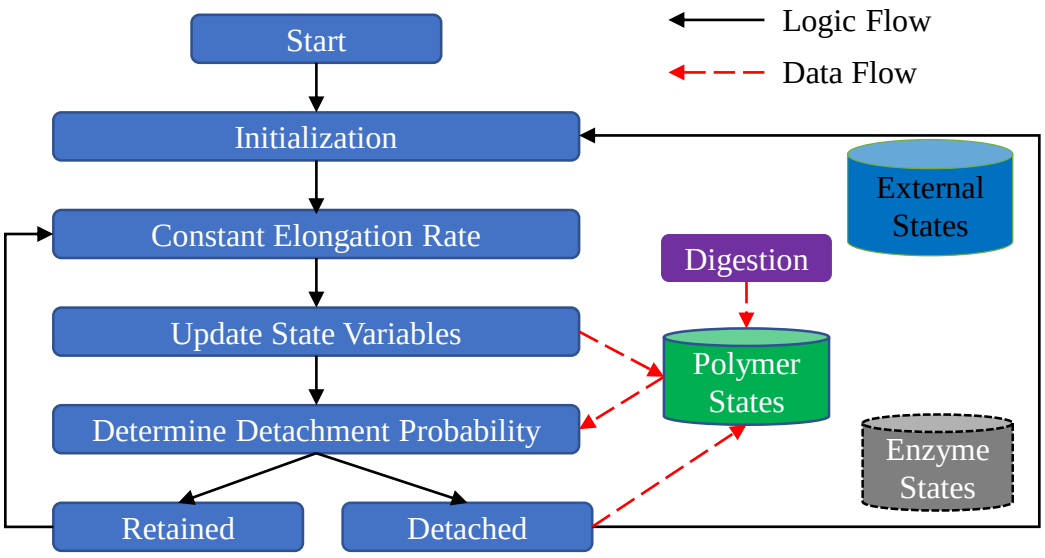

Figure 5.7: Framework of the smart polymer model. Only dynamic data flows are plotted. We call a data flow dynamic if the data sent is time-dependent or the target variables change with time. Comparing with the unregulated model (Figure 5.3), the detachment probability is dynamically influenced by the states of the polymer. Hyaluronidase can digest hyaluronan and thus reset the state variables which consequently reset the detachment probability.

We design an experiment where the two models predict different brush thicknesses. The results support that hyaluronan carries the state variable for length regulation. Details of the models, experiment, and results are presented below.

5.8.1 Smart Polymer Model versus Smart Enzyme Model

In the smart enzyme model, the hyaluronan synthase can record the number of the cycles of attaching monomers to the polymer. The hyaluronan synthase has been found to have seven functions to synthesize hyaluronan [19]. It is beyond our imagination to fit a counting mechanism into the 417-amino-acid protein, but we need experimental evidence to rule out the smart enzyme model.

In the smart polymer model, the hyaluronan polymer serves to record and report the length of itself effortlessly. To us, this is a far more plausible hypothesis compared with the alternative smart enzyme model.

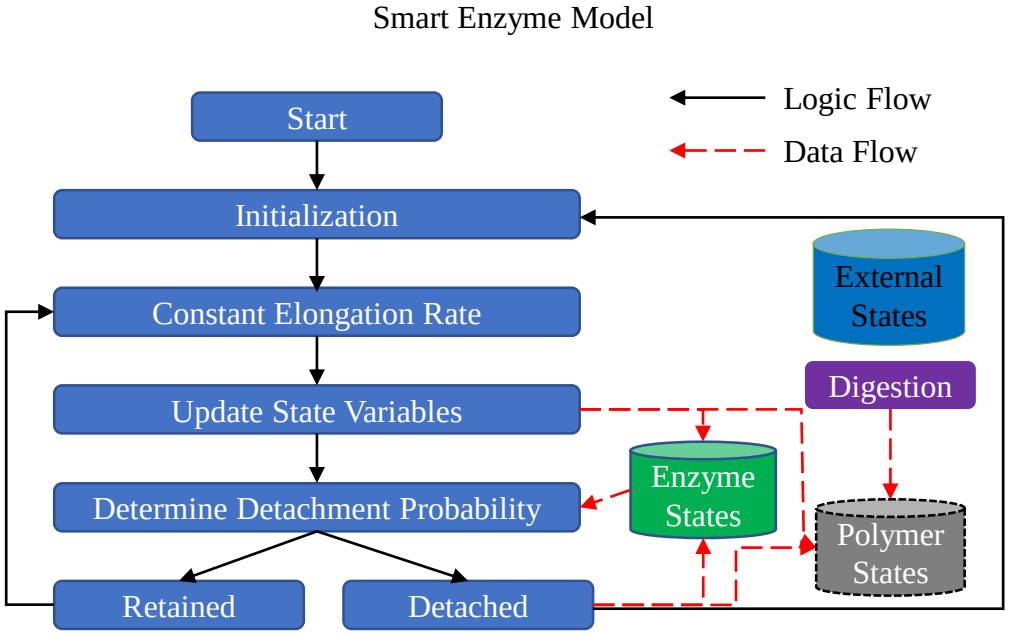

Figure 5.8: Framework of the smart enzyme model. Similar to Figure 5.7, only dynamic data flows are plotted. Comparing with the smart polymer model (Figure 5.7), the detachment probability depends on states of the hyaluronan synthase enzyme instead of the states of the polymer. Digestion of the polymer does not alter the states of the enzyme nor the detachment probability.

5.8.2 Designing the Experiment to Discriminate the Models

The nonlinearity of the growth curve in Figure 5.4 provided us with the insight to design the experiment. In the first two hours, the thickness of the brush increased by $4\,\mu\mathrm{m}$. In contrast, in the last two hours, the thickness of the brush only increased by less than $2\,\mu\mathrm{m}$. In both the smart enzyme model and the smart polymer model, if the state variable which controls the detachment probability, the hyaluronan-synthesis system will also be reset and the growth curve will follow a pattern as if the synthesis were just started. Figure 5.9 shows the predictions of both models after the state variables of hyaluronan are reset.

We had a method to reset the hyaluronan using the hyaluronidase which digests hyaluronan into short fragments made of a few disaccharide units [90]. The part of the hyaluronan exposed to the solution is effectively digested by the hyaluronidase, as confirmed with particle exclusion assay in Chapter 4. In terms of part of hyaluronan, the type I-S hyaluronidase from bovine testes we used has a molecular mass of $55\,\mathrm{kDa}$ and is too big to have access into the pore of the $48\,\mathrm{kDa}$ hyaluronan synthase [19]. Thus the part of hyaluronan inside the pore of the hyaluronan synthase should be intact during the hyaluronan digestion. The bovine hyaluronidase targets the $1 \rightarrow 4$-linkage in hyaluronan [90] and we did not find evidence in the literature that it has specific interaction with hyaluronan synthases. Thus we assume the state variables of hyaluronan enzyme stay intact when the hyaluronidase is added.

5.8.3 Experimental Methods

In the experiment, hyaluronidase was added after $6\,\mathrm{h}$ of hyaluronan growth. After thoroughly removing the hyaluronidase, we continued the synthesis for two hours.

5.8.4 Predictions

We define $H(t)$ as the brush thicknesses measured using the particle exclusion assay (Figure 5.4). As shown in Figure 5.9A, the smart enzyme model predicts that, as everything

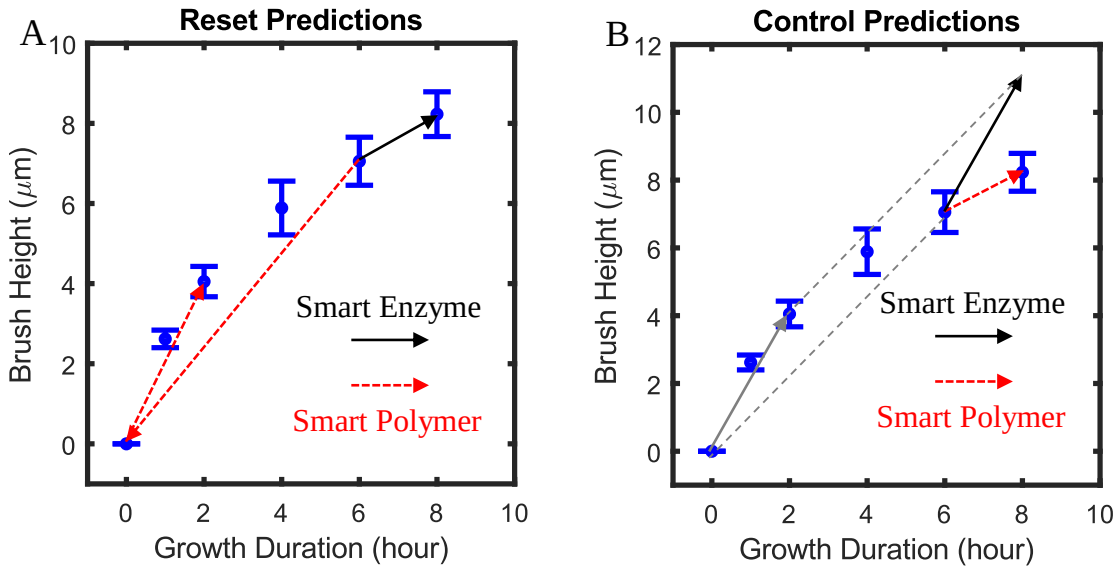

Figure 5.9: Changes in the key state (controlling detachment probability) variables and predictions by the two models. **A** Hyaluronidase is added at $6\,\mathrm{h}$. **B** control experiment without hyaluronidase (See Section 5.8.6).

is intact during the hyaluronidase treatment, the thickness of the brush should increase to $H(8hour) - H(6hour) < 2\,\mu\mathrm{m}$. In contrast, the smart polymer model predicts that the thickness of the brush should increase to about $H(4hour) \sim 4\,\mu\mathrm{m}$, following the growth curve starting from the beginning.

5.8.5 The Results

The result is shown in Figure 5.10 A. The measured brush height from the second growth agrees with the predictions by the smart polymer model. The deviation of the brush height from the prediction is most likely from the residual hyaluronidase in the sample. During the hyaluronidase treatment, there was a sudden change in the concentration of UDP-sugars. One who supports the smart enzyme model may argue that this sudden change can reset the state variables of the hyaluronan synthase which leads to the same result as the smart polymer model. Thus, we performed a control experiment described below.

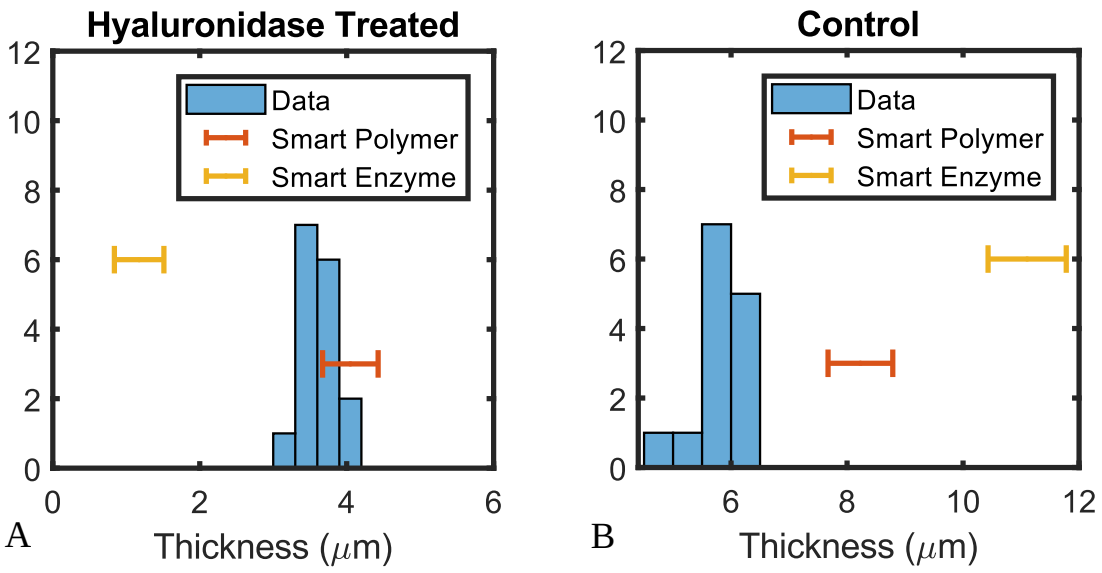

Figure 5.10: Predictions and results of interrupted and then continued brush growth. **A** A brush was digested using hyaluronidase before the second growth phase. **B** Control experiment without hyaluronidase. Each data point in the histogram represents the average thickness of the brush measured in a $53\,\mu\mathrm{m}$ by $53\,\mu\mathrm{m}$ field of view using particle exclusion assay.

5.8.6 Hyaluronan Synthase Is not Affect during Hyaluronidase Interruption

To exam the influence of this sudden change on the state variables of the hyaluronan synthase. We performed a control experiment where everything was the same as the experiment above except that hyaluronidase was not added to the sample. According to the corrected smart enzyme model, the final thickness should be $\sim H(6hour) + H(2hour) \sim 11\,\mu\mathrm{m}$. In contrast, the smart polymer model predicts that the final thickness is simply the thickness of an $8\,\mathrm{h}$ fresh growth. The predictions by the two models are presented in Figure 5.9 B.

The result is shown in Figure 5.10 B. The thickness of the brush agrees with neither of the models. More troubleshoot and research are needed. At this point, we hypothesize either the brush was damaged during the washing steps or EDTA, which was added between the two growth steps and slowed down the synthesis, was not effectively washed out before the second growth step. We also had issues with washing out the chemical in the section below

where we tried to measure the hyaluronan detachment rate.

5.9 Length Dependent Desorption Rate of Hyaluronan

In the previous section, we showed that the hyaluronan polymer under synthesis most likely served as the counter of the hyaluronan-synthase system. In this section, we look deeper into how hyaluronan might regulate its own detachment probability.

The size of the hyaluronan product spans two orders of magnitude. This indicates that the detachment of hyaluronan is a stochastic process. This is different from the synthesis of DNA where the product has the identical length as the DNA template.

In the remaining of this section, we present the discussion about the dependence of the synthesis rate on the polymer length. We also present our preliminary experiments to measure the dependence of the desorption rate on the polymer length.

5.9.1 Desorption Rate and Polymer Length

Under the conditions of a constant synthesis rate, the length regulation mechanism is mainly achieved through the length dependent desorption probability $\mathrm{p(l)}$. This also means that the nonlinearity in the growth curve (Figure 5.4) must arise solely from the release of hyaluronan. In the first two hours, the growth curve is mostly linear, and then the slope of the curve starts to deviate from the initial growth rate because polymer desorption becomes significant. We designed a set of experiments to compare the desorption rate of brushes of different lengths. If as we hypothesize, length-dependent desorption exists, we should see a difference in desorption rates for thinner and thicker brushes.

5.9.2 Experimental Method

We measured the desorption rate of brushes which were grown for 1, 2 and 8 hours before the synthesis was quenched (See Section 3.7.8 for how we extract desorption rate from the height curves). The thicknesses of different growth durations are approximately $2\,\mu\mathrm{m}$,

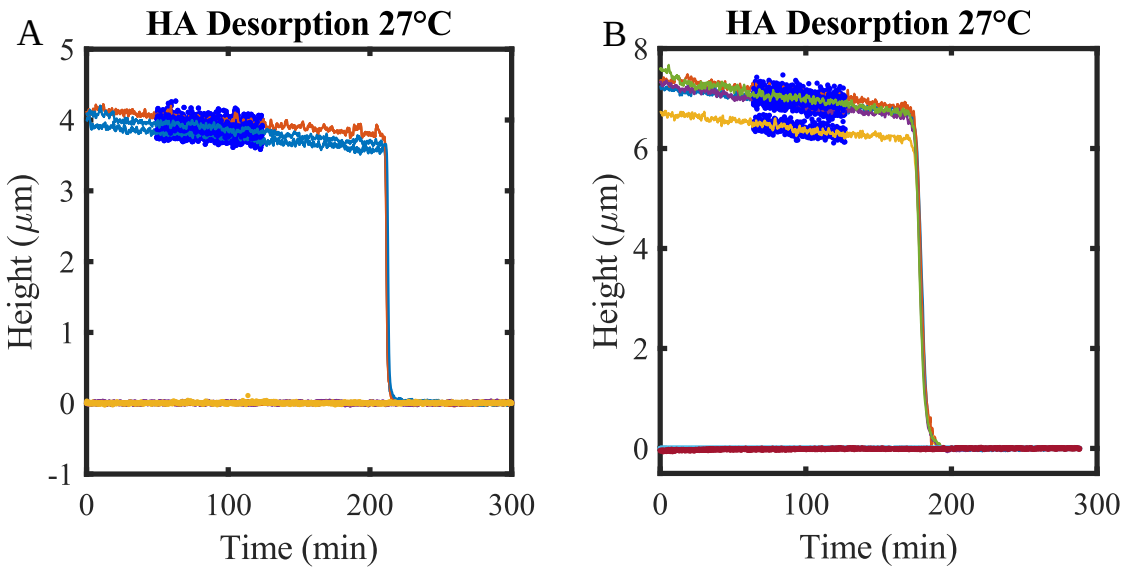

Figure 5.11: Representative desorption curves. **A** desorption experiment on a $4\,\mu\mathrm{m}$ brush. **B** desorption experiment on a $7\,\mu\mathrm{m}$ brush. Data used to generate the results are labeled in blue. The rapid reduction around $200\,\mathrm{min}$ was due to digestion by hyaluronidase to calibrate the particles at the end of the experiment.

$4\,\mu\mathrm{m}$ and $7\,\mu\mathrm{m}$. Experiments were repeated three times for each growth duration. Based on the shape of the growth curve which is linear at shorter times $< 2\,\mathrm{h}$, we predicted the $2\,\mu\mathrm{m}$ brush and the $4\,\mu\mathrm{m}$ brush would have similar desorption rates and that those rates would be sizably smaller than the $7\,\mu\mathrm{m}$ brush.

5.9.3 Preliminary Results

Desorption Experiment I

Figure 5.11 shows representative data from the desorption experiments. In these experiments, we track beads in multiple fields of view on a brush of a given starting height. The height of the beads versus time is collected for $2\,\mathrm{h}$. Figure 5.12 plots the statistics of the desorption rates for the brushes of three initial heights. Experiments on $2\,\mu\mathrm{m}$ and $7\,\mu\mathrm{m}$ brushes were repeated three times. Each data point represents results from tracking one bead. The desorption rate was on the order of $6\,\%$ per hour. The $7\,\mu\mathrm{m}$ brushes had statistically significantly higher desorption rate than the $4\,\mu\mathrm{m}$ brushes by $3\,\%$ per hour. Data for

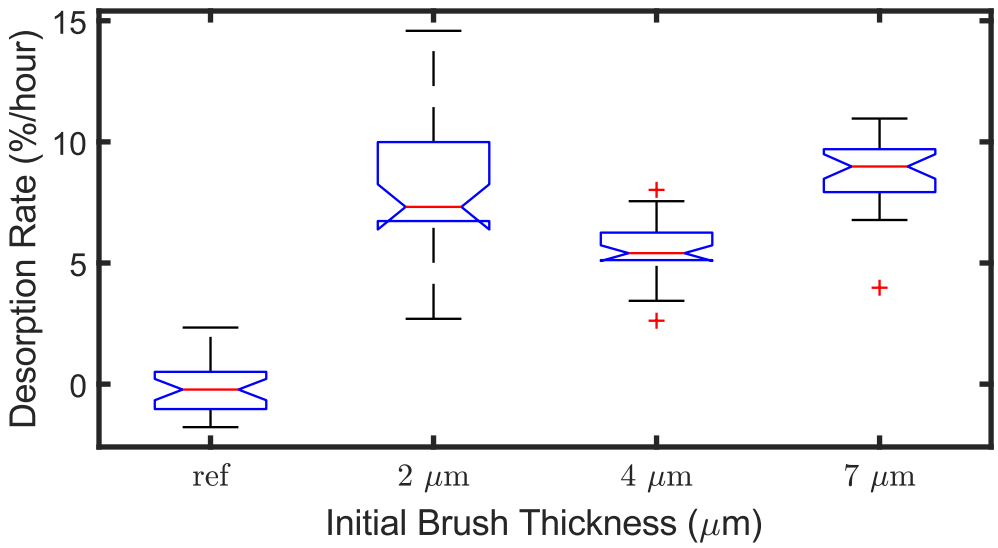

Figure 5.12: Desorption rates of brushes of different initial thickness. The value labeled 'ref' is the slopes of the position of reference beads relative to other reference beads.

the $2\,\mu\mathrm{m}$ brushes had a much larger variance. Its range covered the values for both the $4\,\mu\mathrm{m}$ brushes and the $7\,\mu\mathrm{m}$ brushes. The results are not conclusive. The relatively fast desorption rates measured in the $2\,\mu\mathrm{m}$ experiments made us suspect the quenching step is leading to varied results. Worse quenching will lead to continued growth that competes with desorption. If there were variations in the efficiency of quenching across different experiments, we might miss the length dependent effect due to random errors.

Desorption Experiment II

In the later experiments, we increased the strength of the washing in the quenching step. Between exchanging the liquid in the sample, we pipetted half of the liquid up and down while horizontally moving the pipette tip for seven times. With the new washing method, we observed a desorption rate which was four times as fast in an experiment on a $7\,\mu\mathrm{m}$ brush (Figure 5.13A). However, we could not repeat this result in the next two experiments. We also did two experiments on $4\,\mu\mathrm{m}$ brushes. The results are shown in Figure 5.13B. This time, the results suggest there was no observable difference between the desorption rates.

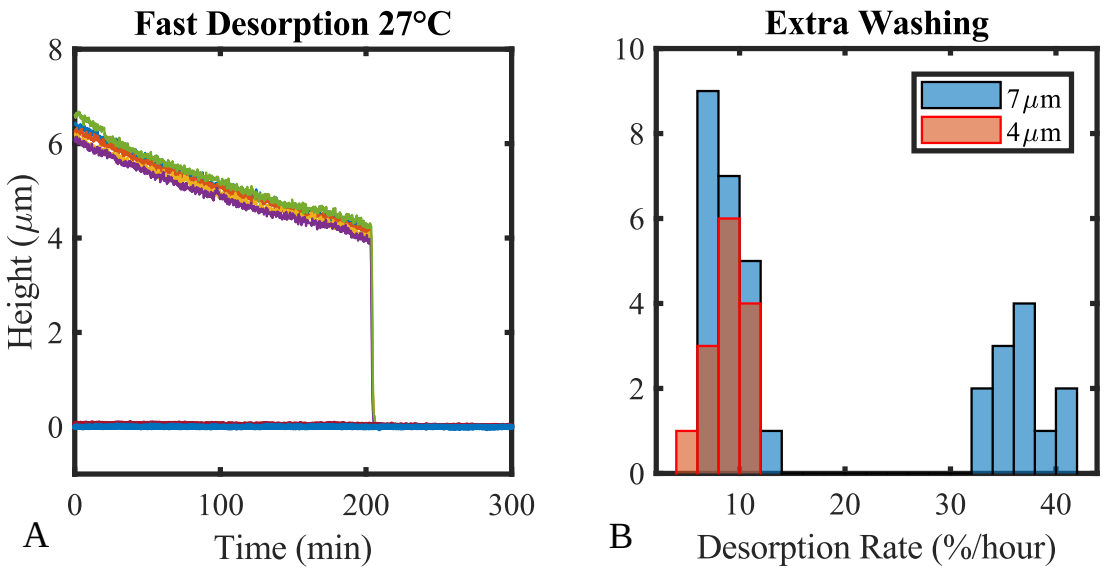

Figure 5.13: Desorption rates of brushes where extra flushing was performed in the quenching step. **A** An experiment of unnormal desorption rate. **B** Inconsistent desorption rates measured in two 7 µm samples.

5.9.4 Conclusion

We cannot draw any conclusion on the length dependent desorption rate. The experiments are very sensitive to the washing method in the quenching step. We encountered a similar issue when trying to exchange the solution in the previous section thoroughly. As Dr. Weigel commented in an email exchange,

> ... It's humbling to realize how naive we can be about how even simple procedures (like washing a slide) are far more complex than we imagine.

, we need to design a better method and probably a special sample holder for efficient solution exchange before we can precisely measure the desorption rate of hyaluronan polymers of different lengths.

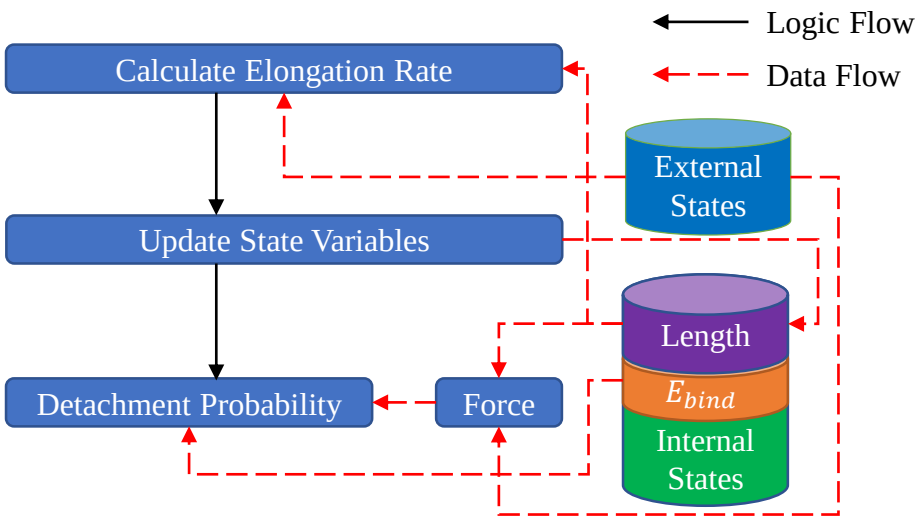

Figure 5.14: Information processing in Dr. Weigel's mechanical model. Only the model-dependent pieces are shown. Hyaluronan length indirectly regulates the detachment probability via the polymer tension. An isoform of hyaluronan synthase of stronger binding energy to hyaluronan has a lower detachment rate [91]. External states, such as shear flow, can influence the releasing force, potentially in a length-dependent manner.

5.10 Summary

In this chapter, we attempted to bring insights into the length regulation mechanism of the hyaluronan synthesis. Our preliminary results favor a model where the hyaluronan polymer serves as the memory of the length regulation mechanism. We could not conclude the predicted length dependent desorption rate, and more investigation is needed. We hope future researchers can ultimately test Dr. Weigel's mechanical length dependent model as shown in Figure 5.14.

CHAPTER 6

TESTING THE POTENTIAL OF APPLICATIONS IN IMPLANTS

6.1 Overview

In this chapter, we report our work to explore one particular avenue of enzyme-synthesized hyaluronan brushes for biomaterial applications. Specifically, we studied the possible application in implants. Biofilm formation is one of the most common causes of implant failure, resulting in patients suffering from at least one additional surgery [92, 93, 94, 95]. Biofilm is a sessile microbial community containing bacteria which are strongly attached to a surface and the extracellular polymeric substance produced by the bacteria [96]. Biofilms often defy both defenses of the immune system [97, 98, 99] as well as the actions of antimicrobial agents [100] and are infamously difficult to remove from surfaces. Thus it is essential to develop anti-bacterial materials that prevent biofilm adhesion to start with through a combination of antimicrobial activity (biocides) as well as through a non-fouling scheme.

A lot of research has shown that polymer brushes are a promising material to prevent the formation of biofilm [101, 102, 103]. Further, hyaluronan, in particular, is recognized for its non-fouling properties in that it does not allow proteins to stick [104]. These factors combined with the fact that hyaluronan is already an FDA approved biomaterial makes the hyaluronan brush platform particularly interesting to investigate, in addition to the fact that it is a novel configuration that also potentially has regenerative properties. Indeed, the brush thickness and its established ability to reject $100\,\mathrm{nm}$ particles and smaller from penetrating the brush, let alone reaching the underlying surface $5\,\mu\mathrm{m}$ to $10\,\mu\mathrm{m}$ below indicates that they should be extraordinarily effective at preventing bacterial from reaching the surface. According to our results from the particle exclusion assay, our hyaluronan brush should be

able to block both bacteria and mammalian cells from reaching the grafting surface as long they do not produce enzymes that digest hyaluronan such as the hyaluronidase.

We studied the interactions between bacteria and mammalian cells with our hyaluronan brush. We used a biofilm-forming bacteria *Pseudomona aeruginosa* and mouse embryonic fibroblasts which generate the pericellular matrix. The experiments require an environment which is not friendly to the hyaluronan synthase. Both the bacteria and the fibroblasts prefer $37\,^{\circ}\mathrm{C}$. The reducing agent DTT is also poisonous to the bacteria and the fibroblasts. Thus, unless stated otherwise, we used reinforced hyaluronan assembly. The brush was allowed to grow for eight hours before the reinforcement treatment.

6.2 *P. Aeruginosa* Growth and Biofilm Adhesion to Hyaluronan Brushes

Pseudomona aeruginosa is one of the most frequent etiologic agents in implant infections [105]. The bacterial strain *Pseudomona aeruginosa* (PA01) was added with LB broth on top of the prepared hyaluronan brushes. To probe the limits of the brush, we purposely selected this environment which is friendly to the bacteria but challenging to the hyaluronan brush. More detailed description of the experiments can be found in the Method Chapter 3.8.1.

Figure 6.1 shows the representative XZ image of bacteria at the brush interface. As expected from preliminary work with particles, the brush fully prevents the bacteria from reaching the surface, holding them at the brush edge. The brush was able to block the bacteria for at least two weeks (we stopped the experiments then). Very rarely, a bacteria cell reached the surface, and its long-axis was usually perpendicular to the surface. We noticed that the brush height reduced faster compared with the experiment measured at room temperature in bacteria-free solution 4.16. This faster thickness reduction rate might be caused by the elevated temperature and polymer digestion by enzymes secreted by the bacteria.

Biofilms are notoriously known for the difficulty in detaching them from surfaces they adhere to. To test the formation of biofilm on the brush, we relatively gently washed the

sample (see Section 3.8.1 for the washing method). Figure 6.2 shows the representative XY image after gently washing the sample. Images were taken at the height where the bacteria closest to the surface was found. The results indicate that the biofilm was not formed.
We hypothesized, besides the anti-fouling property of hyaluronan, the hyaluronan assembly formed a hydrous and soft interference which lack the mechanical clue for bacteria to adhere and form the biofilm.

6.3 Fibroblast Locally Digesting Hyaluronan Brush and Proliferating

Mouse embryonic fibroblasts transected to express GFP-vinculin were added on top of the brush. Detailed procedures can be found in Section 3.8.2. We took time-elapse differential interference contrast images of the fibroblasts (N $\approx$ 40) over a period of $12\,\mathrm{h}$. Image representing key events are shown in Figure 6.3-6.6. In the beginning of the experiment, the cells were not able to reach the coverslip and blocked by the brush (Figure 6.3). However, in contrast to the *Pseudomona aeruginosa* bacteria, fibroblasts started to reach and spread on the surface of the coverslip within $40\,\mathrm{min}$ (Figure 6.4). At later time, they full spread on the surface and migrated. After $10\,\mathrm{h}$ since settlement, some cells detached from the surface and started to divide (Figure 6.5 and Figure 6.6). This experiment suggests that fibroblasts were healthy and proliferating on the hyaluronan brush.
According to the particle exclusion assay (Section 4.5.1), Fibroblasts are too big to penetrate the brush. We speculate that fibroblasts secreted hyaluronidase which digests the hyaluronan brush and then reached the coverslip. We used particle exclusion assay to visualize the brush after the fibroblasts were seeded overnight. In Figure 6.7 A, $200\,\mathrm{nm}$ nanoparticles were able to reach the coverslip in part of the area. This indicates the brush was digested in vicinity of the cells. We speculate the hyaluronidase may be anchored on the cell membrane. It has been shown that, in a human breast tumor cell line, a hyaluronidase enzyme HYAL2 is GPI-anchored at the plasma membrane [106, 107].
Another interesting phenomenon is that the contact area between the cells and the coverslip

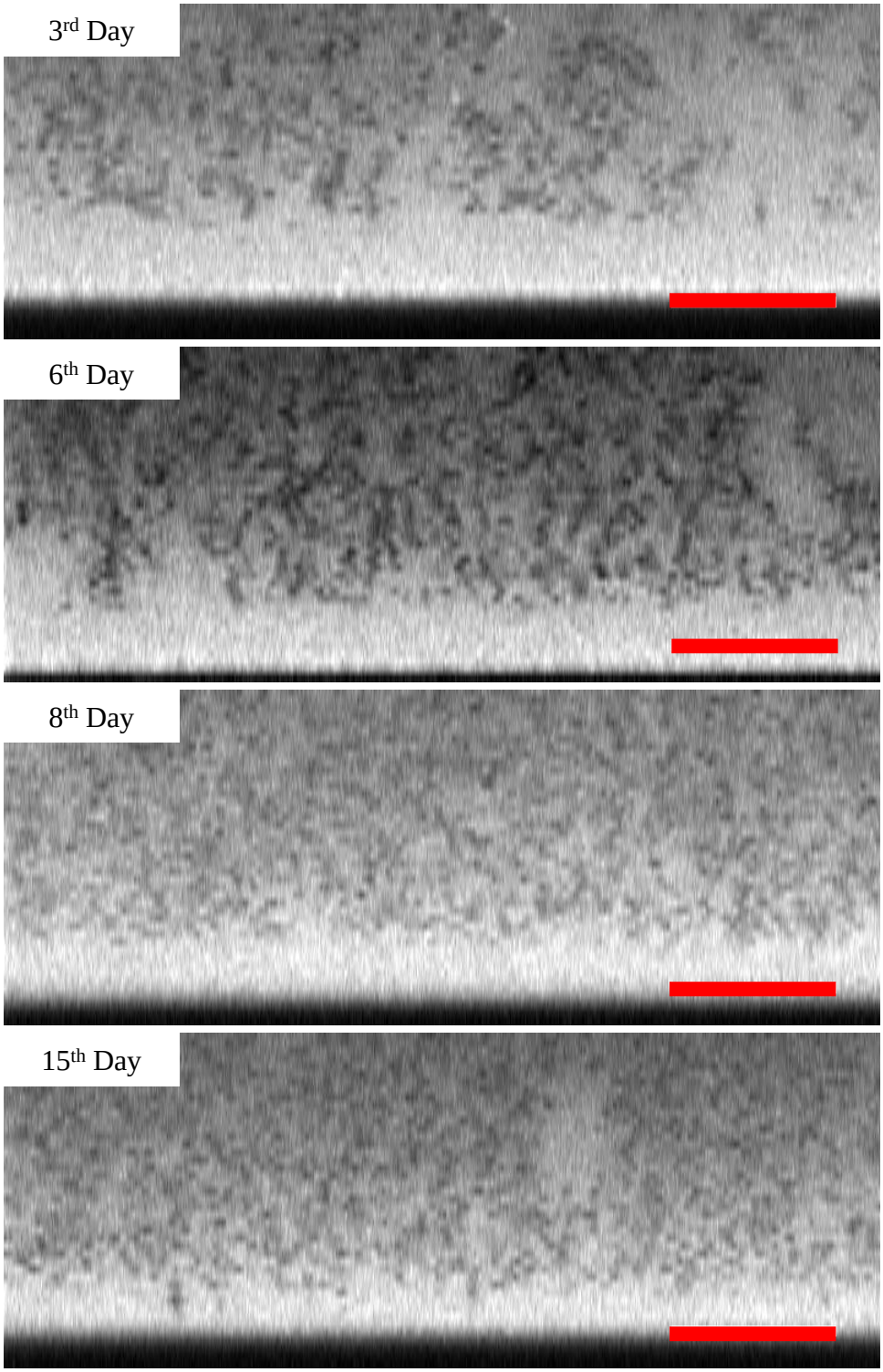

Figure 6.1: Bacteria at the brush interface. Bacteria are inversely labeled with fluorescent dextran which does not enter the bacteria. The coverslips are shown as dark horizontal bands. The brush is between the bacteria and the coverslip. Scale bars are $10\,\mu\mathrm{m}$.

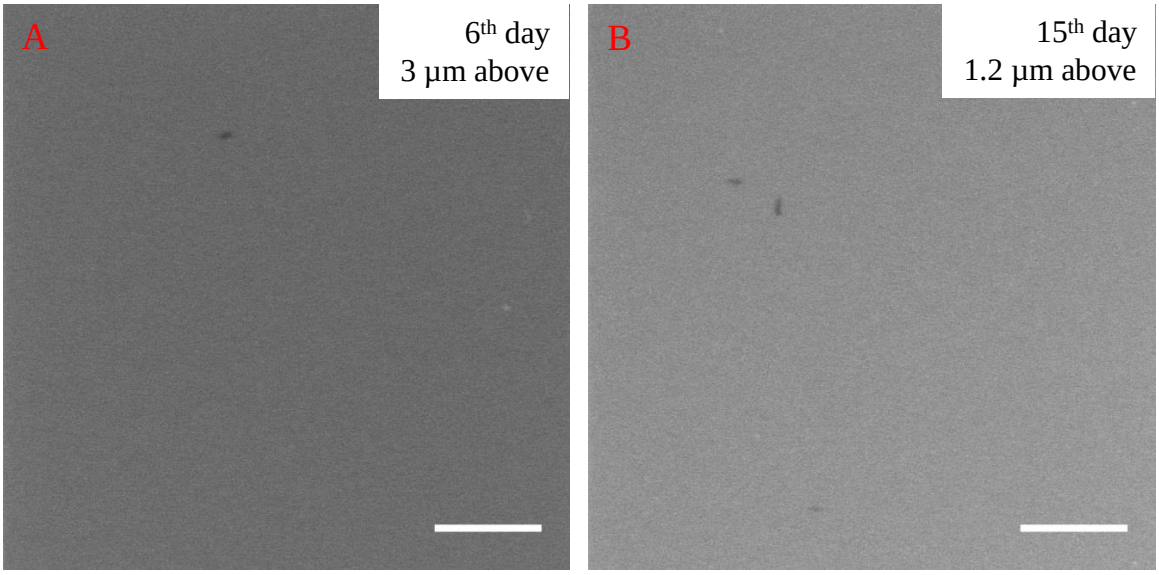

Figure 6.2: Images from two samples after gentle washing. Bacteria closest to the coverslip were images. Scale bars are $10\,\mu\mathrm{m}$.

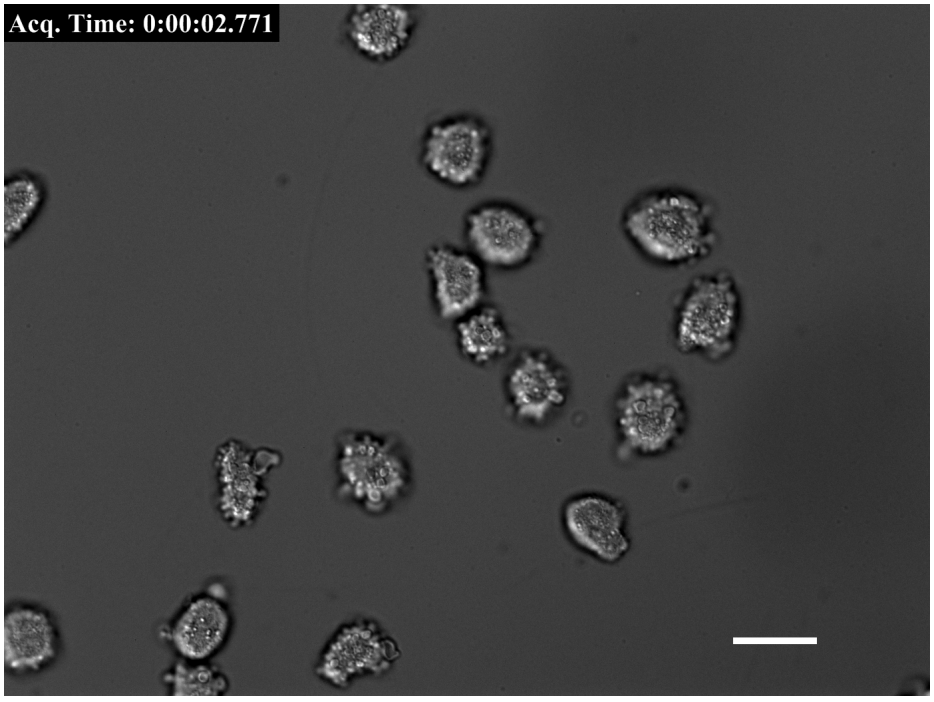

Figure 6.3: Cells settled on the top of the brush. The objective was focused on the coverslip and the cells were not fully in focus. Scale bar is $20\,\mu\mathrm{m}$.

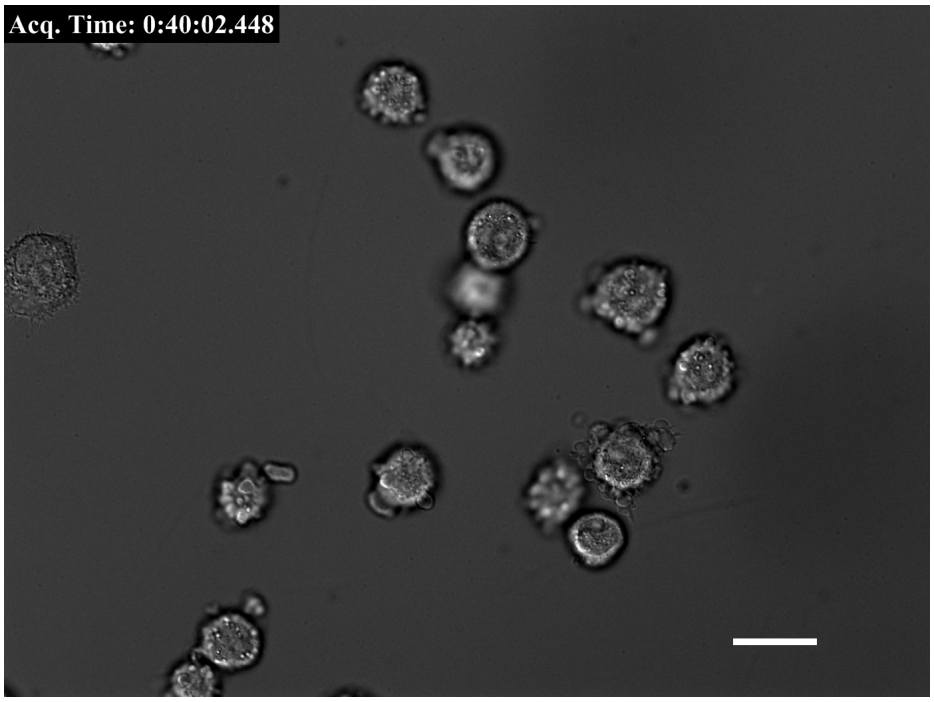

Figure 6.4: Cells reached the coverslip. Scale bar is 20 µm.

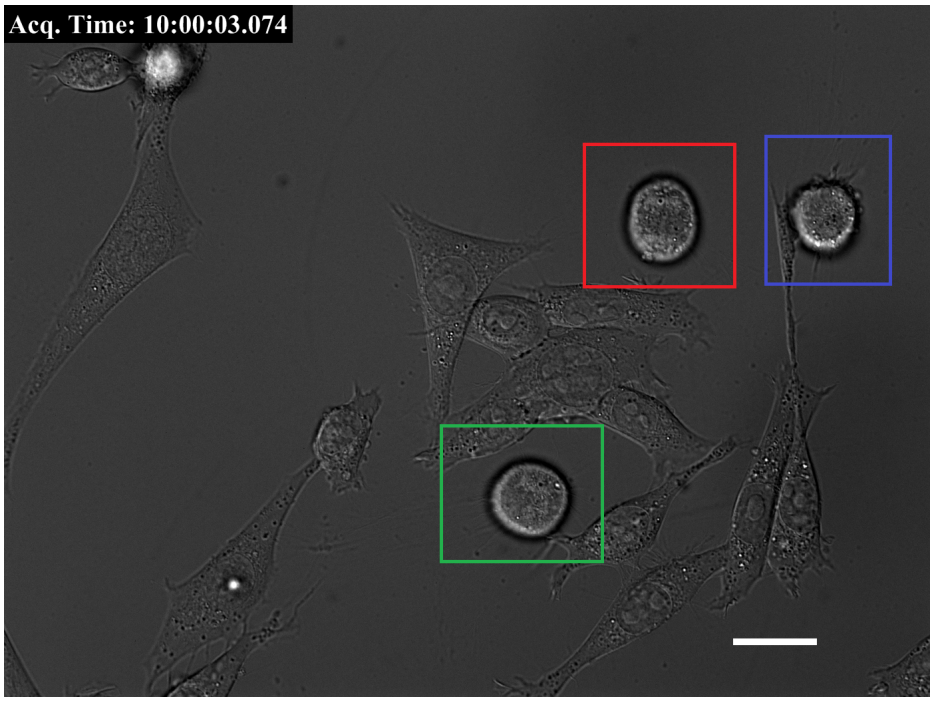

Figure 6.5: Cells spread, migrated and proliferated on the coverslip. Three cells had detached from the surface and were about to divide. Scale bar is 20 µm.

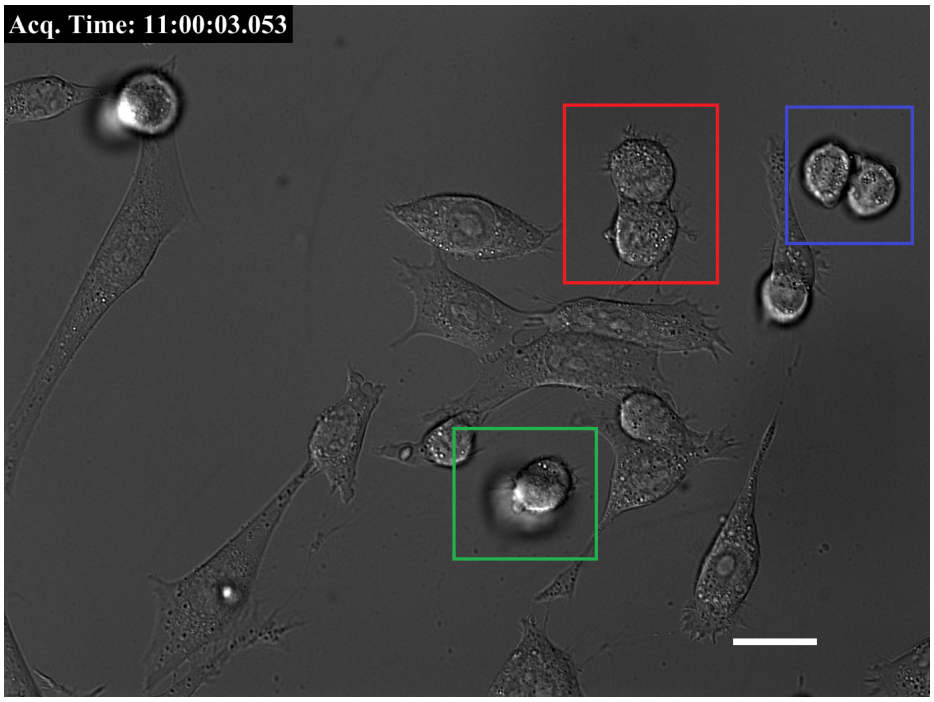

Figure 6.6: The three cells identified in the previous image (Figure 6.5) had divided and started to spread on the coverslip. Scale bar is 20 µm.

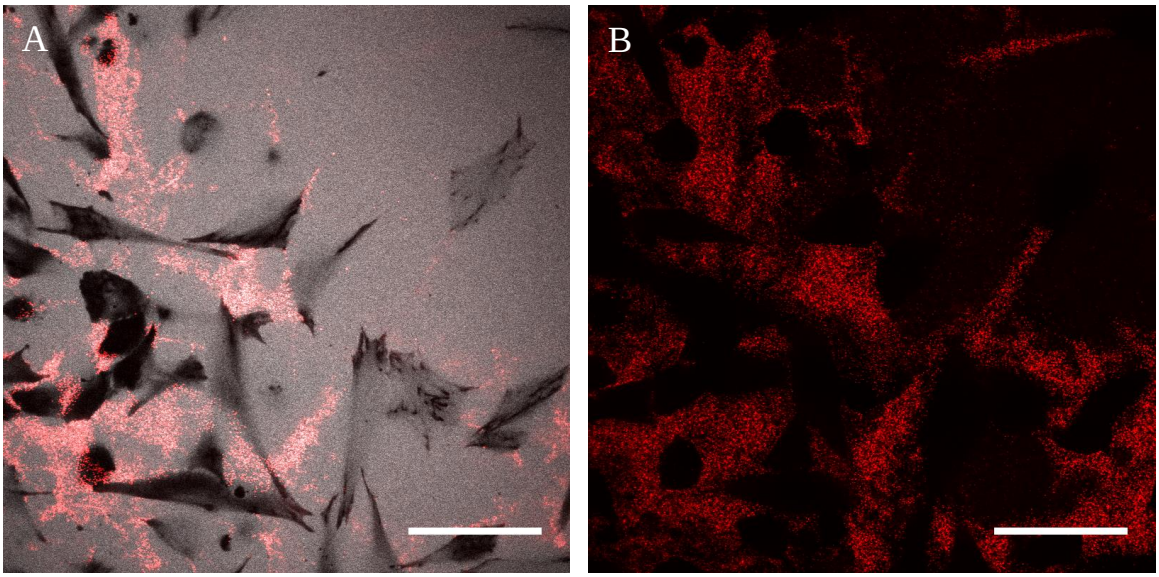

Figure 6.7: 200 nm nanoparticles and 10 kDa dextran were used to visualize the brush and the fibroblasts. Fibroblasts were incubated on reinforced hyaluronan assembly overnight. **A** image taken at the surface of the coverslip. Cells were well spread on the surface. **B** 2.8 µm above the coverslip. The brush was locally digested by the cells. Scale bars are 50 µm.

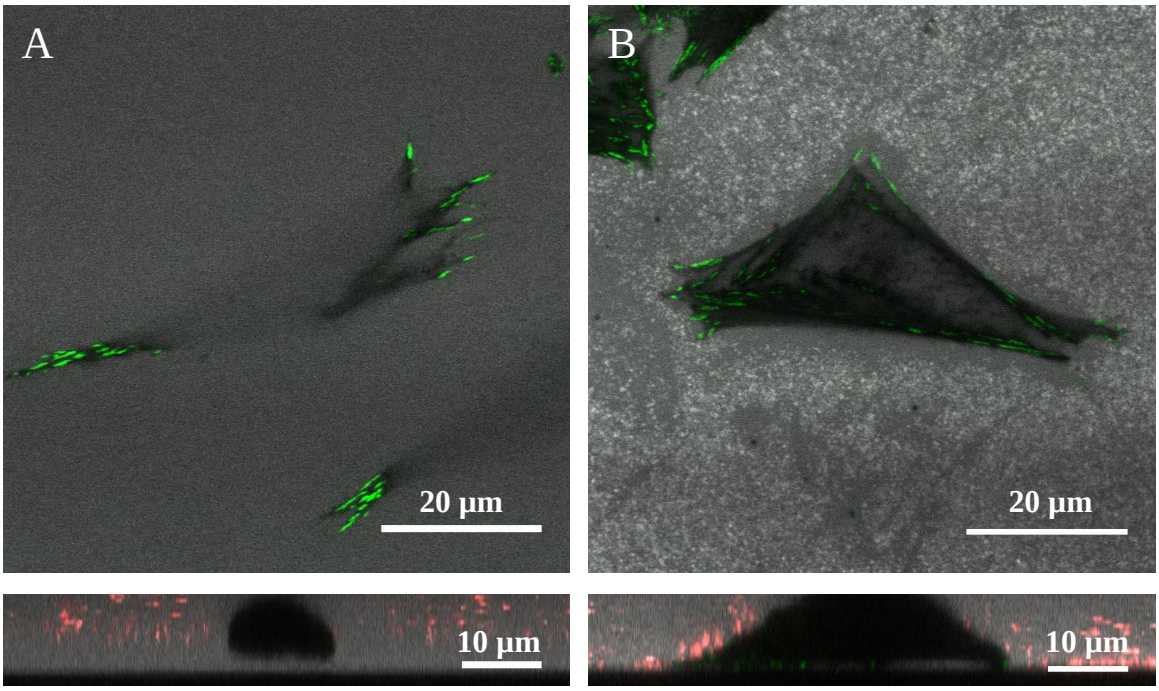

Figure 6.8: **A** A fibroblast on hyaluronan brush. The cell expressed GFP-vinculin in the focal adhesions. In the non-focal-adhesion area beneath the cells, there is strong dextran signal indicate the cell is not in contact with the coverslip. The gap is more visible in the XZ slice than in the XY slice. **B** A fibroblast on a coverslip with hyaluronan brush. The gap between the cell and the coverslip is much smaller compared with Figure **A**.

is much smaller than in the control experiment on coverslip without hyaluronan brush. In Figure 6.8, there is a $700\,\mathrm{nm}$ gap between the cell and the coverslip. We think the gap is filled with hyaluronan, but we do not know whether the hyaluronan is remnant from the brush or possibly part of the cells' pericellular matrix, which is abundantly evident on the top of the cell. Fluorescently label the hyaluronan brush during the reinforcement treatment will help to discriminate.

6.4 Summary

We have seen that the hyaluronan brush can block the *Pseudomona Aeruginosa* bacteria for at least two weeks while allows for fibroblasts to attach and proliferate. In the context of implants, we speculate that cells will preferentially cover the surface of the implant over the bacteria which greatly reduce the probability of the formation of biofilms. However, more research and test are needed before in vivo experiment.

In Figure 4.2, we see that only $\approx 30\,\%$ of the surface is covered by membrane fragments even though we used saturating concentration of membrane fragments.

The membrane fragments we used are from *E. coli* bacteria and may contain endotoxin which may trigger serious immune response such as fever and septic shock [108]. The are three potential methods to prepare endotoxin-free hyaluronan brush. We can use detergent to extensively wash the brush after the reinforcement treatment (Section 4.5). We can expression hyaluronan synthase in detoxified bacteria strains [109]. We can collect membrane fragments from mammalian cells which over-express hyaluronan synthases.

In Figure 6.7, there are small regions around the cells which are accessible by the $200\,\mathrm{nm}$ nanoparticles and potentially bacteria. We need to test each the immune system can effectively clean bacteria which reach the surface. To further suppress the formation of biofilms, we can attach anti-bacteria molecules on hyaluronan. The anti-bacteria molecules gradually release as the brush is digestion by the mammalian cells.

CHAPTER 7

OUTLOOK

The work presented in this thesis on the super-sized hyaluronan brush is only the beginning of valuable avenues of research in polymer physics, biomaterial, molecular biology and cellular biology. In this chapter, we present potential research projects, some of which call for exciting advances in experimental techniques.

7.1 Improving Sample Preparation

7.1.1 Improving Membrane Fragments Coverage

The SEM image in Figure 4.2 shows that the coverage of membrane fragments is $30\,\%$ and there is a big room for improvement. For polymer physics research, ideally, the surface should be uniformly covered by hyaluronan synthase which requires higher surface coverage of membrane fragments. For biomaterial application, higher surface coverage means thicker brush and longer lifetime before the brush thickness reduces to a certain threshold. The sample was air-dried before mounted on the SEM and the membrane fragments might shrink or get damaged during the drying process. Thus the coverage of membrane fragments should be measured in a hydrated state. The super-resolution structured illumination microscopy has a lateral resolution of $50\,\mathrm{nm}$ and is a convenient tool to image the membrane fragments. Electron cryomicroscopy has higher resolution but requires more work in sample preparation and also costs more.

A potential cause of the relative low fragment coverage is competence of other molecules. In the membrane fragments, proteins which are not embedded in the fragments and the tris molecules in the storage buffer can compete for crosslinking with the glutaraldehyde coated in the surface because they also have primary amine groups. Dialysis using a $100\,\mathrm{kDa}$

molecular mass cutoff membrane can remove these molecules.

Another potential cause of the low coverage is that a significant portion of the fragments are too big to be efficiently crosslinked due to geometric hindrance. Sonication with a probe sonicator should break up the fragments and thus increase the immobilization efficiency.

7.1.2 Improving Reinforcement Efficiency

After the reinforcement treatment (Figure 4.13), about $50\,\%$ of hyaluronan was lost. One can optimize the pH, ionic strength and concentrations of EDC and sulfo-NHS to achieve optimal reinforcement efficiency. Pipetting during solution exchange also leads to hyaluronan desorption and a better slide holder can provide milder washing condition (Section 7.6).An optimized reinforcement procedure will increase the stability of the brush and preserve the natural state of end-grafted hyaluronan.

7.1.3 Post-reinforcement Modification

After the reinforcement process, the brush can be further modified to attach fluorescence dye, growth factors or anti-bacteria molecules. Such modification will facilitate the dynamic change of brush upon external environment and improve the performance in biomaterial applications.

7.2 Length Distribution of Polymers in the Brush

Length distribution and surface density of the hyaluronan in the brush are vital to fully characterize the brush. As we are writing this thesis, we also building a collaboration with Dr. Adam Hall on measuring hyaluronan length distribution using the nanopore technique which only requires nanograms of hyaluronan [87]. Another promising technique to measure low quantity hyaluronan is the NanoSight®[110]. NanoSight has higher data collection rate but required fluorescence labeling to measure low molecular weight hyaluronan polymers while the nanopore is a label-free method. Both methods simultaneous measure

hyaluronan concentration from which we can estimate the hyaluronan density in the brush.

7.3 Comparing Brush Structure with Theory

Once the length distribution and surface density of the hyaluronan in the brush are known, we can compare the predictions and measurements on the monomer density profiles [42] and the penetration profiles of nanoparticles of different sizes [43]. When comparing the monomer density profile, one may need to add the interaction between the hyaluronan and GFPn to the theory for more accurate prediction.

7.4 Curvature Effect in Polymer Brush

Either for the interest in the statistical physics of polymers [111, 112, 113, 114] and the application of polymer brush, it is valuable to study polymer brushes on spherical surfaces [115, 116, 117, 118]. Spherical brushes obey a different scaling law [111, 112, 113] and a different predicted monomer density profile [114]. The diffraction based tracking microscopy and thermal denaturing of hyaluronan synthase can test the scaling law at the micrometer scale. Our thick brush provide a unique opportunity to measure the monomer density profile of spherical brushes (Figure 4.5).

7.5 Single Polymer Tracking

This is an exciting technique to develop which fully unleash the academic potential of the super-size polymer brush. For the first time, we will be able to directly observe motion of a single polymer in the brush which bring experimental study of polymer brushes to single molecule level and enable testing predictions on polymer brushes which were made more than two decades ago but remained experimentally untested such as the distribution of the end monomers [41, 42].

In the first phase of the project, one can start by end-grafting DNA polymers into the

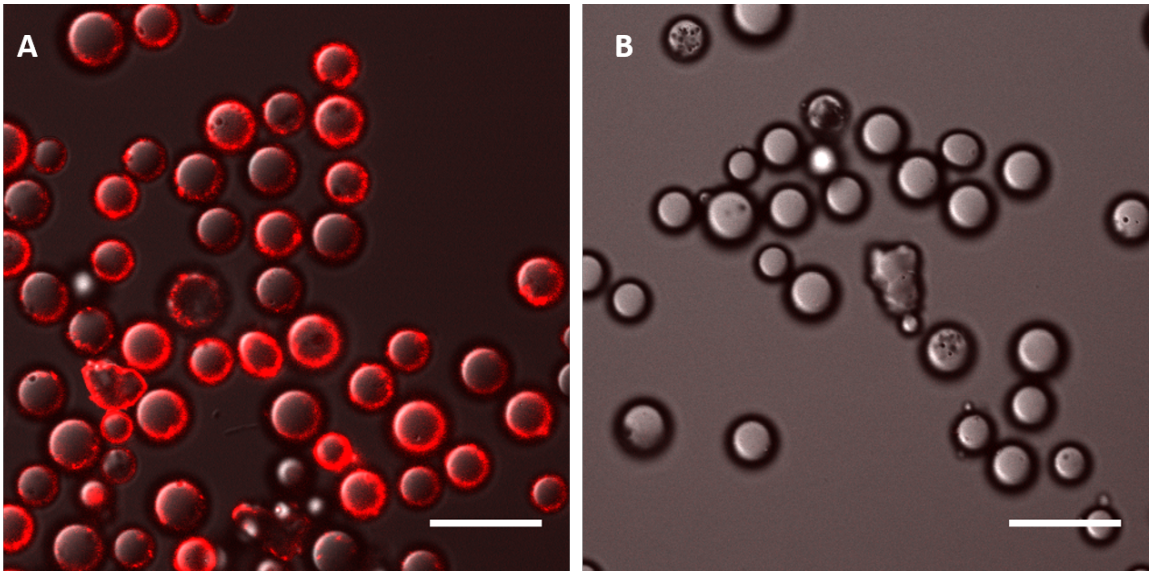

Figure 7.1: **A** Adding fluorescent streptavidin to lipid-biotin modified membrane fragments on glass beads. **B** Control experiment without lipid-biotin. Scale bars are 20 µm
.

hyaluronan brush. The 5' and 3' ends of DNA can be distinctly modified and the whole polymer can be brightly labeled using the YOYO®-1 dye [119].

Preparing the sample to visualize single hyaluronan polymer is more challenging but practical with the help from collaborating chemists. The sugar ring at the reducing end of a hyaluronan polymer is not stable and enable specific chemical modification at this end using click chemistry [120]. For example, one can prepare hyaluronan-biotin. We have successfully decorated the membrane fragments which hyaluronan synthases were embedded with lipid-biotin (Figure 7.1). One can end-graft the exogenous hyaluronan by linking the two biotin molecules with a streptavidin protein. Another method is to use HA-lipid.

7.6 Improving Sample Holders

With the Teflon coverslip hoder used in this thesis work, we need to take a z-stack to measure the thickness of the brush. The Z resolution is two times worse than the XY resolution on a confocal microscope. The z-stack is sensitive to drift between the sample

holder and the nosepiece. This method is also sensitive to photobleaching. For example, when the illumination is focused on the top of the brush, fluorophores in other parts of the brush are also absorbing light and also photobleaching.

All the issues above can be solved if we can image a brush whose grafting surface is parallel to the axial direction of the microscope. Then we can collect data of the vertical intensity profile in a single XY image.

It is also important to build the sample holder as a flow chamber which allows for a few exciting experiments on shear flow and polymer brush described in the following section. In addition, it has been shown that flow exchange via pipetting leads to significant hyaluronan desorption and the new sample holder helps to preserve the hyaluronan polymers in the brush. We suspect the inconsistence in experiments on hyaluronan desorption in Section 5.9.3 is from inconsistent chemical removal and the damage of brush caused by shear flow from pipetting.

7.7 Polymer Response to Shear Flow

Polymer brush responses to shear flow are less understood than that of the dynamics of polymer brush in a static solvent. For example, we find conflicting predictions regarding the change in brush height due to shear flow [121, 122, 123, 124, 125, 126]. With a flow chamber (Section 7.6), one can easily measure the thickness of brush under different shear flow conditions.

Another interesting experiment is to measure the desorption of polymers in the brush. It is predicted that the desorption of longer polymers is faster because of chain stretching and reduction of blob size [127]. This experiment becomes accessible once the single polymer imaging protocol (Section 7.5) is established.

7.8 Molecule Transportation across Brush Interface

The pericellular matrix is the chemical interface between cells and the extracellular space. It is important to study the transportation of molecules through polymer brushes.

7.9 Summary

This Outlook demostrates that our super-sized hyaluronan polymer brush serves as a platform which opens up a wide spectrum of future research. We also expect more research projects to be found as deeper understand of this system is achieved. We hope this Outlook can serve as a map for future graduate students who should pay attention to the advantages of fluorescence microscopy which open research opportunities inaccessible with the traditional methods for polymer brush characterization.

REFERENCES

[1] B. P. Toole, "Hyaluronan," in *Proteoglycans*, CRC Press, 2000, pp. 70–101.

[2] N. R. Council *et al.*, *Transforming glycoscience: a roadmap for the future*. National Academies Press, 2012.

[3] T. C. Laurent, U. B. Laurent, and J. R. E. Fraser, "The structure and function of hyaluronan: An overview," *Immunology and cell biology*, vol. 74, no. 2, A1, 1996.

[4] L. Bohaumilitzky, A.-K. Huber, E. M. Stork, S. Wengert, F. Woelfl, and H. Boehm, "A trickster in disguise: Hyaluronan's ambivalent roles in the matrix," *Frontiers in Oncology*, vol. 7, p. 242, 2017.

[5] R. Stern, "Hyaluronan catabolism: A new metabolic pathway," *European journal of cell biology*, vol. 83, no. 7, pp. 317–325, 2004.

[6] P Ghosh, "The role of hyaluronic acid (hyaluronan) in health and disease: Interactions with cells, cartilage and components of synovial fluid.," *Clinical and experimental rheumatology*, vol. 12, no. 1, pp. 75–82, 1994.

[7] L. Raio, F. Ghezzi, A. Cromi, E. Cereda, and A. Passi, "Sonographic morphology and hyaluronan content of umbilical cords of healthy and down syndrome fetuses in early gestation," *Early human development*, vol. 77, no. 1-2, pp. 1–12, 2004.

[8] D. C. Briggs, H. L. Birchenough, T. Ali, M. S. Rugg, J. P. Waltho, E. Ievoli, T. A. Jowitt, J. J. Enghild, R. P. Richter, A. Salustri, *et al.*, "Metal ion-dependent heavy chain transfer activity of tsg-6 mediates assembly of the cumulus-oocyte matrix," *Journal of Biological Chemistry*, vol. 290, no. 48, pp. 28 708–28 723, 2015.

[9] J. E. Curtis, "The mechanics of ovulation depend on an incredibly soft and sugar-rich extracellular matrix," *Biophysical journal*, vol. 110, no. 12, pp. 2566–2567, 2016.

[10] M. Choudhary, X. Zhang, P. Stojković, L. Hyslop, G. Anyfantis, M. Herbert, A. P. Murdoch, M. Stojković, and M. Lako, "Putative role of hyaluronan and its related genes, has2 and rhamm, in human early preimplantation embryogenesis and embryonic stem cell characterization," *Stem Cells*, vol. 25, no. 12, pp. 3045–3057, 2007.

[11] O. Oksala, T. Salo, R. Tammi, L. Häkkinen, M. Jalkanen, P. Inki, and H. Larjava, "Expression of proteoglycans and hyaluronan during wound healing.," *Journal of Histochemistry & Cytochemistry*, vol. 43, no. 2, pp. 125–135, 1995.

[12] M. Pyka, C. Wetzel, A. Aguado, M. Geissler, H. Hatt, and A. Faissner, "Chondroitin sulfate proteoglycans regulate astrocyte-dependent synaptogenesis and modulate synaptic activity in primary embryonic hippocampal neurons," *European Journal of Neuroscience*, vol. 33, no. 12, pp. 2187–2202, 2011.

[13] P Vabres, "Hyaluronan, embryogenesis and morphogenesis," in *Annales de Dermatologie et de Venereologie*, vol. 137, 2010, S9–S14.

[14] P. H. Weigel and P. L. DeAngelis, "Hyaluronan synthases: A decade-plus of novel glycosyltransferases," *Journal of Biological Chemistry*, vol. 282, no. 51, pp. 36 777–36 781, 2007.

[15] P. H. Weigel and B. A. Baggenstoss, "Hyaluronan synthase polymerizing activity and control of product size are discrete enzyme functions that can be uncoupled by mutagenesis of conserved cysteines," *Glycobiology*, vol. 22, no. 10, pp. 1302–1310, 2012.

[16] C. Spagnoli, A. Korniakov, A. Ulman, E. A. Balazs, Y. L. Lyubchenko, and M. K. Cowman, "Hyaluronan conformations on surfaces: Effect of surface charge and hydrophobicity," *Carbohydrate research*, vol. 340, no. 5, pp. 929–941, 2005.

[17] W. S. Toh, E. H. Lee, X.-M. Guo, J. K. Chan, C. H. Yeow, A. B. Choo, and T. Cao, "Cartilage repair using hyaluronan hydrogel-encapsulated human embryonic stem cell-derived chondrogenic cells," *Biomaterials*, vol. 31, no. 27, pp. 6968–6980, 2010.

[18] X. Z. Shu, K. Ghosh, Y. Liu, F. S. Palumbo, Y. Luo, R. A. Clark, and G. D. Prestwich, "Attachment and spreading of fibroblasts on an rgd peptide–modified injectable hyaluronan hydrogel," *Journal of biomedical materials research Part A*, vol. 68, no. 2, pp. 365–375, 2004.

[19] P. H. Weigel, "Functional characteristics and catalytic mechanisms of the bacterial hyaluronan synthases," *IUBMB life*, vol. 54, no. 4, pp. 201–211, 2002.

[20] N. Itano, T. Sawai, M. Yoshida, P. Lenas, Y. Yamada, M. Imagawa, T. Shinomura, M. Hamaguchi, Y. Yoshida, Y. Ohnuki, *et al.*, "Three isoforms of mammalian hyaluronan synthases have distinct enzymatic properties," *Journal of Biological Chemistry*, vol. 274, no. 35, pp. 25 085–25 092, 1999.

[21] N. Itano and K. Kimata, "Mammalian hyaluronan synthases," *IUBMB life*, vol. 54, no. 4, pp. 195–199, 2002.

[22] R. Mendichi, L. Šoltés, and A. Giacometti Schieroni, "Evaluation of radius of gyration and intrinsic viscosity molar mass dependence and stiffness of hyaluronan," *Biomacromolecules*, vol. 4, no. 6, pp. 1805–1810, 2003.

[23] E. A. Balazs, "The physical properties of synovial fluid and the special role of hyaluronic acid," *Disorders of the Knee*, vol. 2, pp. 61–74, 1974.

[24] J. S. Richards, "Ovulation: New factors that prepare the oocyte for fertilization," *Molecular and cellular endocrinology*, vol. 234, no. 1-2, pp. 75–79, 2005.

[25] N. Itano, T. Chanmee, and K. Kimata, "Hyaluronan synthase 1-3 (has1-3)," in *Handbook of Glycosyltransferases and Related Genes*, N. Taniguchi, K. Honke, M. Fukuda, H. Narimatsu, Y. Yamaguchi, and T. Angata, Eds. Tokyo: Springer Japan, 2014, pp. 865–872, ISBN: 978-4-431-54240-7.

[26] R. H. Tammi, A. G. Passi, K. Rilla, E. Karousou, D. Vigetti, K. Makkonen, and M. I. Tammi, "Transcriptional and post-translational regulation of hyaluronan synthesis," *The FEBS journal*, vol. 278, no. 9, pp. 1419–1428, 2011.

[27] P. H. Weigel, "Hyaluronan synthase: The mechanism of initiation at the reducing end and a pendulum model for polysaccharide translocation to the cell exterior," *International journal of cell biology*, vol. 2015, 2015.

[28] K. Kumari and P. H. Weigel, "Identification of a membrane-localized cysteine cluster near the substrate-binding sites of the streptococcus equisimilis hyaluronan synthase," *Glycobiology*, vol. 15, no. 5, pp. 529–539, 2004.

[29] V. L. Tlapak-Simmons, E. S. Kempner, B. A. Baggenstoss, and P. H. Weigel, "The active streptococcal hyaluronan synthases (hass) contain a single has monomer and multiple cardiolipin molecules," *Journal of Biological Chemistry*, vol. 273, no. 40, pp. 26 100–26 109, 1998.

[30] C. Heldermon, P. L. DeAngelis, and P. H. Weigel, "Topological organization of the hyaluronan synthase fromstreptococcus pyogenes," *Journal of Biological Chemistry*, vol. 276, no. 3, pp. 2037–2046, 2001.

[31] C. Breton, E. Bettler, D. H. Joziasse, R. A. Geremia, and A. Imberty, "Sequence-function relationships of prokaryotic and eukaryotic galactosyltransferases," *The Journal of Biochemistry*, vol. 123, no. 6, pp. 1000–1009, 1998.

[32] V. L. Tlapak-Simmons, B. A. Baggenstoss, T. Clyne, and P. H. Weigel, "Purification and lipid dependence of the recombinant hyaluronan synthases from streptococcus pyogenes andstreptococcus equisimilis," *Journal of Biological Chemistry*, vol. 274, no. 7, pp. 4239–4245, 1999.

[33] A. P. Medina, J. Lin, and P. H. Weigel, "Hyaluronan synthase mediates dye translocation across liposomal membranes," *BMC biochemistry*, vol. 13, no. 1, p. 2, 2012.

[34] A. Mashaghi, P. Partovi-Azar, T. Jadidi, N. Nafari, P. Maass, M. R. R. Tabar, M. Bonn, and H. J. Bakker, "Hydration strongly affects the molecular and electronic structure of membrane phospholipids," *The Journal of chemical physics*, vol. 136, no. 11, 03B611, 2012.

[35] K. Kumari and P. H. Weigel, "Molecular cloning, expression, and characterization of the authentic hyaluronan synthase from group c streptococcus equisimilis," *Journal of Biological Chemistry*, vol. 272, no. 51, pp. 32 539–32 546, 1997.

[36] P. L. DeAngelis and P. H. Weigel, "Immunochemical confirmation of the primary structure of streptococcal hyaluronan synthase and synthesis of high molecular weight product by the recombinant enzyme," *Biochemistry*, vol. 33, no. 31, pp. 9033–9039, 1994.

[37] B. A. Baggenstoss and P. H. Weigel, "Size exclusion chromatography–multiangle laser light scattering analysis of hyaluronan size distributions made by membrane-bound hyaluronan synthase," *Analytical biochemistry*, vol. 352, no. 2, pp. 243–251, 2006.

[38] E. Evans, "Looking inside molecular bonds at biological interfaces with dynamic force spectroscopy," *Biophysical chemistry*, vol. 82, no. 2-3, pp. 83–97, 1999.

[39] B. T. Marshall, M. Long, J. W. Piper, T. Yago, R. P. McEver, and C. Zhu, "Direct observation of catch bonds involving cell-adhesion molecules," *Nature*, vol. 423, no. 6936, p. 190, 2003.

[40] W. J. Brittain and S. Minko, "A structural definition of polymer brushes," *Journal of Polymer Science Part A: Polymer Chemistry*, vol. 45, no. 16, pp. 3505–3512, 2007.

[41] S. T. Milner, T. Witten, and M. Cates, "Theory of the grafted polymer brush," *Macromolecules*, vol. 21, no. 8, pp. 2610–2619, 1988.

[42] W. M. de Vos and F. A. Leermakers, "Modeling the structure of a polydisperse polymer brush," *Polymer*, vol. 50, no. 1, pp. 305–316, 2009.

[43] W. M. de Vos, F. A. Leermakers, A. de Keizer, J. M. Kleijn, and M. A. Cohen Stuart, "Interaction of particles with a polydisperse brush: A self-consistent-field analysis," *Macromolecules*, vol. 42, no. 15, pp. 5881–5891, 2009.

[44] B. A. Baggenstoss, E. N. Harris, J. L. Washburn, A. P. Medina, L. Nguyen, and P. H. Weigel, "Hyaluronan synthase control of synthesis rate and hyaluronan product

size are independent functions differentially affected by mutations in a conserved tandem b-x7-b motif," *Glycobiology*, vol. 27, no. 2, pp. 154–164, 2017.

[45] A Dorfman, A Markovitz, and J. Cifonelli, "Metabolism of hyaluronic acid and chondroitinsulfuric acids.," in *Federation proceedings*, vol. 17, 1958, pp. 1093–1099.

[46] V. L. Tlapak-Simmons, B. A. Baggenstoss, K. Kumari, C. Heldermon, and P. H. Weigel, "Kinetic characterization of the recombinant hyaluronan synthases from streptococcus pyogenes and streptococcus equisimilis," *Journal of Biological Chemistry*, vol. 274, no. 7, pp. 4246–4253, 1999.

[47] V. L. Tlapak-Simmons, C. A. Baron, and P. H. Weigel, "Characterization of the purified hyaluronan synthase from streptococcus equisimilis," *Biochemistry*, vol. 43, no. 28, pp. 9234–9242, 2004.

[48] P. H. Weigel, B. A. Baggenstoss, and J. L. Washburn, "Hyaluronan synthase assembles hyaluronan on a [glcnac] n- udp primer and hyaluronan retains this residual chitin oligomer as a cap at the nonreducing end," *Glycobiology*, vol. 27, no. 6, pp. 536–554, 2017.

[49] P. H. Weigel, A. J. Padgett-McCue, and B. A. Baggenstoss, "Methods for measuring class i membrane-bound hyaluronan synthase activity," in *Glycosyltransferases*, Springer, 2013, pp. 229–247.

[50] P. Quinn, G. Griffiths, and G. Warren, "Density of newly synthesized plasma membrane proteins in intracellular membranes ii. biochemical studies.," *The Journal of cell biology*, vol. 98, no. 6, pp. 2142–2147, 1984.

[51] A. Razatos, Y.-L. Ong, M. M. Sharma, and G. Georgiou, "Molecular determinants of bacterial adhesion monitored by atomic force microscopy," *Proceedings of the National Academy of Sciences*, vol. 95, no. 19, pp. 11 059–11 064, 1998.

[52] D. Dulin, T. J. Cui, J. Cnossen, M. W. Docter, J. Lipfert, and N. H. Dekker, "High spatiotemporal-resolution magnetic tweezers: Calibration and applications for dna dynamics," *Biophysical journal*, vol. 109, no. 10, pp. 2113–2125, 2015.

[53] B. Clarris and J. Fraser, "On the pericellular zone of some mammalian cells in vitro," *Experimental cell research*, vol. 49, no. 1, pp. 181–193, 1968.

[54] L. T. McLane, P. Chang, A. Granqvist, H. Boehm, A. Kramer, J. Scrimgeour, and J. E. Curtis, "Spatial organization and mechanical properties of the pericellular matrix on chondrocytes," *Biophysical journal*, vol. 104, no. 5, pp. 986–996, 2013.

[55] P. S. Chang, L. T. McLane, R. Fogg, J. Scrimgeour, J. S. Temenoff, A. Granqvist, and J. E. Curtis, "Cell surface access is modulated by tethered bottlebrush proteoglycans," *Biophysical journal*, vol. 110, no. 12, pp. 2739–2750, 2016.

[56] B. Button, L.-H. Cai, C. Ehre, M. Kesimer, D. B. Hill, J. K. Sheehan, R. C. Boucher, and M. Rubinstein, "A periciliary brush promotes the lung health by separating the mucus layer from airway epithelia," *Science*, vol. 337, no. 6097, pp. 937–941, 2012. eprint: `http://science.sciencemag.org/content/337/6097/937.full.pdf`.

[57] R. C. Gonzalez and R. E. Woods, *Digital image processing*, 2012.

[58] N. Otsu, "A threshold selection method from gray-level histograms," *IEEE transactions on systems, man, and cybernetics*, vol. 9, no. 1, pp. 62–66, 1979.

[59] H. Zhang, S. L. Baader, M. Sixt, J. Kappler, and U. Rauch, "Neurocan–gfp fusion protein: A new approach to detect hyaluronan on tissue sections and living cells," *Journal of Histochemistry & Cytochemistry*, vol. 52, no. 7, pp. 915–922, 2004.

[60] D. Kohda, C. J. Morton, A. A. Parkar, H. Hatanaka, F. M. Inagaki, I. D. Campbell, and A. J. Day, "Solution structure of the link module: A hyaluronan-binding domain involved in extracellular matrix stability and cell migration," *Cell*, vol. 86, no. 5, pp. 767–775, 1996.

[61] C. Kiani, C. Liwen, Y. J. Wu, J. Y. Albert, and B. Y. Burton, "Structure and function of aggrecan," *Cell research*, vol. 12, no. 1, p. 19, 2002.

[62] Y. Yamaguchi, "Lecticans: Organizers of the brain extracellular matrix," *Cellular and Molecular Life Sciences CMLS*, vol. 57, no. 2, pp. 276–289, 2000.

[63] A. Rosenfeld, "Computer vision: A source of models for biological visual processes?" *IEEE Transactions on Biomedical Engineering*, vol. 36, no. 1, pp. 93–96, 1989.

[64] I. Vilfan, J Lipfert, D. Koster, S. Lemay, and N. Dekker, "Magnetic tweezers for single-molecule experiments," in *Handbook of single-molecule biophysics*, Springer, 2009, pp. 371–395.

[65] R. Parthasarathy, "Rapid, accurate particle tracking by calculation of radial symmetry centers," *Nature methods*, vol. 9, no. 7, p. 724, 2012.

[66] D. T. Kovari, Y. Yan, L. Finzi, and D. Dunlap, "Tethered particle motion: An easy technique for probing dna topology and interactions with transcription factors," in *Single Molecule Analysis*, Springer, 2018, pp. 317–340.

[67] S. Edmondson, V. L. Osborne, and W. T. Huck, "Polymer brushes via surface-initiated polymerizations," *Chemical society reviews*, vol. 33, no. 1, pp. 14–22, 2004.

[68] W. Kim and J. Jung, "Polymer brush: A promising grafting approach to scaffolds for tissue engineering," *BMB reports*, vol. 49, no. 12, p. 655, 2016.

[69] S. Attili, O. V. Borisov, and R. P. Richter, "Films of end-grafted hyaluronan are a prototype of a brush of a strongly charged, semiflexible polyelectrolyte with intrinsic excluded volume," *Biomacromolecules*, vol. 13, no. 5, pp. 1466–1477, 2012.

[70] T. W. Kelley, P. A. Schorr, K. D. Johnson, M. Tirrell, and C. D. Frisbie, "Direct force measurements at polymer brush surfaces by atomic force microscopy," *Macromolecules*, vol. 31, no. 13, pp. 4297–4300, 1998.

[71] S. Yamamoto, M. Ejaz, Y. Tsujii, M. Matsumoto, and T. Fukuda, "Surface interaction forces of well-defined, high-density polymer brushes studied by atomic force microscopy. 1. effect of chain length," *macromolecules*, vol. 33, no. 15, pp. 5602–5607, 2000.

[72] S. Yamamoto, M. Ejaz, Y. Tsujii, and T. Fukuda, "Surface interaction forces of well-defined, high-density polymer brushes studied by atomic force microscopy. 2. effect of graft density," *Macromolecules*, vol. 33, no. 15, pp. 5608–5612, 2000.

[73] J. Piehler, A. Brecht, R. Valiokas, B. Liedberg, and G. Gauglitz, "A high-density poly (ethylene glycol) polymer brush for immobilization on glass-type surfaces," *Biosensors and Bioelectronics*, vol. 15, no. 9-10, pp. 473–481, 2000.

[74] A Karim, S. Satija, J. Douglas, J. Ankner, and L. Fetters, "Neutron reflectivity study of the density profile of a model end-grafted polymer brush: Influence of solvent quality," *Physical review letters*, vol. 73, no. 25, p. 3407, 1994.

[75] R Ivkov, P. Butler, S. Satija, and L. Fetters, "Effect of solvent flow on a polymer brush: A neutron reflectivity study of the brush height and chain density profile," *Langmuir*, vol. 17, no. 10, pp. 2999–3005, 2001.

[76] S. M. Sirard, R. R. Gupta, T. P. Russell, J. J. Watkins, P. F. Green, and K. P. Johnston, "Structure of end-grafted polymer brushes in liquid and supercritical carbon dioxide: A neutron reflectivity study," *Macromolecules*, vol. 36, no. 9, pp. 3365–3373, 2003.

[77] X. Gao, N. Kucerka, M.-P. Nieh, J. Katsaras, S. Zhu, J. L. Brash, and H. Sheardown, "Chain conformation of a new class of peg-based thermoresponsive polymer brushes grafted on silicon as determined by neutron reflectometry," *Langmuir*, vol. 25, no. 17, pp. 10 271–10 278, 2009.

[78] J. Klein, E. Kumacheva, D. Mahalu, D. Perahia, and L. J. Fetters, "Reduction of frictional forces between solid surfaces bearing polymer brushes," *Nature*, vol. 370, no. 6491, p. 634, 1994.

[79] A. Harder, V. Walhorn, T. Dierks, X. Fernandez-Busquets, and D. Anselmetti, "Single-molecule force spectroscopy of cartilage aggrecan self-adhesion," *Biophysical journal*, vol. 99, no. 10, pp. 3498–3504, 2010.

[80] L. Ng, A. J. Grodzinsky, P. Patwari, J. Sandy, A. Plaas, and C. Ortiz, "Individual cartilage aggrecan macromolecules and their constituent glycosaminoglycans visualized via atomic force microscopy," *Journal of structural biology*, vol. 143, no. 3, pp. 242–257, 2003.

[81] J. Yu, N. E. Jackson, X. Xu, B. K. Brettmann, M. Ruths, J. J. de Pablo, and M. Tirrell, "Multivalent ions induce lateral structural inhomogeneities in polyelectrolyte brushes," *Science advances*, vol. 3, no. 12, eaao1497, 2017.

[82] N. E. Jackson, B. K. Brettmann, V. Vishwanath, M. Tirrell, and J. J. de Pablo, "Comparing solvophobic and multivalent induced collapse in polyelectrolyte brushes," *ACS Macro Letters*, vol. 6, no. 2, pp. 155–160, 2017.

[83] B. Brettmann, P. Pincus, and M. Tirrell, "Lateral structure formation in polyelectrolyte brushes induced by multivalent ions," *Macromolecules*, vol. 50, no. 3, pp. 1225–1235, 2017.

[84] J. Schindelin, I. Arganda-Carreras, E. Frise, V. Kaynig, M. Longair, T. Pietzsch, S. Preibisch, C. Rueden, S. Saalfeld, B. Schmid, *et al.*, "Fiji: An open-source platform for biological-image analysis," *Nature methods*, vol. 9, no. 7, p. 676, 2012.

[85] J. Mondek, M. Kalina, V. Simulescu, and M. Pekař, "Thermal degradation of high molar mass hyaluronan in solution and in powder; comparison with bsa," *Polymer Degradation and Stability*, vol. 120, pp. 107–113, 2015.

[86] A. Kornberg, T. A. Baker, *et al.*, *DNA replication*. Wh Freeman San Francisco, 1980.

[87] F. Rivas, O. K. Zahid, H. L. Reesink, B. T. Peal, A. J. Nixon, P. L. DeAngelis, A. Skardal, E. Rahbar, and A. R. Hall, "Label-free analysis of physiological hyaluronan size distribution with a solid-state nanopore sensor," *Nature communications*, vol. 9, no. 1, p. 1037, 2018.

[88] L. J. Bain, D. L. Weeks, *et al.*, "A note on the truncated exponential distribution," *The Annals of Mathematical Statistics*, vol. 35, no. 3, pp. 1366–1367, 1964.

[89] W. L. Deemer Jr and D. F. Votaw Jr, "Estimation of parameters of truncated or censored exponential distributions," *The Annals of Mathematical Statistics*, pp. 498–504, 1955.

[90] H. Saitoh, K. Takagaki, M. Majima, T. Nakamura, A. Matsuki, M. Kasai, H. Narita, and M. Endo, "Enzymic reconstruction of glycosaminoglycan oligosaccharide chains using the transglycosylation reaction of bovine testicular hyaluronidase," *Journal of Biological Chemistry*, vol. 270, no. 8, pp. 3741–3747, 1995.

[91] J. Yang, F. Cheng, H. Yu, J. Wang, Z. Guo, and G. Stephanopoulos, "Key role of the carboxyl terminus of hyaluronan synthase in processive synthesis and size control of hyaluronic acid polymers," *Biomacromolecules*, vol. 18, no. 4, pp. 1064–1073, 2017.

[92] J. W. Costerton, P. S. Stewart, and E. P. Greenberg, "Bacterial biofilms: A common cause of persistent infections," *Science*, vol. 284, no. 5418, pp. 1318–1322, 1999.

[93] R. A. Weinstein and R. O. Darouiche, "Device-associated infections: A macroproblem that starts with microadherence," *Clinical Infectious Diseases*, vol. 33, no. 9, pp. 1567–1572, 2001.

[94] R. O. Darouiche, "Treatment of infections associated with surgical implants," *New England Journal of Medicine*, vol. 350, no. 14, pp. 1422–1429, 2004.

[95] E. deLancey Pulcini and G. James, "Biofilms and device implants," *Applied Biomedical Microbiology: A Biofilms Approach*, p. 59, 2009.

[96] J. Costerton, L Montanaro, and C. Arciola, "Biofilm in implant infections: Its production and regulation," *The International journal of artificial organs*, vol. 28, no. 11, pp. 1062–1068, 2005.

[97] C. Vuong, J. M. Voyich, E. R. Fischer, K. R. Braughton, A. R. Whitney, F. R. DeLeo, and M. Otto, "Polysaccharide intercellular adhesin (pia) protects staphylococcus epidermidis against major components of the human innate immune system," *Cellular microbiology*, vol. 6, no. 3, pp. 269–275, 2004.

[98] P. Ø. Jensen, M. Givskov, T. Bjarnsholt, and C. Moser, "The immune system vs. pseudomonas aeruginosa biofilms," *Pathogens and Disease*, vol. 59, no. 3, pp. 292–305, 2010.

[99] S. Goodman, K. Obergfell, J. Jurcisek, L. Novotny, J. Downey, E. Ayala, N Tjokro, B Li, S. Justice, and L. Bakaletz, "Biofilms can be dispersed by focusing the immune system on a common family of bacterial nucleoid-associated proteins," *Mucosal immunology*, vol. 4, no. 6, p. 625, 2011.

[100] T.-F. C. Mah and G. A. O'toole, "Mechanisms of biofilm resistance to antimicrobial agents," *Trends in microbiology*, vol. 9, no. 1, pp. 34–39, 2001.

[101] M. R. Nejadnik, H. C. van der Mei, W. Norde, and H. J. Busscher, "Bacterial adhesion and growth on a polymer brush-coating," *Biomaterials*, vol. 29, no. 30, pp. 4117–4121, 2008.

[102] G. Gao, D. Lange, K. Hilpert, J. Kindrachuk, Y. Zou, J. T. Cheng, M. Kazemzadeh-Narbat, K. Yu, R. Wang, S. K. Straus, *et al.*, "The biocompatibility and biofilm resistance of implant coatings based on hydrophilic polymer brushes conjugated with antimicrobial peptides," *Biomaterials*, vol. 32, no. 16, pp. 3899–3909, 2011.

[103] A. K. Muszanska, E. T. Rochford, A. Gruszka, A. A. Bastian, H. J. Busscher, W. Norde, H. C. van der Mei, and A. Herrmann, "Antiadhesive polymer brush coating functionalized with antimicrobial and rgd peptides to reduce biofilm formation and enhance tissue integration," *Biomacromolecules*, vol. 15, no. 6, pp. 2019–2026, 2014.

[104] M. Morra, "Engineering of biomaterials surfaces by hyaluronan," *Biomacromolecules*, vol. 6, no. 3, pp. 1205–1223, 2005.

[105] P Brouqui, M. Rousseau, A Stein, M Drancourt, and D Raoult, "Treatment of pseudomonas aeruginosa-infected orthopedic prostheses with ceftazidime-ciprofloxacin antibiotic combination.," *Antimicrobial agents and chemotherapy*, vol. 39, no. 11, pp. 2423–2425, 1995.

[106] L. Y. Bourguignon, P. A. Singleton, F. Diedrich, R. Stern, and E. Gilad, "Cd44 interaction with na+-h+ exchanger (nhe1) creates acidic microenvironments leading to hyaluronidase-2 and cathepsin b activation and breast tumor cell invasion," *Journal of Biological Chemistry*, vol. 279, no. 26, pp. 26 991–27 007, 2004.

[107] E. Bastow, S Byers, S. Golub, C. Clarkin, A. Pitsillides, and A. Fosang, "Hyaluronan synthesis and degradation in cartilage and bone," *Cellular and Molecular Life Sciences*, vol. 65, no. 3, pp. 395–413, 2008.

[108] J. G. Cannon, R. G. Tompkins, J. A. Gelfand, H. R. Michie, G. G. Stanford, J. W. Van Der Meer, S. Endres, G. Lonnemann, J. Corsetti, B. Chernow, *et al.*, "Circulating interleukin-1 and tumor necrosis factor in septic shock and experimental endotoxin fever," *Journal of Infectious Diseases*, vol. 161, no. 1, pp. 79–84, 1990.

[109] U. Mamat, K. Wilke, D. Bramhill, A. B. Schromm, B. Lindner, T. A. Kohl, J. L. Corchero, A. Villaverde, L. Schaffer, S. R. Head, *et al.*, "Detoxifying escherichia coli for endotoxin-free production of recombinant proteins," *Microbial cell factories*, vol. 14, no. 1, p. 57, 2015.

[110] V. Filipe, A. Hawe, and W. Jiskoot, "Critical evaluation of nanoparticle tracking analysis (nta) by nanosight for the measurement of nanoparticles and protein aggregates," *Pharmaceutical research*, vol. 27, no. 5, pp. 796–810, 2010.

[111] S. Milner, "Polymer brushes," *Science*, vol. 251, no. 4996, pp. 905–914, 1991.

[112] C. Wijmans and E. B. Zhulina, "Polymer brushes at curved surfaces," *Macromolecules*, vol. 26, no. 26, pp. 7214–7224, 1993.

[113] D. Dukes, Y. Li, S. Lewis, B. Benicewicz, L. Schadler, and S. K. Kumar, "Conformational transitions of spherical polymer brushes: Synthesis, characterization, and theory," *Macromolecules*, vol. 43, no. 3, pp. 1564–1570, 2010.

[114] F. Lo Verso, S. A. Egorov, A. Milchev, and K. Binder, "Spherical polymer brushes under good solvent conditions: Molecular dynamics results compared to density functional theory," *The Journal of chemical physics*, vol. 133, no. 18, p. 184 901, 2010.

[115] G. Storm, S. O. Belliot, T. Daemen, and D. D. Lasic, "Surface modification of nanoparticles to oppose uptake by the mononuclear phagocyte system," *Advanced drug delivery reviews*, vol. 17, no. 1, pp. 31–48, 1995.

[116] R. A. Vaia and J. F. Maguire, "Polymer nanocomposites with prescribed morphology: Going beyond nanoparticle-filled polymers," *Chemistry of Materials*, vol. 19, no. 11, pp. 2736–2751, 2007.

[117] L. M. Hall, A. Jayaraman, and K. S. Schweizer, "Molecular theories of polymer nanocomposites," *Current Opinion in Solid State and Materials Science*, vol. 14, no. 2, pp. 38–48, 2010.

[118] D. Trombly and V. Ganesan, "Interactions between polymer-grafted particles and bare particles for biocompatibility applications," *Journal of Polymer Science Part B: Polymer Physics*, vol. 47, no. 24, pp. 2566–2577, 2009.

[119] D. E. Smith, H. P. Babcock, and S. Chu, "Single-polymer dynamics in steady shear flow," *Science*, vol. 283, no. 5408, pp. 1724–1727, 1999.

[120] R. Novoa-Carballal and A. H. Müller, "Synthesis of polysaccharide-b-peg block copolymers by oxime click," *Chemical Communications*, vol. 48, no. 31, pp. 3781–3783, 2012.

[121] P. De Gennes, "Polymers at an interface; a simplified view," *Advances in colloid and interface science*, vol. 27, no. 3-4, pp. 189–209, 1987.

[122] Y Rabin and S Alexander, "Stretching of grafted polymer layers," *EPL (Europhysics Letters)*, vol. 13, no. 1, p. 49, 1990.

[123] J. L. Barrat, "A possible mechanism for swelling of polymer brushes under shear," *Macromolecules*, vol. 25, no. 2, pp. 832–834, 1992.

[124] M. G. Saphiannikova, V. A. Pryamitsyn, and T. Cosgrove, "Self-consistent brownian dynamics simulation of polymer brushes under shear," *Macromolecules*, vol. 31, no. 19, pp. 6662–6668, 1998.

[125] G.-L. He, H. Merlitz, J.-U. Sommer, and C.-X. Wu, "Static and dynamic properties of polymer brushes at moderate and high grafting densities: A molecular dynamics study," *Macromolecules*, vol. 40, no. 18, pp. 6721–6730, 2007.

[126] D. Anastassopoulos, N Spiliopoulos, A. Vradis, C Toprakcioglu, S. Baker, and A Menelle, "Shear-induced desorption in polymer brushes," *Macromolecules*, vol. 39, no. 26, pp. 8901–8904, 2006.

[127] M Aubouy, J. Harden, and M. Cates, "Shear-induced deformation and desorption of grafted polymer layers," *Journal de Physique II*, vol. 6, no. 7, pp. 969–984, 1996.

VITA

Wenbin Wei was born and grew up in Shenyang, Liaoning, China. He graduated from the Math and Science Senior High Division of Northeast Yucai School in 2008. He received his bachelor of Science in physics with a focus on particle physics from the University of Science and Technology of China in June 2012. Then he moved to Georgia Tech where he began working on his Ph.D. in biophysics under the supervision of Dr. Jennifer Curtis. He won the *2018 Amelio Award for Research Excellence by a Graduate Student*. His dissertation was defended in May 2018.